MECHANISMS OF HEAT TRANSPORT

THROUGH THE FLOOR OF THE EQUATORIAL PACIFIC OCEAN

by

John Crowe

B.S., Columbia University
(1974)

SUBMITTED IN PARTIAL FULFILLMENT
OF THE REQUIREMENTS FOR THE
DEGREE OF

DOCTOR OF PHILOSOPHY

at the

MASSACHUSETTS INSTITUTE OF TECHNOLOGY
and the
WOODS HOLE OCEANOGRAPHIC INSTITUTION

February, 1981

Signature of Author _____

Joint Program in Oceanography, Massachusetts Institute of Technology /
Woods Hole Oceanographic Institution, and the Department of Earth and
Planetary Sciences, Massachusetts Institute of Technology, November,
1980.

Certified by _____

Richard P. Von Herzen, Thesis Co-supervisor

Certified by _____

John G. Sclater, Thesis Co-supervisor

Accepted by _____

Richard P. Von Herzen, Chairman, Joint Oceanography Committee in the
Earth Sciences, Massachusetts Institute of Technology / Woods Hole
Oceanographic Institution

TABLE OF CONTENTS

LIST OF FIGURES

CHAPTER III

CHAPTER IV

LIST OF TABLES

BIOGRAPHICAL SKETCH

The author was born on May 31, 1952 in Brooklyn, New York. He graduated from Brooklyn Technical High School in June 1970. In September, 1970, he entered the School of Engineering at Columbia University where he recieved a B.S. degree in applied geophysics in May, 1974. In June, 1975 he entered the M.I.T.-W.H.O.I. Joint Program in Oceanography as a candidate for the degree of Doctor of Philosophy.

Publications:

Sclater, J.G. and J. Crowe, Oceanic heat flow, Rev. Geophysics and Space Physics, 13, 536-538, 547-548, 1975.

Sclater, J.G., J. Crowe and R. N. Anderson, On the reliability of oceanic heat flow averages, J. Geophys. Res., 81, 2997-3006, 1976.

Purdy, G.M., H. Schouten, J. Crowe, D.L. Barrett, R.K.H. Falconer, G.B. Udintsev, N.A. Marova, V.M. Litvin, G.M. Valyashko, V.M. Markushevich and V.V. Zdoroven, IPOD survey area AT-6: a site survey, In: Melson, W.G., P.D. Rabinowitz, et al., Initial Reports of the Deep Sea Drilling Project, 45, 23-48, Washington (U.S. Government Printing Office), 1978.

Sclater, J.G. and J. Crowe, A heat flow survey at anomaly 13 on the Reykjanes Ridge: a critical test of the relation between heat flow and age, J. Geophys. Res., 84, 1593-1602, 1979.

ACKNOWLEDGEMENTS:

I would like to express my deep gratitude to Richard P. Von Herzen and John G. Sclater for their creative guidance and inexhaustible patience. I am grateful for the opportunity to have worked with them. Their example will always mean a great deal to me. The efforts of the other members of my thesis committee are appreciated. Armand J. Silva, Russell McDuff and Barry Parsons provided constant encouragement, timely advice and useful criticism.

Ken Green helped with the collection, reduction and interpretation of the heat flow data and certainly influenced the final form of the thesis. Hans Schouten provided invaluable assistance during the early stages of the project. Woolcott Smith provided remedial lessons in error analysis. Linda Meinke helped sort out numerous computer crises. Victor Zlotnicki, Steve Hellinger and Adolfo Figueroa-Vinas were always willing to assist with mathematical or computer problems. The staff and students at the Marine Geomechanics Lab at URI offered extensive support during my geomechanical studies there. D. Gillette and J. Pierson were always ready to bail me out of a bureaucratic hassle.

I want to give due credit to the friendship and intellectual stimulation I have shared with my fellow students especially Anne Trehu, Peter Goreau, Claude Jaupart, John Nabelek and Mark Kurz. I am grateful to Janet Billane, Roberta Towner and Larry Smith for their friendship and support. And last, but certainly not least, I wish to thank my parents for their continuous encouragement and assistance throughout my college career.

ABSTRACT:

The equatorial Pacific heat flow low, a major oceanic geothermal anomaly centered on the equatorial sediment bulge, was investigated using deeply penetrating heat flow probes (6-11 meters penetration) within three detailed surveys (400 km^2) and along over 10,000 km of continuous seismic profiles (CSP). Previous heat flow measurements in this region defined a broad region characterized by a heat flux well below 1 HFU. We report 98 new measurements collected during cruises PLEIADES 3 and KNORR 73-4 that verify the anomalous nature of the heat flux and also define non-linear temperature gradients (concave down). Temperature field disturbances due to perturbations of a purely conductive heat transport regime are incapable of suitably explaining either of these observations. A simple model incorporating heat transport by both conduction and fluid convection through the sediments fits the observations. A volume flux of (hydrothermal) fluid in the range of 10^{-6} to 10^{-5} cm^3/sec/cm^2 (0.1 liter/yr/cm^2) is required. The sense of the flow for all measurements exhibiting non-linear gradients is upward out of the sediment column; no evidence for the recharging of the system was observed.

Investigation of a well-defined boundary of the low zone at 4°N and 114°W showed a transition from low and variable heat flow to values compatible with thermal models that correlated with a change in the nature of the basement from rough to smooth. A few outcrops occur in the area of rough basement, but otherwise the region is well-sedimented (greater than 200 meters). Measurements within a detailed survey centered at this transition showed a dramatic increase in heat flow from 1.21 HFU to values greater than 3 HFU over a horizontal distance of 10 km. A similar transition from non-linear to linear temperature gradients was not observed as nearly every measurement

was non-linear.

Heat flow measurements located in well-sedimented, outcrop-free areas (A environments) were associated with linear gradients and a heat flux greater than 1 HFU, however, several of these values were well below the theoretical heat flow for the appropriate age crust. Values measured in environments other than A exhibited variable heat flow and non-linear gradients. The average value of measurements located in A environments within the equatorial Pacific heat flow low was 1.37±0.27 HFU. The previously reported average was 0.92±0.48 HFU based on several measurements from L-DGO cruise VEMA 24-3.

The average heat flow measured at a survey located outside the low heat flow zone on crust of 55 ±5 m.a. was 1.76 ±0.30 HFU which is in good agreement with the theoretical value of 1.60. The measurements in this survey were not located in A environments suggesting that crustal convection has ceased or is greatly attenuated within crust of this age.

Error analysis of the geothermal data reduction using the convective/conductive heat transport model suggests that the volume flux parameter is sensitive to temperature measurement errors greater than a few millidegrees. Volume fluxes less than 10^{-7} cm/sec are difficult to distinguish from the purely conductive case assuming instrumental accuracies of 0.001°C. Resolution of the volume flux deteriorates as heat flow decreases and is poor for values less than 0.5 HFU. A detailed survey located within the low zone confirmed previous measurements of low heat flow, however, due to the low value of heat flow (about 0.5 HFU) the small-scale variability could not be clearly defined.

Estimated profiles of lithostatic stress and sediment permeability with

CHAPTER I

Introduction and Overview

INTRODUCTION:

Thermal models which account for the subsidence of ocean ridges also predict the decay of heat flow with distance from spreading centers, i.e. heat flow is inversely proportional to the square root of age (Lister, 1977). Average values of conductive heat flow measurements in well-sedimented basins are generally in agreement with the thermal models (Sclater et al., 1976). Thick sequences of "impermeable" sediment draping the basement confine hydrothermal circulation to the crust. In this situation the average heat flow is representative of the geothermal flux at depth. Where a thick sediment blanket is perforated by outcropping basement, low and scattered heat flow is observed.

Within this framework, observations from the equatorial Pacific Ocean stand out as anomalous. A broad region of low heat flow, well below that predicted by the thermal models, is centered on the equatorial Pacific sediment bulge, which is an extensive accumulation of pelagic sediments exceeding 500 meters in thickness at some points. Recent deeply penetrating heat flow stations (6-11 meters) in this zone have measured non-linear temperature gradients. Similar observations in the Indian Ocean have been interpreted as resulting from heat transport by both conduction and convection through the sediment column (Anderson et al., 1979).

As of yet, no model successfully explains the observed heat flow in the equatorial Pacific. The low zone contradicts models which are the basis of all thermal subsidence studies (i.e. oceanic crust, continental margins, old ocean basins, aseismic ridges) and raises serious questions concerning the validity of ages assigned to oceanic and marginal sea crust based on heat flow

measurements alone.

Analysis of the non-linear temperature gradients using models of heat transport by both convection and conduction through the sediment column require fluid velocities that are quite large, 10^{-6} to 10^{-5} cm/sec. Such high rates would certainly alter present concepts in such fields as interstitial pore water chemistry, the physical properties of sediments and sediment diagenesis as well as create perhaps an insurmountable problem for the disposal of nuclear waste within the seabed.

ORGANIZATION OF THESIS:

This thesis is a collection of three papers examining problems related to the geothermal regime of the equatorial Pacific. The basic objectives of this research are (a) to gain insight into the mechanisms controlling the flow of heat through the floor of the equatorial Pacific Ocean and (b) to critically evaluate estimates of fluid flow through the sediment column based on non-linear temperature gradients.

In Chapter II the basic heat flow problem is discussed. Previous geothermal observations in the equatorial Pacific are reviewed as well as the tectonic and geological setting. Two cruises, KNORR 73-4 and PLEIADES 3, were conducted through the anomalous region during which 98 new heat flow measurements were made, 63 penetrating to depths greater than six meters. The geological environment of these measurements, consisting of sediment thickness and basement topography, were identified from over 10,000 km of continuous seismic profiling (CSP). Because the measurements within the equatorial Pacific prior to these two cruises consist of widely spaced individual values,

the small-scale variability of the heat flow field was investigated in three detailed surveys each covering approximately 400 km^2. Thermal conductivity was measured on 16 cores.

The existence of non-linear temperature gradients has been observed in other deep-sea basins (Anderson et al., 1979) as well as at active spreading centers (Williams et al., 1979). These non-linear gradients have been associated with the flow of fluid through the sediment cover driven by convection located within the crust. A model consisting of the transport of heat by both conduction and convection was applied to the new geothermal data and studied with standard error analysis techniques. Statistical studies show that fluid flows less than 10^{-7} cm/sec cannot be distinguished from the case of no flow. At values of heat flow less than 0.5 HFU, flow estimates appear to be unreliable.

The morphology of the equatorial Pacific sediment bulge was found to be more complex than previously suggested. Numerous outcrops and extensive regions of rough basement topography are associated with en-echelon fracture zones related to a complicated tectonic evolution involving a series of ridge-jumps. CSP data demonstrates the relationship between heat flow and the geological environment. Where the basement is smooth and draped with thick sediments, higher heat flow is observed.

In an attempt to constrain the magnitude of the pressure gradients necessary to drive the proposed fluid convection, geomechanical properties (especially permeability and consolidation) of sediments recovered from several piston cores on PLEIADES 3 and KNORR 73-4 were studied. Since the proposed fluid flux should also affect other processes controlled by

diffusion, a field study of the pore water geochemistry was carried out at piston core sites that exhibited geothermal evidence of fluid motion.

Chapter III presents the results of a laboratory study of the permeability and consolidation characteristics of biogenic sediments recovered from the equatorial Pacific sediment bulge. The laboratory measurements of biogenic sediment permeability show the equatorial Pacific sediment bulge to be at least an order of magnitude more permeable than red clays from the North Pacific. The consolidation studies did not find evidence of widespread underconsolidation which would result in the case where the overburden stress due to lithostatic loading is compensated by excess pore pressures due to vertical fluid motion. In addition, estimates of the balance between lithostatic stress and the hydraulic fluid pressures necessary to maintain the fluid flow are discussed in Chapter II and show that volume fluxes greater than 2×10^{-6} cm/sec will result in pore pressures greater than the overburden stress.

In Chapter IV the results of a field study of volume flux estimates based on both geothermal and chemical pore water profiles is presented. The chemical tracer is sulfate. Comparison of these estimates show the chemical estimate to be three orders of magnitude less than the geothermal.

The low heat flow and non-linear gradients cannot be explained using conductive models. The sense of the fluid flow suggested by the observed temperature gradients is upward out of the sediment column. No evidence of recharge of the system was found. Heat transport models that include the movement of fluid through the sediment pore structure infer pressure gradients that exceed the lithostatic stress. Independent estimates of the volume flux

based on pore water chemistry profiles do not support the geothermal estimates. We feel strongly that the large values of volume flux estimated from the geothermal data are difficult to support and should not be accepted as a valid heat transport mechanism until strong evidence, independent of the geothermal data, such as in-situ pore water chemical profiles or in-situ pore water pressure measurements are obtained. Alternative explanations for the observations include disturbances resulting from the deployment of the heat flow probe or incorrect estimates of sediment permeability due to unrepresentative samples or failure to reproduce in-situ conditions in the laboratory.

BIBLIOGRAPHY:

Anderson, R. N., M.A. Hobart and M.G. Langseth, Geothermal convection through oceanic crust and sediments in the Indian Ocean, Science, 204, 828-832, 1979.

Lister, C.R.B., Estimators for heat flow and deep rock properties based on boundary layer theory, Tectonophysics, 41, 157-171, 1977.

Sclater, J.G., J. Crowe and R.N. Anderson, On the reliability of oceanic heat flow averages, J. Geophys. Res., 81, 2997-3006, 1976.

Williams, D.L., K.E. Green, T.H. van Andel, R.P. Von Herzen, J.R. Dymond and K. Crane, The hydrothermal mounds of the Galapagos Rift: observations with DSRV Alvin and detailed heat flow studies, J. Geophys. Res., 84, 7467-7484, 1979.

CHAPTER II

The Eastern Equatorial Pacific Ocean Heat Flow Low:

Evidence of Hydrothermal Circulation Within 15 to 40 Ma Crust

by

John Crowe

Dept. of Geology and Geophysics
Woods Hole Oceanographic Institution, Woods Hole, MA 02543

Dept. of Earth and Planetary Sciences
Massachusetts Institute of Technology, Cambridge, MA 02139

Richard P. Von Herzen

Dept. of Geology and Geophysics
Woods Hole Oceanographic Institution, Woods Hole, MA 02543

and

Kenneth E. Green
Dept. of Geology and Geophysics
Woods Hole Oceanographic Institution, Woods Hole, MA 02543

Dept. of Earth and Planetary Sciences
Massachusetts Institute of Technology, Cambridge, MA 02139

ABSTRACT:

The equatorial Pacific heat flow low, a major oceanic geothermal anomaly centered on the equatorial sediment bulge, was investigated using deeply penetrating heat flow probes (6-11 meters penetration) within three detailed surveys (400 km^2) and along over 10,000 km of continuous seismic profiles (CSP). Previous heat flow measurements in this region defined a broad region characterized by a heat flux well below 1 HFU. We report 98 new measurements collected during cruises PLEIADES 3 and KNORR 73-4 that verify the anomalous nature of the heat flux and also define non-linear temperature gradients (concave down). Temperature field disturbances due to perturbations of a purely conductive heat transport regime are incapable of suitably explaining either of these observations. The application of a simple model incorporating heat transport by both conduction and convection through the sediment is successful, however, a volume flux of hydrothermal fluid in the range of 10^{-6} to 10^{-5} cm/sec is required. The sense of the flow for all measurements exhibiting non-linear gradients is upward out of the sediment column; no evidence for the recharging of the system was observed.

Investigation of a well-defined boundary of the low zone at 4°N and 114°W showed a transition from low and variable heat flow to values compatible with thermal models that correlated with a change in the nature of the basement from rough to smooth. A few outcrops occur in the area of rough basement, but otherwise the region is well-sedimented (greater than 200 meters). Measurements within a detailed survey centered at this transition showed a dramatic increase in heat flow from 1.21 HFU to values greater than 3 HFU over a horizontal distance of 10 km. A similar transition from non-linear to linear temperature gradients was not observed as nearly every measurement

was non-linear.

Heat flow measurements located in well-sedimented, outcrop-free areas (A environments) were associated with linear gradients and a heat flux greater than 1 HFU, however, several of these values were well below the theoretical. Values measured in environments other than A exhibited variable heat flow and non-linear temperature gradients. The average value of heat flow measurements located in A environments within the equatorial Pacific heat flow low was 1.37 ±0.27 HFU. The previously reported average was 0.92 ±0.48 HFU based on several measurements from L-DGO cruise VEMA 24-3.

The average heat flow measured at a survey located outside the low heat flow zone on crust of 55 ±5 m.a. was 1.76 ±0.30 HFU which is in good agreement with the theoretical value of 1.60. The measurements in this survey were not located in A environments suggesting that crustal convection has ceased or is greatly attenuated within crust of this age.

Error analysis of the geothermal data reduction using the convective/conductive heat transport model suggests that the volume flux parameter is sensitive to temperature measurement errors greater than a few millidegrees. Volume fluxes less than 10^{-7} cm/sec are difficult to distinguish from the purely conductive case assuming instrumental accuracies of 0.001°C. Resolution of the volume flux deteriorates as heat flow decreases and is poor for values less than 0.5 HFU. A detailed survey located within the low zone confirmed previous measurements of low heat flow, however, due to the low value of heat flow (about 0.5 HFU) the small-scale variability could not be clearly defined.

Estimated profiles of lithostatic stress and sediment permeability with

depth in the equatorial sediment bulge based on laboratory measurement of the

consolidation and permeability of sediments from the area, suggested that

excess pore pressures at depth exceeding the lithostatic stress are necessary

to support volume fluxes greater than about 2×10^{-6} cm/sec. Comparison of

volume flux rates based on profiles of temperature and pore water chemistry

show the chemical rates to be three orders of magnitude less than the

geothermal.

Geomechanical and geochemical studies fail to support the simple

convection/conduction model. The interpretation of non-linear temperature

gradients suggest a volume flux out of the sediment column with no evidence of

recharge occuring. No independent evidence of the movement of fluid through

the sediment column was found. It may be possible that a temperature bias

introduced by the deployment of the temperature probe may result in erroneous

temperature gradients and overestimated volume fluxes.

INTRODUCTION:

Heat flow measurements within the equatorial Pacific Ocean define a

large region with an average value well below that predicted by reasonable

thermal models of ocean crust subsidence. The mechanisms responsible for this

broad region of low heat flow have not been suitably explained. Attempts to

study the variablility of oceanic heat flow measurements have recognized this

area as anomalous (Sclater et al., 1976; 1980). Recent deeply penetrating

temperature measurements have shown non-linear thermal gradients in the

uppermost 10 meters of the sediment column (Von Herzen et al., 1979). Similar

gradients were reported by Anderson et al. (1979) in the Indian Ocean, and

Langseth and Herman (in press) in the Brazil Basin. They have been interpreted to be due to heat transport by both conduction and fluid convection through the sediment.

We have investigated the variability of the heat flow measurements in the equatorial Pacific Ocean on both a broad regional scale and a fine scale of detailed surveys (400 km^2). The available data base consists of over 500 heat flow values including 65 new measurements made during the WHOI cruise KNORR 73-4 and 33 new measurements made during the Scripps cruise PLEIADES 3.

THE EQUATORIAL PACIFIC OCEAN:

The equatorial Pacific heat flow low is outlined in Figure 1 with a bold line. Although the heat flow throughout the equatorial Pacific region exhibits great scatter, we have arbitrarily defined the boundary of this anomalous region by a contour of heat flow measurements made prior to 1976 (circles in Figure 1) of value less than 1.0 heat flow unit (1 HFU = 10^{-6} cal/cm^2-sec). However, values greater than 1.0 HFU have been observed within this area, including several measurements made during the more recent KNORR 73-4 and PLEIADES 3 cruises (squares in Figure 1). The equatorial Pacific heat flow low was first identified by Von Herzen and Uyeda (1963) in their broad-scale reconnaisance of the distribution of heat flow in the eastern Pacific Ocean. Subsequent investigations (Langseth et al., 1965, 1971; Vacquier et al., 1967; Bookman et al., 1972; Von Herzen and Anderson, 1972) confirmed the nature and delineated the boundaries of this region. The majority of the data within this area consists of widely-spaced measurements made with short probes penetrating to only two or three meters. For most of

Figure 1. Map of heat flow data within the Equatorial Pacific Ocean superimposed on the bathymetric map of Chase (1975). The Equatorial Pacific heat flow low is outlined with a bold solid line. Bathymetry is in corrected fathoms. All short probe and piston core stations prior to 1976 and the pogo probe stations of PLEIADES 3 are indicated by solid dots. Temperature gradient measurements penetrating to greater than six meters from PLEIADES 3 and KNORR 73-4 are represented by squares. Heat flow values are in heat flow units (10^{-6} cal/cm^2 sec). Three detailed surveys from PLEIADES 3 and KNORR 73-4 are marked with large open squares. Multiple penetration heat flow stations associated with the investigation of the low heat flow boundary in the vicinity of 4°N, 114°W are show by small open squares.
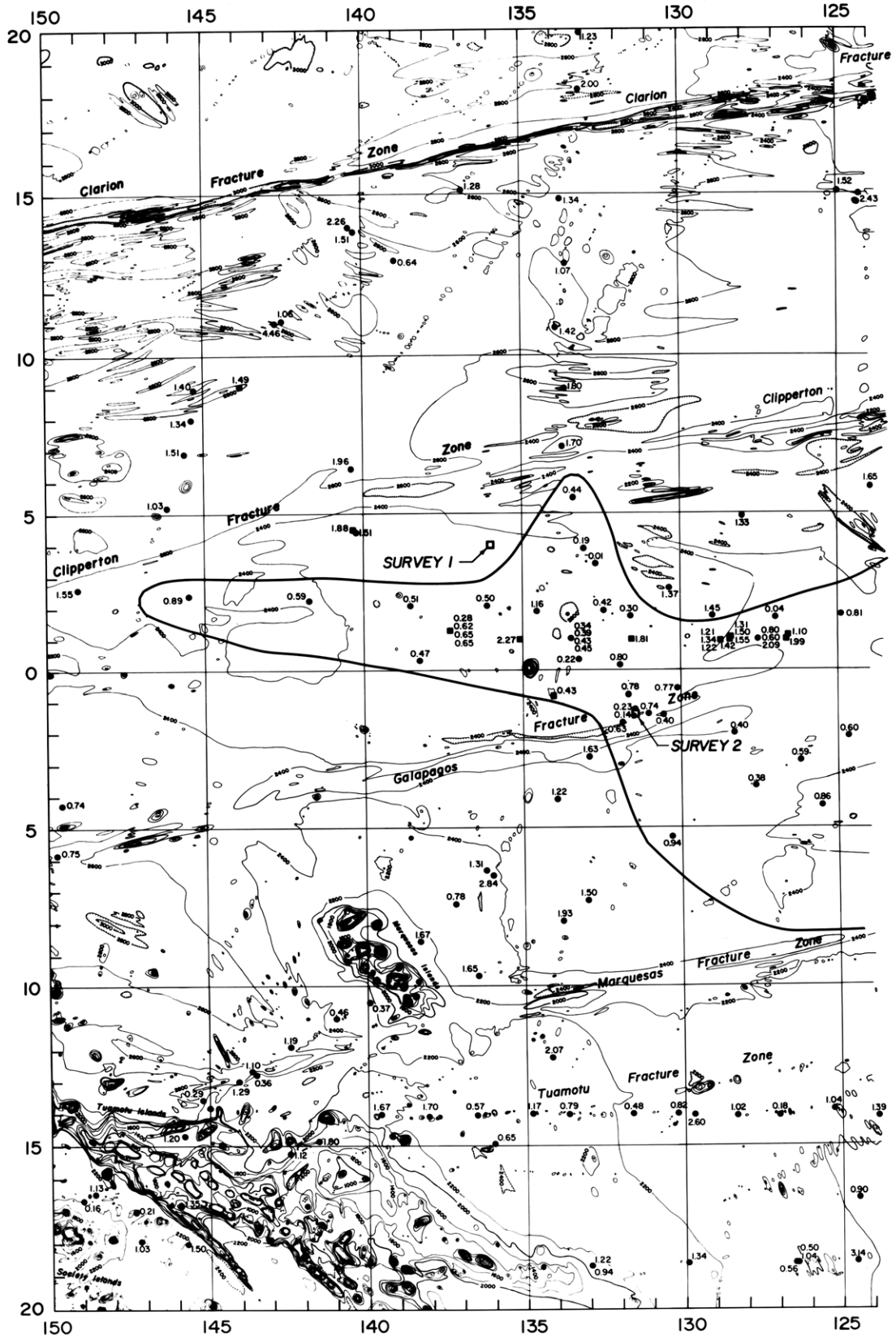
these measurements the geological environment (sediment thickness and basement topography) is poorly known, and the linearity of the temperature gradient is not well determined because of the relatively shallow penetration and few temperature sensors. New measurements reported in this paper extending to between six and eleven meters sub-bottom have identified non-linear temperature gradients that show significant concavity downwards. In Figure 2 temperature and thermal conductivity as a function of depth are plotted for deeply penetrating piston core measurements from PLEIADES 3 and KNORR 73-4. Several mechanisms are capable of producing both the observed low heat flow and the non-linear gradients. We discuss these in more detail below, and critically examine one mechanism in detail, the transport of heat resulting from the circulation of seawater through the sediment layer driven by convection originating within the crust.

A systematic theoretical and experimental relationship between the heat flow and topography of the sea floor consistent with simple plate tectonics models has been developed over the past decade, most recently refined by Parsons and Sclater (1977). Heat flow data in the equatorial Pacific low heat flow zone show considerable scatter, making comparison with theoretical models very difficult, but it is clear that the heat flow in this region is significantly different than that predicted by the models. Lister (1970, 1972) and Talwani et al. (1971) suggested that at active ridge crests, large quantities of heat are removed as the newly formed crust is cooled by hydrothermal convection. Recently this phenomenon has been observed at the Galapagos Spreading Center (Corliss et al., 1979) and at the East Pacific Rise at $21^{o}N$ (Spiess et al, 1980). Two studies (Williams et al., 1979; Green et

Figure 2. Temperature versus depth for the piston core stations of KNORR 73-4 and PLEIADES 3. Thermal conductivities versus depth are plotted to the right of the temperature gradients for the stations where they exist. The horizontal scale divisions are 0.1°C for the temperature data and 0.2 x 10^{-3} cal/cm-sec-$^{\circ}$C for the thermal conductivity data. Errors bars assigned to the temperature data are shown. The lines drawn through the temperature data represent the best fit of a simple conductive/convective thermal model (see text).
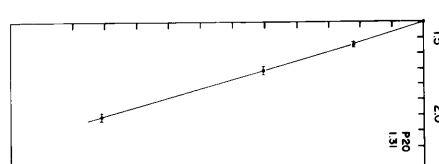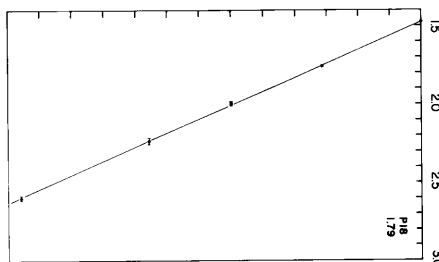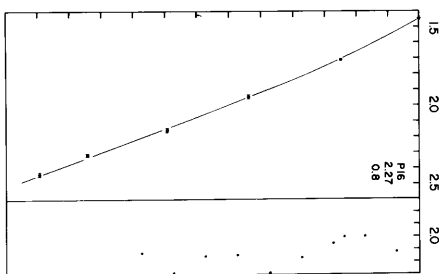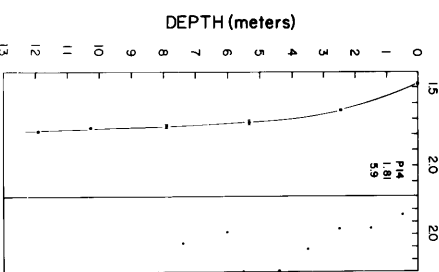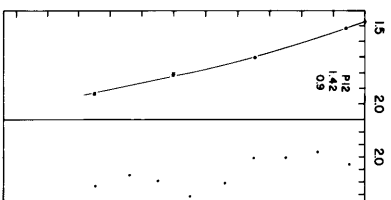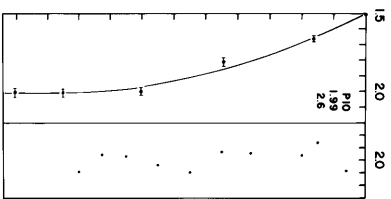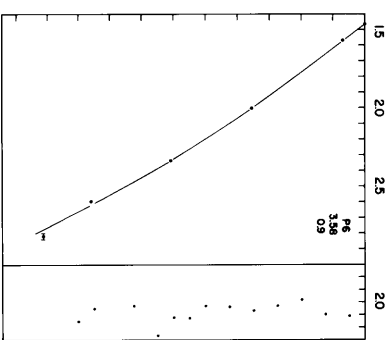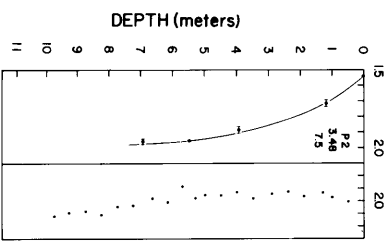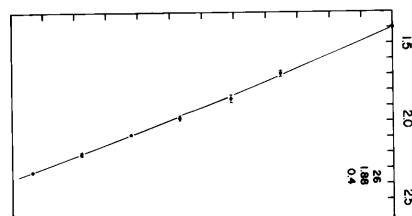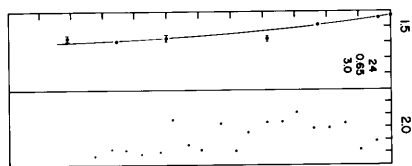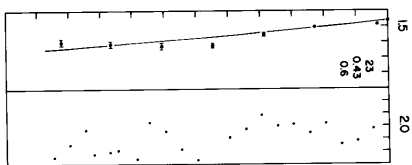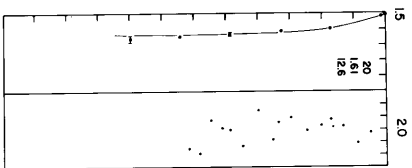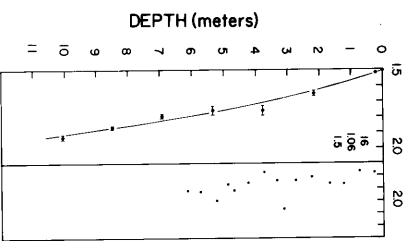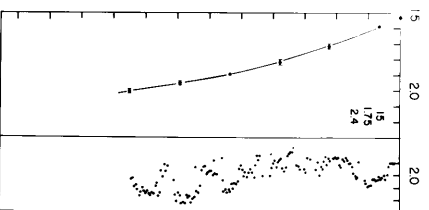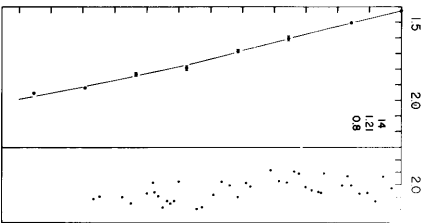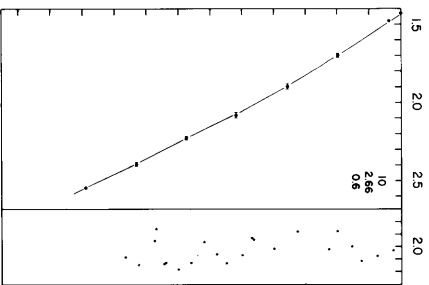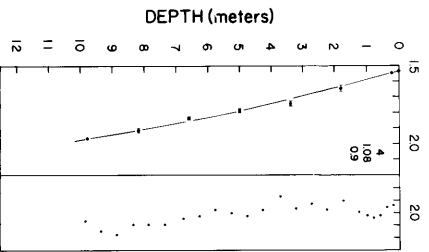
al., 1980) of the heat flow south of the Galapagos Spreading Center showed extensive evidence of hydrothermal convection in crust of younger than approximately 1.0 m.y.

Sclater et al. (1976) developed a model to account for the observed heat. flow variability and applied it to the data in the Pacific Ocean. Where thick sequences of "impermeable" sediment totally cover the ocean floor, hydrothermal circulation is confined to the crust, reducing the scatter in values and resulting in an average heat flow closer to the theoretical. Their results and the results of Sclater and Crowe (1979) are shown in Figure 3 where both theoretical and observed average heat flow are plotted versus age. The equatorial Pacific Ocean clearly stands out as anomalous. In Figure 4 the Pacific Ocean heat flow data located from 20°S to 20°N between the East Pacific Rise and 150°W is plotted in two histograms as % population. The entire data set is divided into (A) the data located within the low heat flow zone and (B) the remaining values outside the low zone situated on oceanic crust. The anamolous nature of the low zone is evident from comparing these histograms.

POSSIBLE REASONS FOR LOW HEAT FLOW:

Several mechanisms capable of explaining the observed non-linear and low heat flow data in the eastern equatorial Pacific exist, some more plausible than others. Among these mechanisms are: (1) recent changes in bottom water temperature, (2) the distortion or movement of deep sea sediment due to large scale slumping or flow (creep) possibly controlled by carbonate dissolution, (3) the effects of high sedimentation rates, (4) heat flow refraction due to

Figure 3. Reliable heat flow averages versus age from Sclater and Crowe, (1979). The dashed region is the equatorial Pacific low zone.
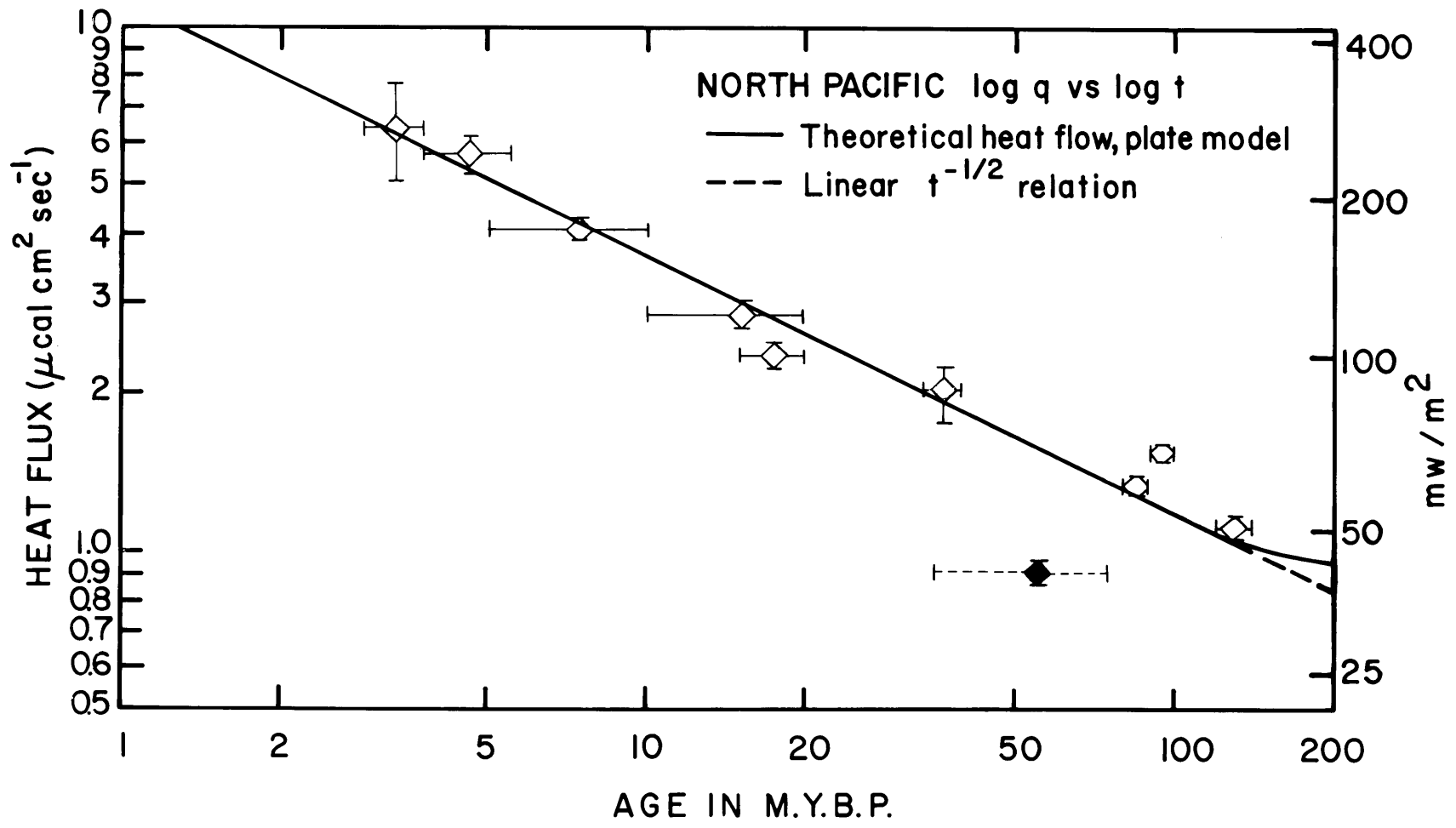
Figure 4.   (A) Histogram of heat flow values within the equatorial Pacific
heat flow low plotted as per cent population versus heat flow value in HFU.
(B) Histogram of all other heat flow values located on oceanic crust west of
the East Pacific Rise in the region $20^{o}N-20^{o}S$ and $100^{o}W-150^{o}W$ plotted
as per cent population versus heat flow.
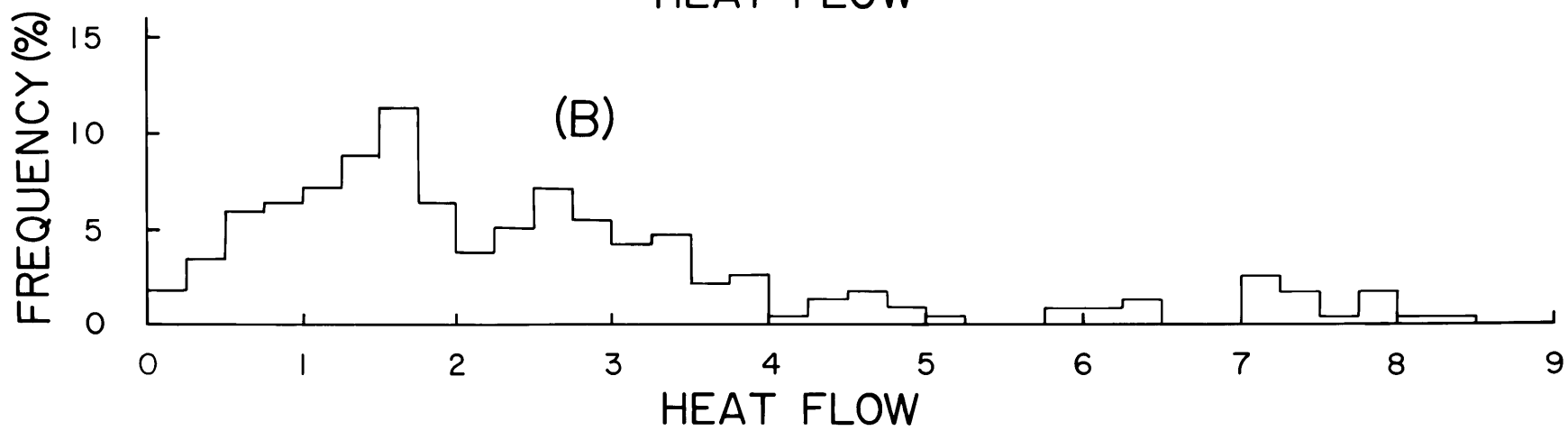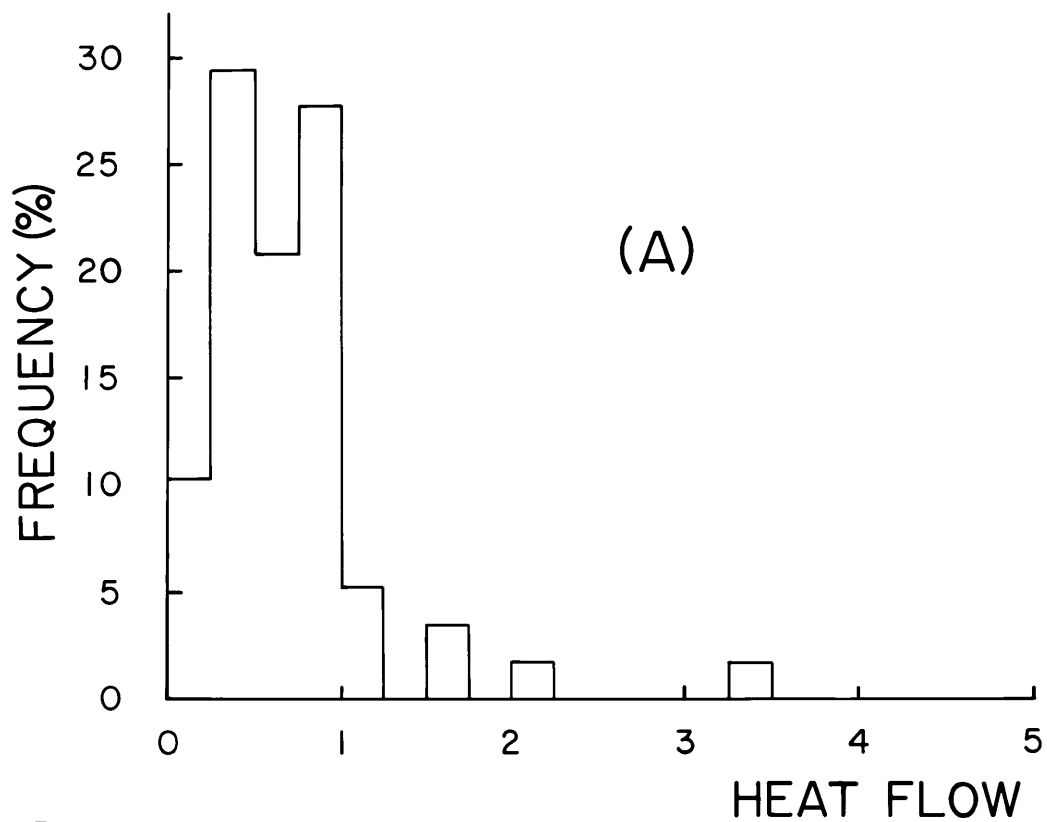
rough topography between basement rock and sediment of different thermal conductivity, (5) the movement of interstitial waters and (6) thermal conductivity variations with depth in sediments.

The effect of bottom water temperature fluctuations has been discussed by Carslaw and Jaeger, 1959 (sec. 2.6). For a periodic perturbation at the seawater/sediment interface the solution is a travelling wave of initial amplitude θ_0 that is exponentially attenuated in amplitude as it penetrates into the medium:

$$\theta = \theta_0 \cos(\omega t - 2\pi z/\lambda - \epsilon) \exp(-2\pi z/\lambda) \tag{1}$$

where ω, λ and ϵ are the frequency, wavelength and phase shift of the surface temperature perturbation. λ is equal to $(4\pi kT)^{1/2}$ where k is the sediment thermal diffusivity and T is the period of the surface temperature perturbation. For a perturbation with a period of a year, λ is about 9 meters, large values for θ_0 on the order of $0.1^{\circ}C$ are necessary to produce the observed non-linear temperature profiles. Such large bottom water temperature changes seem unlikely owing to the long time constant associated with bottom water renewal, 1000-2000 years (Brewer, 1975; Broecker, 1974), and the distant sources of bottom water for this region.

The association of this region with the equatorial biogenic high-productivity zone suggests that the distortion or slumping of sediments might have an effect on the near-surface gradients (Berger and Johnson, 1976). Von Herzen and Uyeda (1963) investigated the thermal consequences of several sedimentary processes. The effect of constant sedimentation rates on

the order of 10^{-4} cm/yr to 10^{-3} cm/yr, the range appropriate for the equatorial Pacific Ocean (Lisitzin, 1972), is quite small. Calculations of the effects of turbidity currents, landslides and sediment erosion suggested that these mechanisms are incapable of adequately accounting for the observed heat flow. With few exceptions, the slope of the seafloor in this region is very slight making widespread large-scale gravity induced sediment movement seem improbable. Slumping induced by earthquake activity is also ruled out by the low seismicity of the region.

The refraction of heat due to thermal conductivity contrasts between basement rock and sediment can account for variations of up to 20% in many areas (Bullard et al., 1956; Von Herzen and Uyeda, 1963; Sclater and Miller, 1969). In the equatorial Pacific heat flow low the difference between the observed average heat flow and the theoretical greatly exceeds 20% and cannot be explained by this mechanism.

Water migration due to either sediment consolidation (Lubimova et al., 1965) or forced convection (Anderson et al., 1979) can successfully explain the observations, however, water expulsion by sediment compaction is at least two orders of magnitude slower than the required volume fluxes (10^{-6} - 10^{-5} $cm^3/sec/cm^2$).

Variations in the thermal conductivity structure will certainly result in producing variability in thermal gradients. If there is a substantial increase or decrease in thermal conductivity over the depth of the measurement, nonlinearities will result. Our modeling of this effect shows that the effect of assuming a constant thermal conductivity structure instead of the true structure cannot explain the observed nonlinearies. For reasonable structures of thermal conductivity, the maximum effect of

substituting a harmonic mean thermal conductivity for the true structure generally increases the heat flow by about 10% and increases the apparent velocity of the pore water by about 20%.

REDUCTION OF DATA:

The low heat flow region is defined with data largely collected prior to 1972 (summarized by Jessop et al., 1975 with additional data reported by Von Herzen and Anderson, 1972 and Anderson et al., 1976). The majority of these measurements consist of shallow penetrations of the sediment layer (less than three meters) with probes equipped with two or three temperature sensors. The local geological environment of many of these stations is obscure owing to the absence of continuous seismic profiling (CSP) and the collection of other detailed data in the vicinity of the measurements.

Data collected on cruises KNORR 73-4 and PLEIADES 3 include heat flow stations where the temperature field was measured to a depth of 12 meters (maximum) with up to seven temperature sensors (described in Von Herzen and Anderson, 1972). Figure 5 is a sketch of a piston core equipped with thermistors showing the position of the temperature sensors relative to the sediment/seawater interface. An underwater camera located in the corehead photographed the seafloor during several stations, enabling the depth of penetration to be estimated independently (McCoy and Von Herzen, 1971). Thermal conductivity was measured on sediment recovered with piston cores using the needle probe technique of Von Herzen and Maxwell (1959). The temperature data was recorded using a digital system on KNORR 73-4, while analog instrumentation (Langseth et al., 1965) was used on PLEIADES 3.

Figure 5. Schematic diagram of the heat flow probe used during KNORR 73-4.
The parameters a and b from equation 5 are shown. The distance from the top
of the recovered sediment core and the sediment/seawater interface is
parameter a. The distance from the bottom of the core head to the
sediment/seawater interface is parameter b. The positions of the temperature
sensors with respect to the bottom of the core head ($\xi = 0$) are ξ_1, ξ_2,
..., ξ_7. The positions of these sensors relative to the sediment/seawater
interface is $z = \xi - b$.

CAMERA/STROBE

COREHEAD

HEAT FLOW
INSTRUMENT

$\xi = 0$

$+\xi$

Seawater

b

$Z = 0$

Sediment

a

$-\xi_1$

$+Z$

RECOVERED
SEDIMENT

$-\xi_2$

$-\xi_3$

OUTRIGGER
THERMISTORS

$-\xi_4$

$-\xi_5$

$-\xi_6$

$-\xi_7$
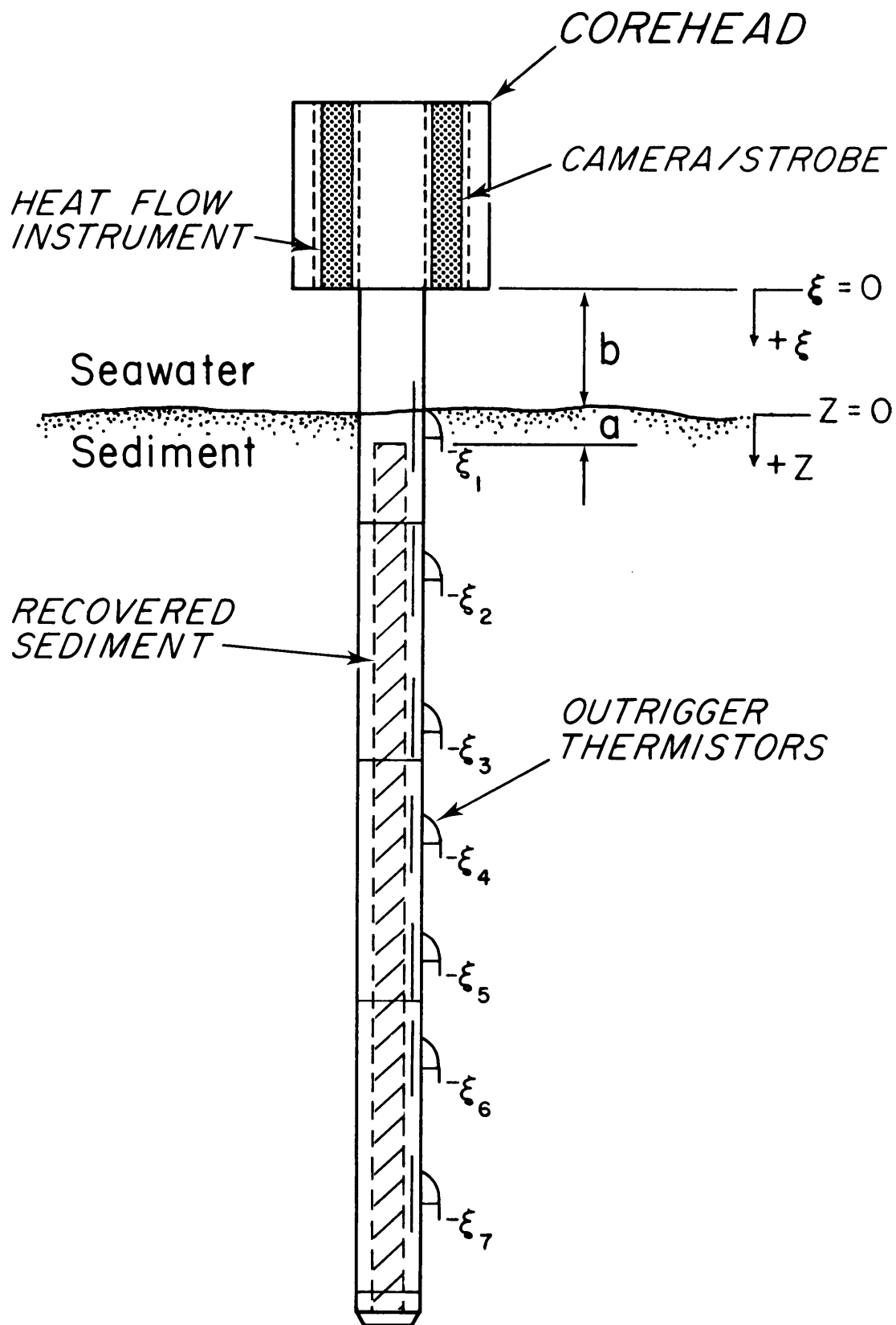
Features of the detailed heat flow variability were revealed within three survey areas in which the majority of the measurements are located.

The procedure followed in reducing the raw digital heat flow data is described by Galson (1979). It is necessary to account for the effects of the frictional heating of the probe caused by its being forced into the sediment. The theoretical decay of this effect, based on a cylindrical probe model (Bullard, 1954; Jaeger, 1956) is rapid at first, with probe temperature quickly approaching equilibrium proportional to the inverse of time. The thermal time constant of the probe, the probe radius squared divided by the sediment thermal diffusivity, is 15 seconds (probe radius is 1/16"). Since this time constant is short compared to the duration of the experiment (6 minutes), a 1/time extrapolation is valid after 1-2 minutes. Errors were assigned to the measured temperatures from both the individual analysis of the decay of each thermistor and the overall instrumental performance. These assigned errors ranged from 1 to 30 millidegrees.

The data is collected as a digital count which is the voltage to frequency (V to F) conversion of the analog output voltage of a Wheatstone bridge. Data is recorded in the form of a twelve bit word, allowing a resolution of 1 in 4096. When 4096 is exceeded, the digital counter rolls over and begins counting from zero. A maximum of 13.5 rollovers is permitted (55296 usable counts). Figures 6 and 7 show the data at station 13, penetration 1. Figure 6 is a plot of digital count versus time before, during and after penetration. There are twelve channels of data (each offset in the figure by 100 counts to avoid overlap) consisting of eight temperature probes, two precision resistor calibration points and a pressure sensor. The vertical

Figure 6. Raw digital data for heat flow station 13-1. The vertical axis is a relative scale showing the magnitude of change in digital count occuring before, during and after probe penetration. The digital count is the voltage to frequency (V to F) conversion of the analog output voltage of a Wheatstone bridge (see text).
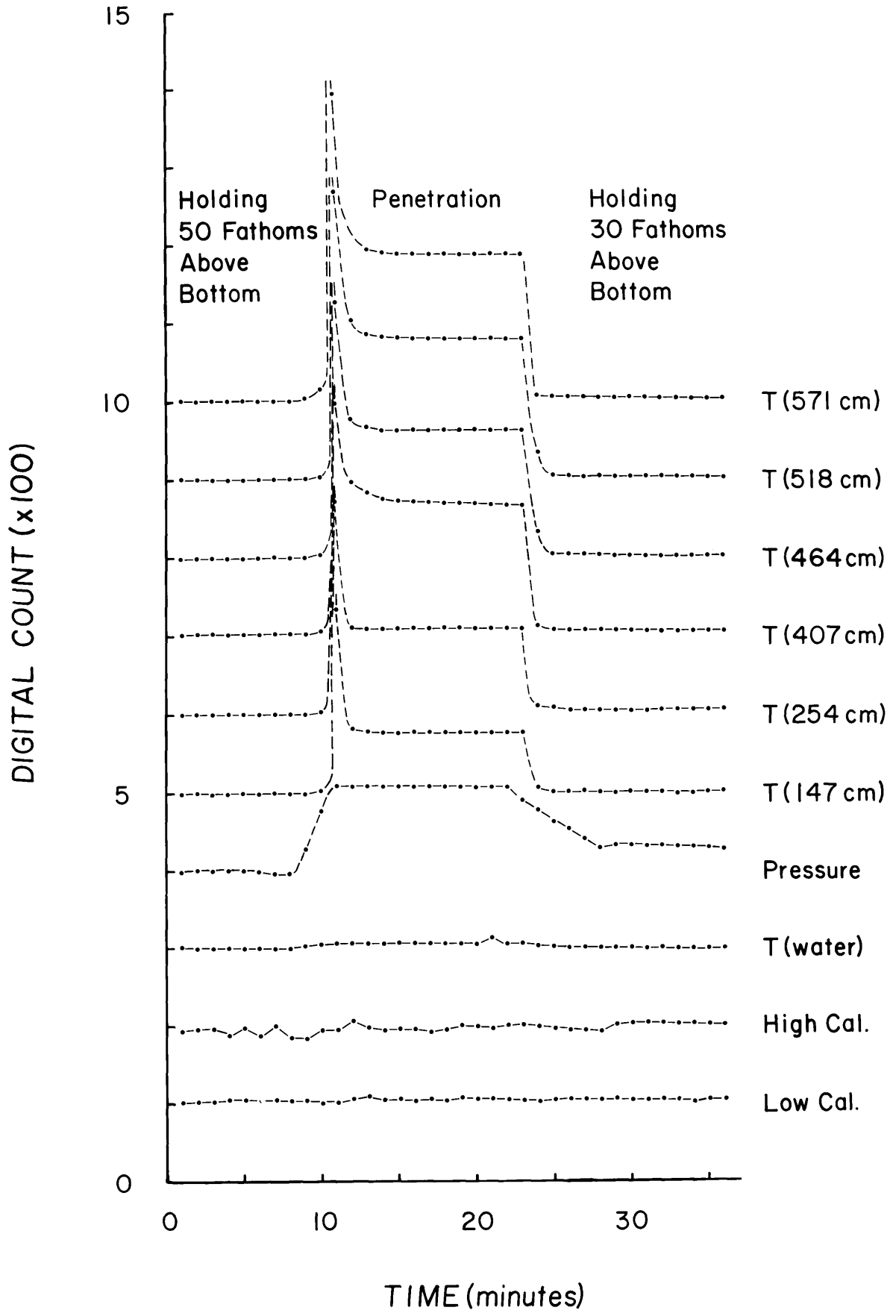
Figure 7. The digital data occuring during penetration for station 13-1

plotted versus the inverse of time. The equilibrium temperatures and range of

errors were assigned subjectively. The digital count representing the

equilibrium temperature is defined as the intersection of the thermal decay

and the vertical line corresponding to the inverse of infinite time. The

range of straight lines that can be drawn through this data is the basis of

the assignment of errors to the equilibrium temperature. These assigned

errors are shown to the right side of the graph. The equilibrium temperature

versus depth profile for station 13-1 is plotted in Figure 28.
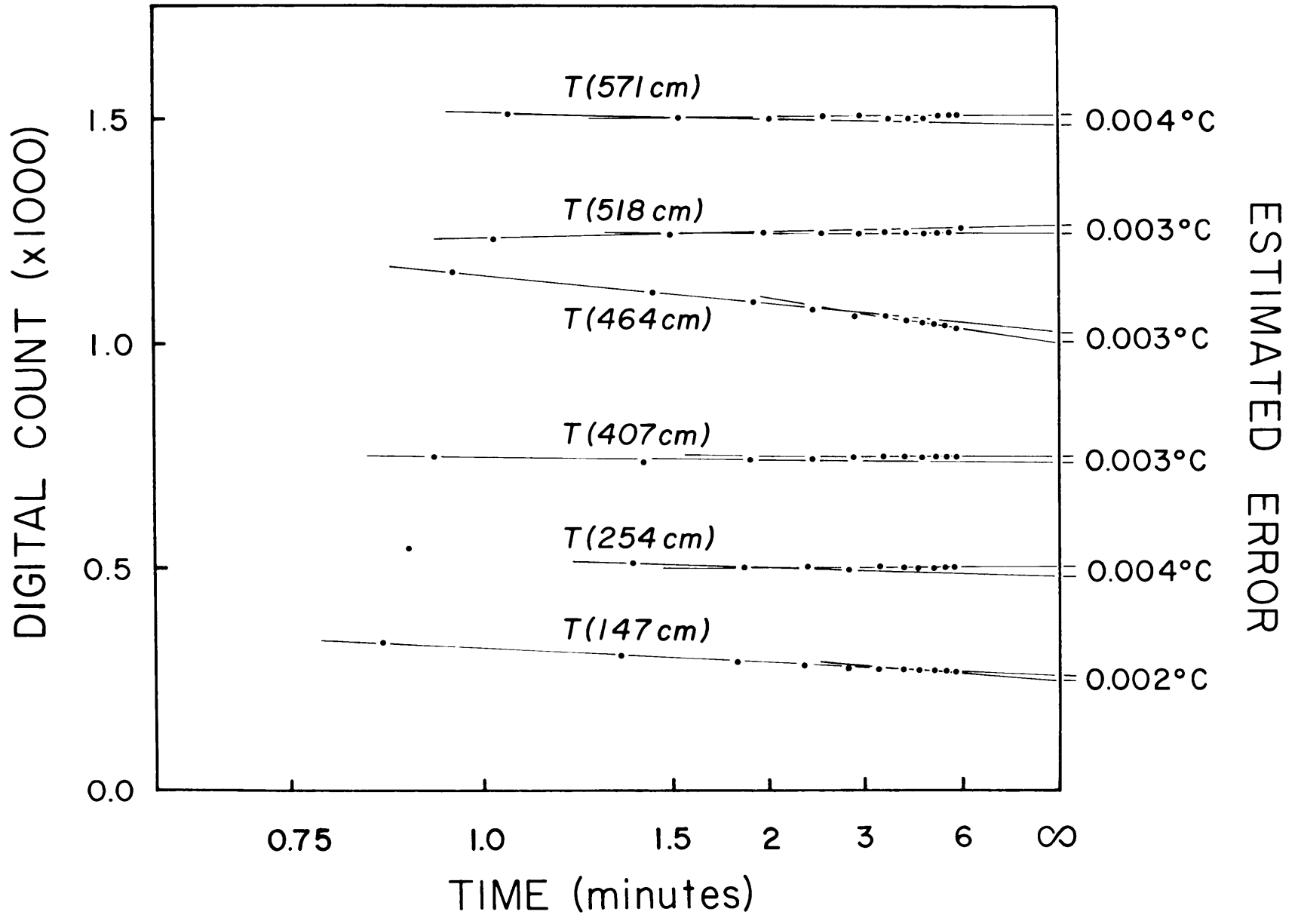
axis is a relative scale showing the magnitude of change in digital count
occuring before, during and after probe penetration. The mean values
corresponding to the upper and lower calibrations in Figure 6 are 9616 and 728
counts respectively. The upper calibration record for this particular station
is 'noisy' by our standards, however, this variability represents a 0.15%
error in the calibration.

In Figure 7 the digital data from Figure 6 is plotted versus the inverse
of time since penetration showing the graphical determination of the
equilibrium temperature and the assignment of experimental error. The digital
count representing the equilibrium temperature is defined as the intersection
of the thermal decay (theoretically a straight line when plotted in this
manner) and the vertical line corresponding to the inverse of infinite time.
The error assigned to the individual temperature measurements is estimated
from the range of lines that can be drawn through the 1/time decay. For some
stations the decay of the temperature disturbance associated with penetration
did not produce plots as linear as that shown in Figure 7. This is probably
the result of some thermal disturbance from the core or probe but our analysis
incorporates the larger errors associated with such non-linear decays.

Our conceptual model for the data is similar to that of Bredehoeft and
Papadopulos (1965) in that heat is transported both conductively and
convectively through the porous sediment. In this model, the general equation
of heat conservation for transport in the vertical direction is

$$0 = \underline{\nabla} \cdot \underline{q} = -k \frac{d^2T}{dz^2} + W \frac{dT}{dz} \tag{2}$$

where q is the vertical heat flux, z is vertical distance (positive downwards), W is the vertical volume flux (positive upwards), k is the sediment thermal diffusivity ($= K/\rho c_p$), ρ is fluid density, c_p is fluid heat capacity and K is the thermal conductivity of the saturated bulk sediment. Subject to the boundary condition T = 0 at z = 0 and imposing q to be constant (q_o) everywhere, the solution to equation 2 for constant thermal conductivity (K = constant) is

$$T(z) = \frac{q_o}{\rho c_p W} [1 - \exp(-Wz/k)] \qquad (3)$$

(Sleep and Wolery, 1978). This model is illustrated in Figure 8 (from Williams et al., 1979) showing the relationship of the resulting non-linear temperature gradient to the direction of fluid flow. For the situation where K is a function of depth, the solution can be generalized to

$$T(z) = \frac{q_o}{\rho c_p W} [1 - \exp(-\rho c_p W \int_0^z R(\zeta) \, d\zeta)] \qquad (4)$$

where R(z) is thermal resistivity (1/K(z)). The integral $\int_0^z R(\zeta) d\zeta$ can be numerically approximated by a summation assuming a layered conductivity model. For m layers each of thickness Δz_n and of thermal resistivity R_n, the integral can be rewritten $\Sigma R_n \Delta z_n$. The formulation of the solution as equation 3 or 4 allows the determination of the values of q_o and $\rho c_p W$ that best fit the observed data. There is uncertainty as to the depth of penetration of the probe resulting in an ambiguity in the location of the temperature sensors relative to the seawater/sediment interface. As a result,

Figure 8. Schematic diagram of parameters Q and W from Williams et al.
(1979). The resulting sense of the temperature gradient for flow into and out
of the sediment layer is shown.
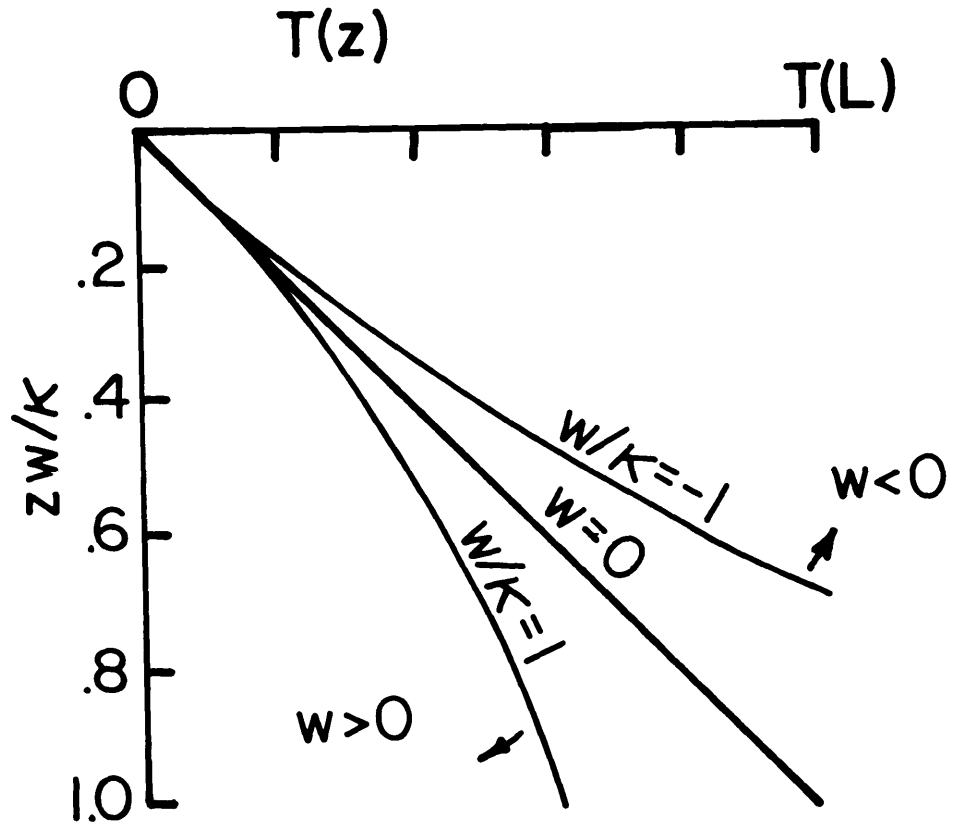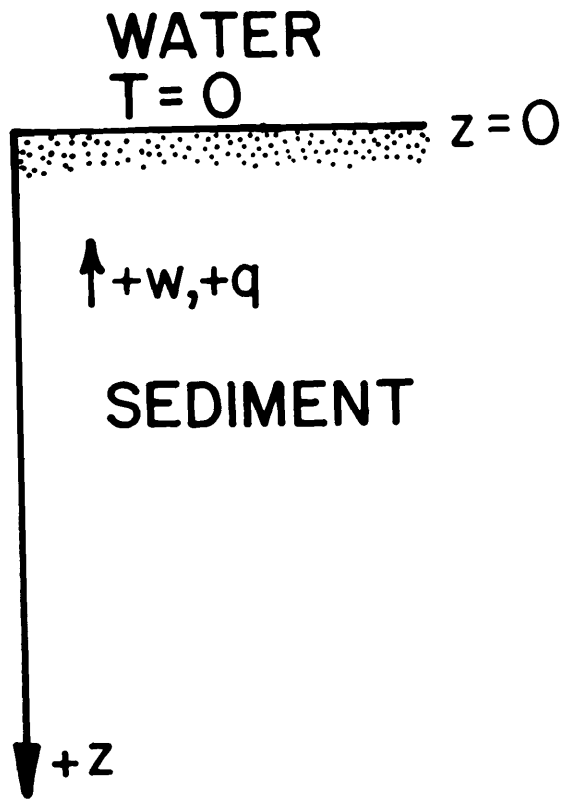
a third parameter, b, shown in Figure 5, can be introduced which is the distance by which the probe falls short of full penetration (b = 0 for full penetration; b > zero for partial penetration). To check this model, the location of the corehead with respect to the seafloor was estimated from corehead photographs. Figure 9 is a photograph taken during penetration at station 10 showing the relationship between the corehead and the seafloor. With one exception, the data for all stations summarized in Table 1 shows good agreement between the independently determined penetrations.

The formulation of equation 4 modified for parameter b is

$$T(\xi) = \frac{q_0}{C} [1 - \exp(-C \int_0^{\zeta-b} R(\zeta) \, d\zeta)] \qquad (5)$$

where $C = \rho c_p W$ and ξ is defined in Figure 5. Since piston coring from a surface ship is not always a precise technique (e.g. McCoy and Von Herzen, 1972), the location of the conductivity measurements determined from the recovered core relative to the seawater/sediment interface can be considered as a fourth parameter, a, shown in Figure 5. In general the length of the recovered core was less than the depth of penetration. The effect of parameter a was found to be significantly less important than the other three parameters, varying on the order of 10 cm. Thereafter parameter a was assumed to equal zero.

At this point we must stress that our use of this model in the data reduction does not imply that we accept the model. Its validity has not been supported by other independent data. However, the majority of our observed temperature gradients are non-linear and the parameter C/K is a useful measure

Figure 9. Corehead photograph showing the position of the piston core (center of photograph) relative to the seafloor during station 10. Note the underwater cables strapped to the side of the core pipe providing an electrical connection between the thermistor probes and the digital recording package located in the corehead (see Figure 5). The 2 meter gravity core that acts as a trigger for the piston core appears in the photograph to the right of the piston core.
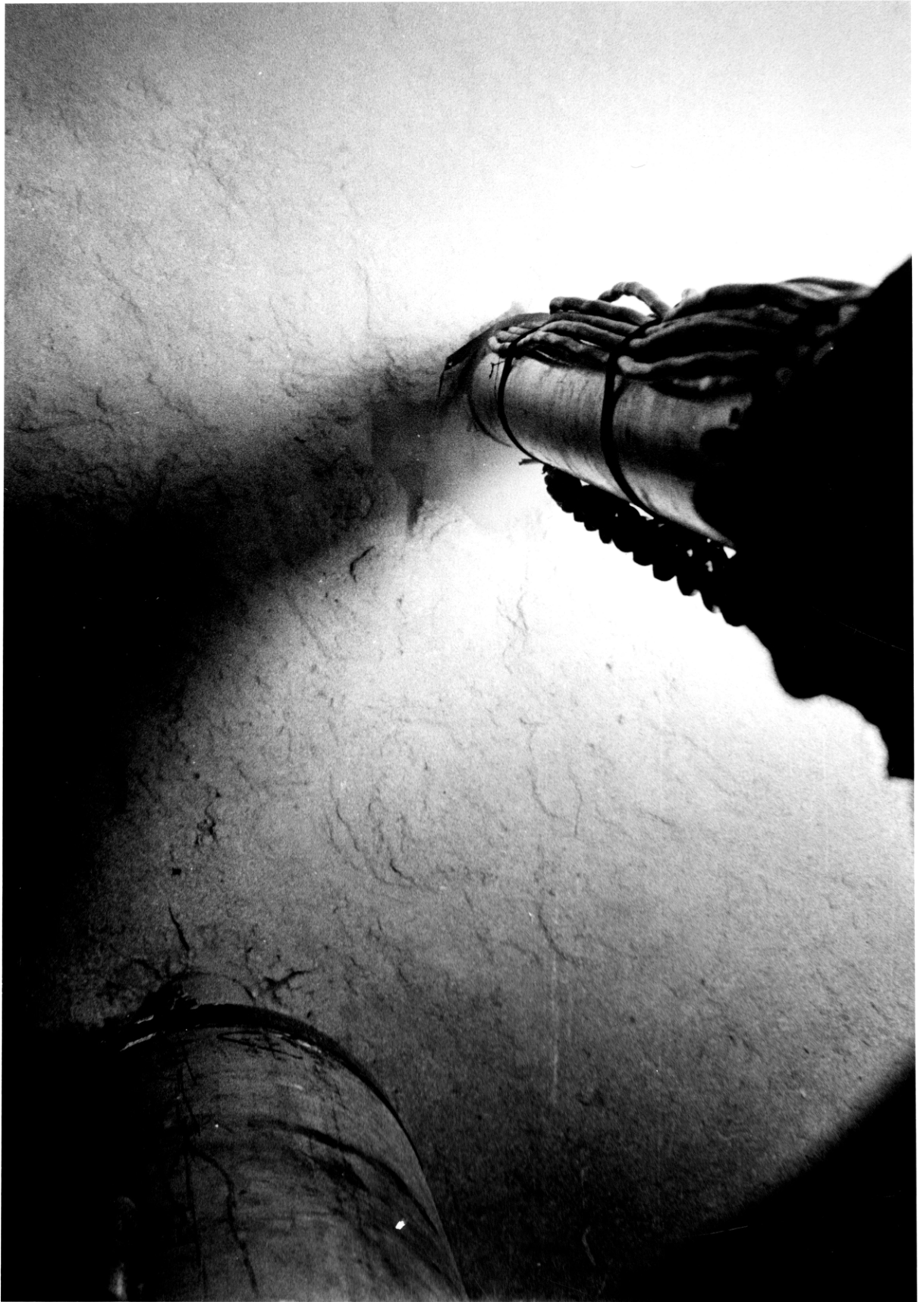
Table 1. Core Head Penetration Summary

Station	Estimated Photographic Value of b [1] (cm.)	Estimated Value of b From Temperature Gradient (cm.)	s.d.
4	116.	185.	13.
5-1	49.	-21.	7.
10	152.	165.	6.
11-1	100.	90.	21.
11-2	149.	164.	43.
15	334	288.	4.
24	185.	124.	47.

[1] Estimated accuracy of ±20 cm.

of this non-linearity (i.e. the e-folding depth). Assuming a value for
sediment thermal diffusivity of 2×10^{-3} cm/sec, the relationship between
e-folding depth, e, and volume flux is $e = 20$ meters-sec^{-1}/W where W is in
units of 10^{-6} cm/sec. The flow model certainly represents a credible heat
transport mechanism, and throughout the paper we freely speak of the volume
flux, however, for all practical purposes we use the terms "volume flux" and
"degree of non-linearity" interchangeably except where stated otherwise.

To determine the best estimate and the range of the model parameters
from our observed data, a weighted least squares fit of equation 5 to the
observed data values by means of stepwise Gauss-Newton iterations on the
parameters Q, C and b was carried out. The formulation of this non-linear
regression method is developed in Appendix I. We obtain from this technique
the best fit parameters, their standard deviations and their correlation with
each other. The results obtained using this non-linear regression program for
the data collected during KNORR 73-4 and PLEIADES 3 are summarized in Tables 2
and 3. The limitations of both our data and the reduction scheme is discussed
in Appendix II.

DISCUSSION OF DATA:

The distribution of heat flow measurements in the equatorial Pacific
Ocean is shown in Figure 1. Although large gaps exist in the coverage of
data, a rough outline of the anomalous low heat flow zone can be drawn (bold
solid line). Many of the values in this region are below 1 HFU (Figure 4).
Measurements made prior to those reported in this paper are indicated by solid
circles as are the multipenetration stations of PLEIADES 3 along 1°N. The

Table 2. Heat Flow Station Data From KNORR 73 Leg 4

Station Number	Latitude	Longitude	Depth[1]	Bottom Water Temp	K[2]	Q[3]	s.d.	W[4]	s.d.	Pen.[5]	# Obs.	Tilt[6]	Environmental[7] Evaluation Factor
4	1 51.0'	-110 16.1'	3732	1.398	2.018	1.08	0.11	0.9	0.5	978	7	-	-
5-1	3 44.3'	-113 31.6'	3837	1.436	(2.04)	2.81	0.13	0.7	0.1	779	6	-	A
5-2	3 44.8'	-113 32.1'	3854	1.441	(2.04)	2.76	0.09	0.6	0.1	774	7	-	A
5-3	3 45.3'	-113 32.6'	3844	1.442	(2.04)	2.40	0.04			792	7	-	A
6-1	4 01.8'	-115 20.0'	4008	1.452	(2.04)	1.82	0.19	2.5	0.7	762	7	4	B
6-2	4 01.7'	-115 19.6'	4012	1.454	(2.04)	1.52	0.16	1.3	0.6	784	7	8	B
6-3	4 01.6'	-115 19.0'	4036	1.455	(2.04)	1.80	0.10	2.4	0.3	756	7	14	B
7-1	4 00.7'	-115 01.7'	4034	1.469	(2.04)	1.65	0.10	1.4	0.3	774	7	5	B
7-2	4 01.2'	-115 01.1'	4084	1.475	(2.04)	1.14	0.20	13.6	2.7	739	7	8	B
7-3	4 01.6'	-115 00.5'	4044	1.472	(2.04)	1.01	0.09	4.6	0.7	768	6	10	B
7-4	4.01.9'	-115 00.0'	4054	1.471	(2.04)	0.76	0.09	3.5	0.7	826	6	4	B
8-1	4 04.0'	-114 40.9'	3976	1.459	(2.04)	2.02	0.24	5.5	1.0	630	6	4	B
8-2	4 04.1'	-114 40.3'	3979	1.464	(2.04)	1.93	0.11	5.6	0.5	631	5	10	B
8-3	4 04.2'	-114 39.7'	4002	1.466	(2.04)	2.17	0.21	10.0	1.2	624	6	9	B
9-1	3 59.3'	-114 16.8'	3934	1.459	(2.04)	1.22	0.21	4.1	1.1	729	7	8	B
9-2	3 59.5'	-114 16.2'	3880	1.458	(2.04)	1.10	0.21	2.8	1.2	766	7	12	B
9-3	3 59.9'	-114 15.4'	3892	1.454	(2.04)	1.06	0.11	2.5	0.6	818	7	3	B
10	4 00.0'	-114 00.8'	3869	1.430	2.021	2.66	0.11	0.6	0.2	992	7	6	B
11-1	3 58.0'	-114 11.6'	3861	1.455	(2.04)	1.54	0.17	1.2	0.5	820	6	6	B
11-2	3 57.8'	-114 10.9'	3886	1.459	(2.04)	1.76	0.42	2.2	1.3	901	7	4	B
11-3	3 57.4'	-114 09.0'	3882	1.456	(2.04)	1.85	0.17	2.3	0.7	829	6	4	B
12-1	3 57.7'	-114 09.1'	3894	1.445	(2.04)	2.96	0.31	3.6	0.8	553	7	10	B
12-2	3 57.7'	-114 09.1'	3894	1.439	(2.04)	1.40	0.26	1.1	0.9	662	7	8	B
12-3	3 56.6'	-114 07.2'	3911	1.444	(2.04)	1.65	0.17	1.6	0.6	595	6	7	B
12-4	3 56.2'	-114 04.7'	3320	1.428	(2.04)	3.11	0.20	2.7	0.4	601	7	8	B
12-5	3 55.7'	-114 03.3'	3827	1.429	(2.04)	3.07	0.33	1.0	0.6	614	7	7	B
12-6	3 55.3'	-114 02.4'	3835	1.430	(2.04)	4.42	0.88	2.7	1.3	538	7	20	B
13-1	4 00.6'	-114 09.5'	3903	1.449	(2.04)	1.72	0.36	4.3	1.6	571	6	13	B
13-2	4 01.0'	-114 08.9'	3962	1.452	(2.04)	1.65	0.14	4.9	0.7	601	6	3	B
13-4	4 00.9'	-114 08.3'	3958	1.452	(2.04)	2.28	0.23	7.6	1.0	508	6	9	B
13-5	4 00.7'	-114 07.4'	3865	1.449	(2.04)	2.02	0.36	2.5	2.5	352	5	25	B
13-6	4 00.7'	-114 07.4'	3903	1.449	(2.04)	2.76	0.77	3.8	3.1	431	5	28	B

			[1]	[2]		[3]		[4]		[5]		[6]	[7]
13-7	4 00.5'	-114 06 4'	3869	1.441	(2.04)	3.01	0.44	3.0	1.1	552	5	15	B
13-8	4 00.7'	-114 05.3'	3890	1.445	(2.04)	2.60	0.42			332	3	25	B
13-9	4 00.9'	-114 05.6'	3905	1.446	(2.04)	2.99	0.17	2.1	0.5	440	4	27	B
13-10	4 01.1'	-114 04.2'	3900	1.445	(2.04)	3.98	0.68	3.5	1.3	570	4	7	B
14	4 00.7'	-114 10.1'	3934	1.441	2.052	1.21	0.15	0.8	0.5	1094	7	4	B
15	1 45.0'	-118 22.5'	4166	1.530	1.982	1.75	0.06	2.4	0.2	864	6	12	A
16	1 03.1'	-123 52.9'	4686	1.504	1.709	1.06	0.21	1.5	0.9	1009	7	8	A
17-1	1 02.1'	-126 33.8'	4469	1.479	(1.95)	1.10	0.12	0.3	0.4	1066	7	8	A
18-1	0 59.8'	-128 24.3'	4405	1.474	(2.19)	1.31	0.02			887	7	17	A
18-2	0 59.9'	-128 23.4'	4397	1.477	(2.19)	1.50	0.12	0.3	0.4	897	7	12	A
18-3	1 00.0'	-128 22.8'	4394	1.476	(2.19)	1.55	0.09	0.3	0.2	890	7	8	A
19-1	0 54.9'	-128 41.4'	4415	1.476	(2.19)	1.21	0.02			943	7	16	A
19-2	0 54.6'	-128 40.0'	4380	1.472	(2.19)	1.34	0.02			901	7	11	A
19-3	0 54.7'	-128 39.7'	4427	1.478	(2.19)	1.22	0.01			901	7	12	A
20	-1 24.3'	-131 28.4'	4498	1.510	1.988	1.61	0.31	12.6	3.4	800	6	10	B
21-1	-1 29.0'	-131 29.8'	4405	1.458	(2.16)	1.04	0.15	3.1	1.0	704	6	15	B
21-2	-1 29.4'	-131 28.8'	4341	1.452	(2.16)	0.88	0.19	2.2	1.4	777	7	27	B
21-3	-1 29.7'	-131 27.5'	4520	1.473	(2.16)	0.62	0.19	2.3	2.2	653	6	29	B
21-4	-1 29.7'	-131 27.1'	4522	1.466	(2.16)	0.47	0.26	0.3	2.7	810	7	33	B
21-5	-1 29.4'	-131 26.0'	4520	1.466	(2.16)	0.77	0.29	1.4	2.0	716	6	26	B
21-6	-1 29.1'	-131 25.3'	4510	1.463	(2.16)	0.91	0.37	1.8	2.7	647	6	33	B
21-7	-1 29.1'	-131 25.3'	4510	1.475	(2.16)	0.81	0.24	2.1	2.0	663	5	30	B
21-8	-1 28.6'	-131 24.6'	4434	1.463	(2.16)	0.45	0.06			644	5	33	B
22-1	-1 28.6'	-131 23.8'	4409	1.452	(2.16)	0.77	0.23	2.6	1.7	888	7	11	B
22-2	-1 28.7'	-131 23.0'	4384	1.447	(2.16)	0.95	0.23	2.8	1.4	883	7	15	B
22-3	-1 28.6'	-131 22.1'	4370	1.448	(2.16)	1.00	0.16	2.2	0.9	920	6	12	B
23	-0 51.8'	-134 03.0'	4444	1.463	2.155	0.43	0.30	0.6	3.3	1027	7	4	B
24	1 16.2'	-137 15.7'	4318	1.431	2.113	0.65	0.25	3.0	2.3	1015	6	11	B
25-1	1 16.0'	-137 16.7'	4312	1.440	(2.11)	0.65	0.02			940	7	14	B
25-2	1 15.8'	-137 16.4'	4320	1.433	(2.11)	0.62	0.17	2.9	1.7	716	5	31	B
25-3	1 15.6'	-137 16.1'	4322	1.429	(2.11)	0.28	0.01			977	6	26	B
26	4 30.8'	-140 19.5'	4425	1.398	(2.08)	1.88	0.18	0.4	0.2	1138	6	10	A
27	9 00.0'	-143 48.2'	5065	1.440	(1.61)	1.49	0.66	5.1	3.2	734	5	-	B

1 Water depth in corrected meters.
2 Harmonic mean thermal conductivity cal cm^{-1} $^{o}C^{-1}$ sec^{-1} x 10^{-3}. Parentheses indicate values assumed from nearby stations.
3 Heat flux cal cm^{-2} sec^{-1} x 10^{-6}.
4 Volume flux cm sec^{-1} x 10^{-6} (porosity x fluid velocity). Blank values indicate stations where no significant curvature was observed (W   1.0 x 10^{-7} cm/sec).
5 Depth to which lowermost thermistor penetrated in cm.
6 Tilt in degrees from vertical.
7 Environmental evaluation factor is from Sclater et al. (1976).

Table 3. Heat Flow Station Data From PLEIADES Leg 3

Station Number	Latitude	Longitude	Depth[1]	Bottom Water Temp.	K[2]	Q[3]	s.d.	W[4]	s.d.	Pen.[5]	# Obs.	Tilt[6]	Environmental Evaluation Factor[7]
2	1 02.7'	-105 34.3'	3526	1.54	1.961	3.48	1.76	7.5	4.9	695.	4	0	B
6	1 02.7'	-113 52.9'	3956	1.46	2.171	3.58	0.19	0.9	0.3	1013.	5	0	-
10	0 58.0'	-126 36.9'	4492	1.50	1.949	1.99	0.88	2.6	2.2	1106.	5	0	A
11-1	0 59 0'	-127 33.1'	4592	1.50	(1.95)	0.60				250.	3	0	B
11-2	0 58.9'	-127 33.2'	4461	1.50	(1.95)	0.80				250.	3	0	B
11-3	0 58.6'	-127 33.3'	4451	1.50	(1.95)	2.09				250.	3	0	B
12	0 57.3'	-128 24.9'	4374	1.47	· 2.194	1.42	0.13	0.9	0.5	851.	4	0	A
14	0 57.3'	-131 32.8'	4451	1.48	2.131	1.81	0.54	5.9	2.0	1191.	5	0	B
15-1	1 01.6'	-133 28.9'	4476	1.46	(2.07)	0.34				250.	2	0	B
15-2	1 01.0'	-133 28.9'	4470	1.46	(2.07)	0.39				250.	2	0	B
15-3	1 00.9'	-133 28.2'	4467	1.46	(2.07)	0.43				250.	2	0	B
15-4	1 00.7'	-133 27.6'	4468	1.46	(2.07)	0.45				250.	2	0	B
16	0 58.4'	-135 05.3'	4298	1.45	2.255	2.27	0.19	0.8	0.3	1197.	5	0	A
17-1	3 58.9'	-136 00.5'	4484	1.41	(2.08)	1.90				250.	3	0	B
17-2	3 58.6'	-136 00.4'	4498	1.41	(2.08)	1.85				250.	3	0	B
18	3 56.5'	-135 59.2'	4527	1.48	(2.08)	1.79	0.04			1260.	4	0	B
19-1	4 02.8'	-136 01.7'	4470	1.40	(2.08)	1.81				150.	2	15	B
19-2	4 02.0'	-136 03.3'	4472	1.41	(2.08)	1.86				150.	2	15	B
19-3	4 01.5'	-136 03.7'	4472	1.41	(2.08)	1.96				150.	2	0	B
20	4 01.5'	-135 56 9'	4449	1.40	(2.08)	1.31	0.07			1013.	3	0	B
21-1	3 56.7'	-135 57.1'	4544	1.41	(2.08)	1.99				250.	3	0	B
21-2	3 56.2'	-135 57.4'	4527	1.41	(2.08)	1.85				250.	3	0	B
21-3	3 55.6'	-135 57.7'	4517	1.41	(2.08)	1.83				250.	3	0	B
21-4	3 54.8'	-136 00.0'	4503	1.41	(2.08)	1.90				250.	3	0	B
21-5	3 54.2'	-136 00.0'	4472	1.41	(2.08)	1.94				250.	3	15	B
21-6	3 53.9'	-136 00.4'	4465	1.40	(2.08)	1.84				250.	3	15	B
21-7	3 53.8'	-136 02.0'	4473	1.40	(2.08)	1.94				250.	3	0	B
22-1	4 03.8'	-135 57.3'	4455	1.40	(2.08)	0.93				250.	3	15	B
22-2	4 02.3'	-135 57.9'	4463	1.40	(2.08)	1.18				250.	3	15	B
22-3	4 01.3'	-135 57.6'	4432	1.40	(2.08)	1.56				250.	3	30	B
22-4	4 01.0'	-135 57.7'	4432	1.40	(2.08)	1.88				250.	3	30	B
22-5	4 00.7'	-135 58.0'	4476	1.40	(2.08)	2.15				250.	3	30	B
22-6	4 00.5'	-135 58.5'	4472	1.39	(2.08)	1.78				250.	3	30	B

[1] Water depth in corrected meters.
[2] Harmonic mean thermal conductivity cal cm^{-1} $°C^{-1}$ sec^{-1} x 10^{-3}. Parentheses indicate values assumed from nearby stations.
[3] Heat flux cal cm^{-2} sec^{-1} x 10^{-6}.
[4] Volume flux cm sec^{-1} x 10^{-6} (porosity x fluid velocity). Blank values indicate stations where no significant curvature was observed (W 1.0 x 10^{-7} cm/sec).
[5] Depth to which lowermost thermistor penetrated in cm.
[6] Tilt in degrees from vertical. 0 indicates tilt between 0 and 15 degrees, 15 indicates tilt between 15 and 30 degrees and 30 indicates a tilt greater than 30 degrees.
[7] Environmental evaluation factor is from Sclater et al. (1976).

majority of the stations designated by the solid circles penetrated to only a

few meters and consist of only 2 or 3 individual temperature measurements.

Deeply penetrating measurements collected during KNORR 73-4 and PLEIADES 3 are

marked with solid squares. Small open squares along $4^{o}N$ at $115^{o}W$ show the

location of a series of multipenetration stations that are part of an

investigation of the eastern boundary of the low zone. The large open squares

($4^{o}N$, $136^{o}W$; 1° 30'S, 131° 30'W; $4^{o}N$, $114^{o}W$) are the approximate

areal coverage of the three detailed heat flow and CSP surveys.

The relationship of this data to basement roughness and sediment cover

is analysed on three scales: (1) a broadly based study of the widely spaced

heat flow coverage and the geological environment evaluated from the existing

CSP coverage, (2) a study of individual heat flow measurements obtained along

individual CSP tracks, and (3) a detailed study of closely spaced heat flow

measurements within a grid of CSP tracks.

Geological and Tectonic Setting:

Upwelling of nutrient rich water associated with the equatorial current

system causes the equatorial Pacific Ocean to be one of the most biologically

productive ocean regions. The equatorial sedimentation pattern is dominated

by the remains of siliceous and calcareous organisms. At the equator

sediments are highly calcareous grading to dominantly siliceous to the north .

and south and at greater distances into clays. An approximate northern

boundary between the calcareous and siliceous rich sediments is the Clipperton

Fracture Zone while north of the Clarion Fracture Zone the siliceous sediments

grade into red clays (Horn et al., 1973). An excellent summary of the

sedimentation patterns and distributions within the equatorial Pacific is found in Van Andel et al., (1975).

The geology and tectonics of the equatorial Pacific are summarized in Figure 10. The data presented in this figure is based on 30 CSP tracks, shown as thin lines, dashed where data is non-existent or poor in quality. Outcropping basement features ranging from small hills to seamounts (greater than 0.5 seconds reflection time above local mean acoustic basement depth) are indicated with solid circles. Near outcrops (less than 0.2 seconds reflection time sediment cover), outcropping basement highs (greater than 25 km in horizontal scale) and small localized outcrops (less than 0.5 seconds reflection time above mean basement depth) are marked with inverted v's. It must be pointed out that the sediment isopacns in Figure 10 represent sediment thickness averaged over a horizontal scale of hundreds of km and that the variability of sediment thickness and the nature of basement outcrops occuring on a smaller scale is difficult to generalize. The presence of scarps in Figure 10 is indicated by lines perpendicular to the ship's track. DSDP sites are marked with solid squares.

Sediment thickness was determined from the CSP data. In Figure 10 transparent sediments overlying acoustic basement are contoured in intervals of 0.1 seconds reflection time. Assuming a average seismic velocity of 2.0 km/sec for the sediment layer (Ewing et al., 1968), the isopachs can be thought of as 100 meter contours. Ewing et al. (1968) observed two forms of acoustic basement, basaltic basement and an opaque sedimentary layer known as Horizon B. Horizon B is distinguished from basaltic basement primarily by its characteristically smooth upper surface. Where it is present, deeper reflectors are not observed with any consistency. DSDP sampling has shown this

Figure 10. Map of sediment thickness and basement outcrops within the
Equatorial Pacific Ocean inferred from continuous seismic profiling data
(CSP). Sediment isopachs of 0.1 sec two way travel-time are shown by bold
solid lines. Light lines indicate the ship tracks of the CSP data base.
Dashed lines represent poor or no data. The tracks corresponding to cruises
VEMA 24-3, SCAN 10, KNORR 73-4 and PLEIADES 3 are marked with a stippled
line. CSP records collected alomg these four tracks are shown in Figures 11
through 15. Outcropping localized basement features ranging from small hills
to seamounts (greater than 0.5 seconds reflection time above mean basement
depth) are indicated with solid circles. Near outcrops (less than 0.2 sec.
reflection time sediment cover), small outcrops (less than 0.5 seconds
reflection time above the mean basement depth) and outcropping basement highs
(greater than 25 km in horizontal scale) are indicated by inverted v's (see
text). Scarps are shown by solid lines perpendicular to the ship track.
Isochrons from Sclater et al. (1980) are marked with thick dashed lines.
Crust younger than 2 m.y. is shaded.
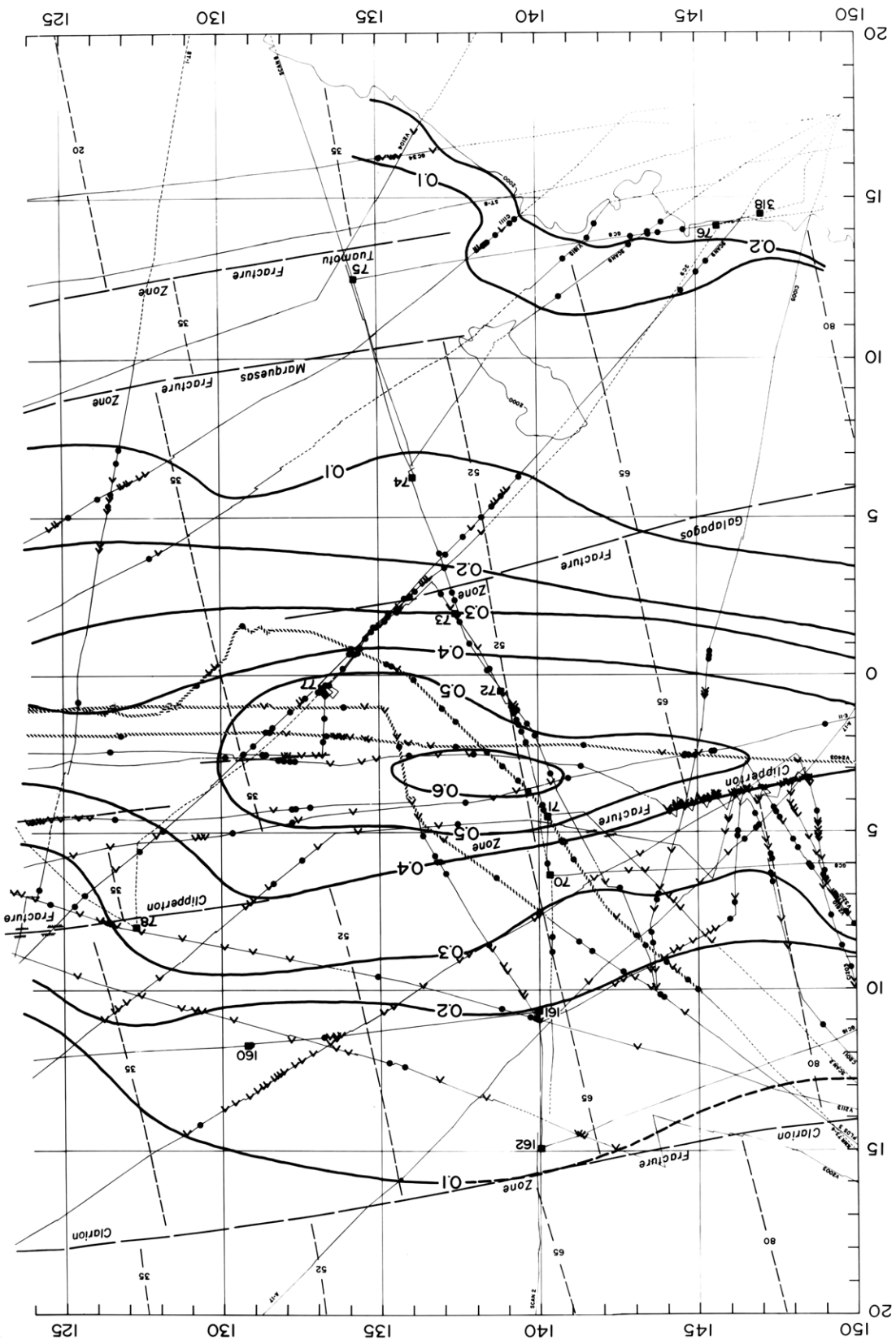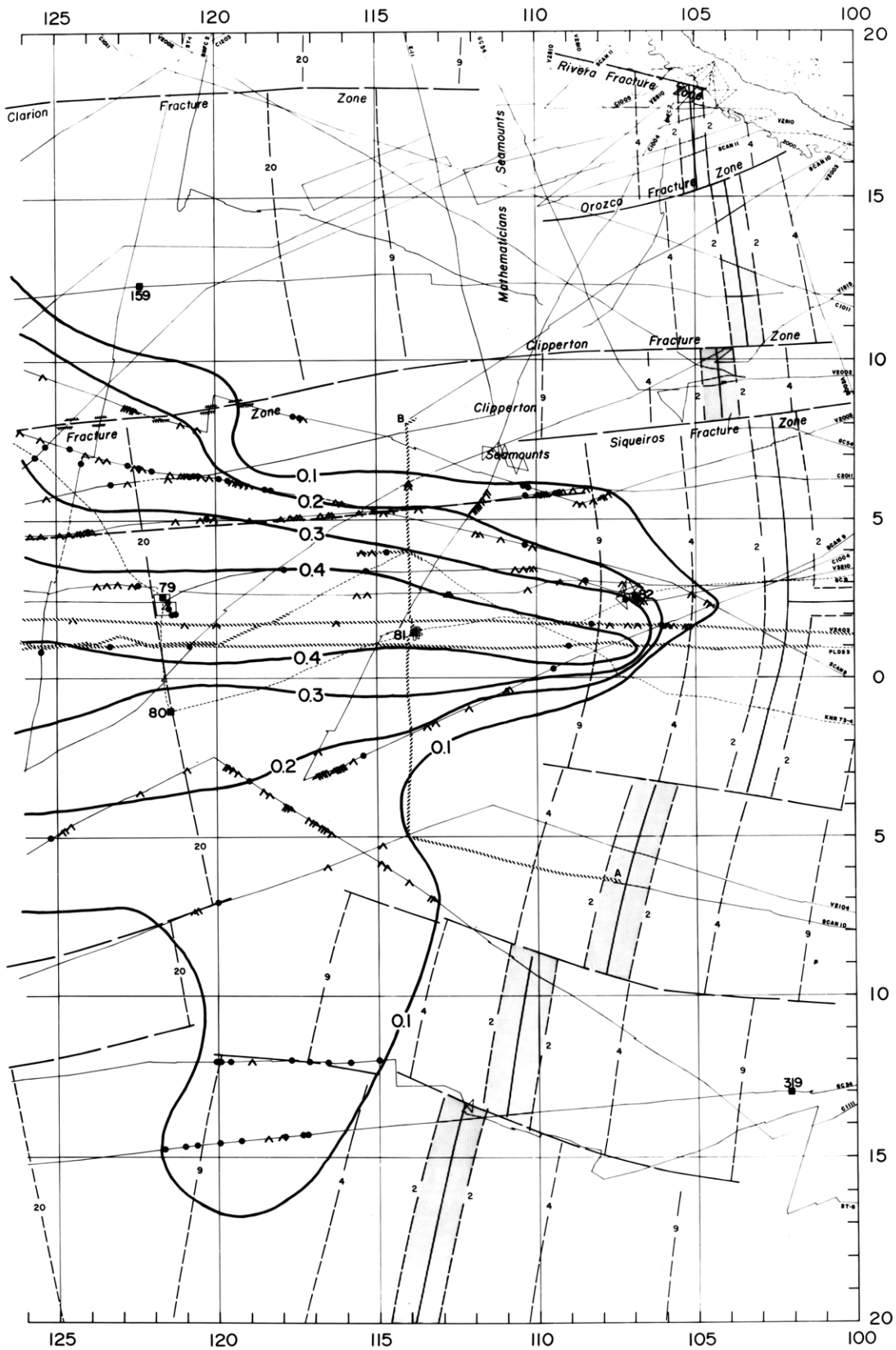
opaque layer to consist of numerous chert beds of Eocene and Paleocene age
(Tracey et al., 1971). In Figure 10, Horizon B is present roughly within the
0.2 second isopach.

The patterns of sea-floor spreading are quite complicated in the
equatorial Pacific. Throughout the Cenozoic, the East Pacific Rise has not
remained fixed. Shifts in its position in the form of ridge jumps have left
distinct features such as the Mathematician and Clipperton seamounts (Sclater
et al., 1971).

In Figure 10 the isochrons of Sclater et al. (1980) are superimposed on
the major tectonic features of the equatorial Pacific. Many of these features
can be clearly recognized in the existing CSP coverage, although some less
constrained features are not so evident. A fossil ridge at 115°W between
the equator and 7°N was suggested by Herron (1972) based on magnetic anomaly
patterns. Analysis of the CSP records transecting this area does not support
the presence of this feature nor suggest the existence in this vicinity of
another feature that could be interpreted as a continuous fossil ridge.
Another feature not supported by bathymetric and CSP data is a fracture zone
predicted by Sclater et al. (1971) based on topographic profiles between the
Clarion and Clipperton Fracture Zones. However, the distribution of DSDP
basement ages between these two fracture zones supports the existence of this
fracture zone (Van Andel et al., 1975).

From the bathymetric data, the Galapagos Fracture Zone ceases to be a
distinct feature east of 130°W where it begins to be inundated by the
equatorial sediment bulge. Our attempts to trace this fracture zone through
the sediment budge using the CSP data have been unsuccessful. A possible

explanation is that the Galapagos Fracture Zone is not continuous east of 125° to 130°W but instead consists of several en-echelon fracture zones. Winterer (1976) suggested that in this general area many small ridge jumps may have occurred rather than one large jump that would have left a prominent topographic feature. The basement of the region north of the alleged cessation of the Galapagos Fracture Zone is unusually rough (Figure 10). Sclater et al. (1971) suggested the existence of a fracture zone north of 5°N between 110° and 130°W essentially an extension of the Siqueiros Fracture Zone. The basement throughout this area is also unusually rough. We have indicated the position of this fracture zone with a bold dashed line and show another small fracture zone at 4°N between 125-130°W. Adopting the suggestion of Winterer (1976) we propose that a major reorientation of the spreading axis during the Oligocene in the equatorial Pacific resulted in the termination of the Galapagos Fracture Zone in the vicinity of 130°W. The evolution of a complicated pattern of en-echelon fracture zones and numerous short ridge jumps is a possible consequence of such a change in spreading direction and could explain the observed extreme basement roughness.

Interpretation of Heat Flow Measurements Along CSP Tracks:

The relationship between observed heat flow and geological environment was studied along four CSP tracks, SCAN 10, VEMA 24-3, PLEIADES 3 and KNORR 73-4, transecting the equatorial sediment bulge (Figures 11 through 15). Two of these tracks (SCAN 10 and VEMA 24-3) were discussed by Sclater et al. (1976). The geological environment was classified according to the scheme of Sclater et al. (1976) in which a letter was assigned to each of four

Figure 11. Line drawing of the CSP records collected during SCAN 10 annotated with the heat flow measurements of Sclater et al. (1971). Ship's track is shown in Figure 10 and the portion corresponding to the line drawing is marked A-B. The stations with the heat flow values of 2.72, 2.80, 1.16, 2.42, 2.58 and 2.31 were located in A environments (Sclater et al., 1976).
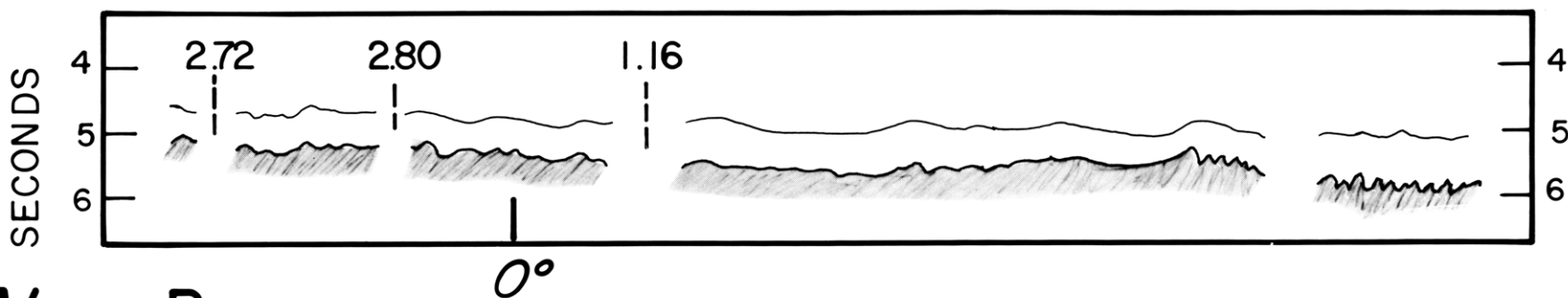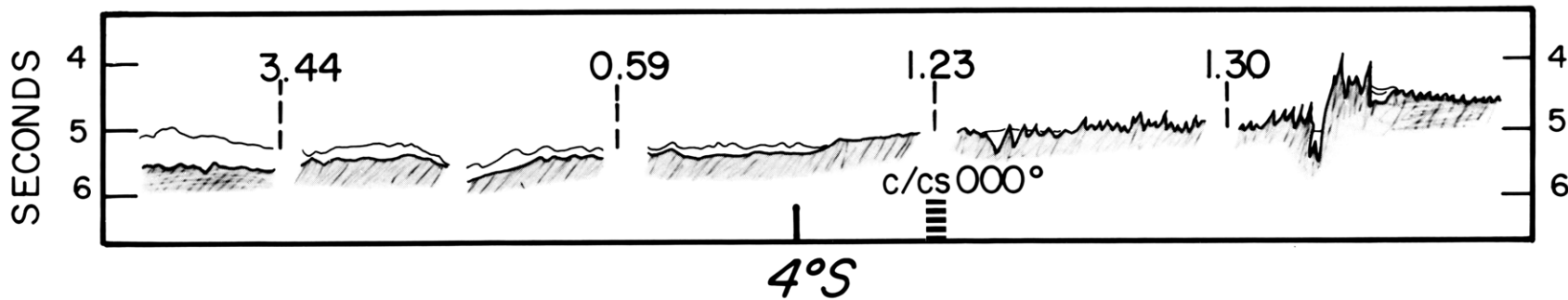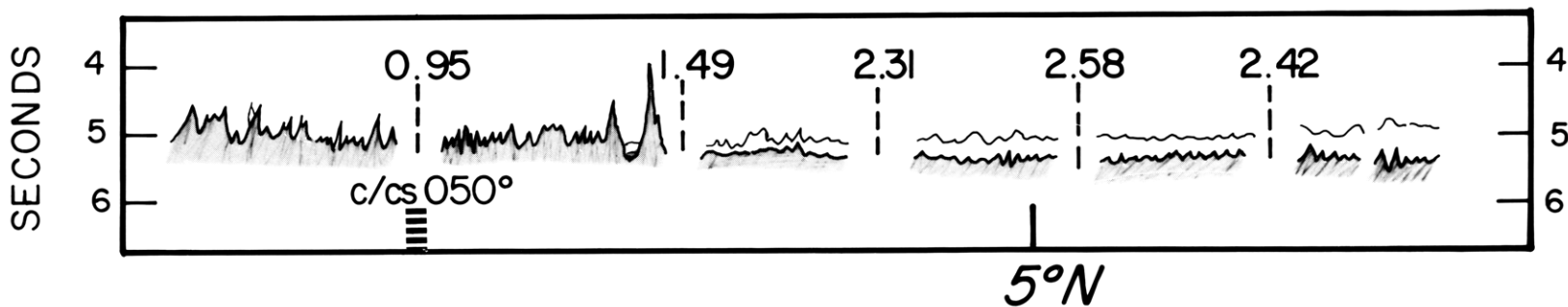
Figure 12. CSP records collected during VEMA 24-3, (a) between 100° and 125°W, (b) between 125° and 150°W, annotated with the heat flow measurements reported by Langseth et al. (1971) and the geologic environment (Sclater et al., 1976). Ship's track is shown in Figure 10.

Figure 13. CSP records collected during PLEIADES 3, (a) 101° to 122°W, (b) 122° to 133°W and (c) 133° to 140°W, annotated with the results of the heat flow measurements and the geological environment (Sclater et al., 1976). Volume flux values are in parenthesis. Ship's track is shown in Figure 10.

2 - WAY TRAVEL TIME (sec)

6 —
7 —
8 —
140°W

SURVEY

5 —
6 —
7 —
5°N
c/c 312°

5 —
6 —
7 —

HF 16
2.27
(0.8)

HF 15
0.34 0.39
0.43 0.45

5 —
6 —
7 —
135°W
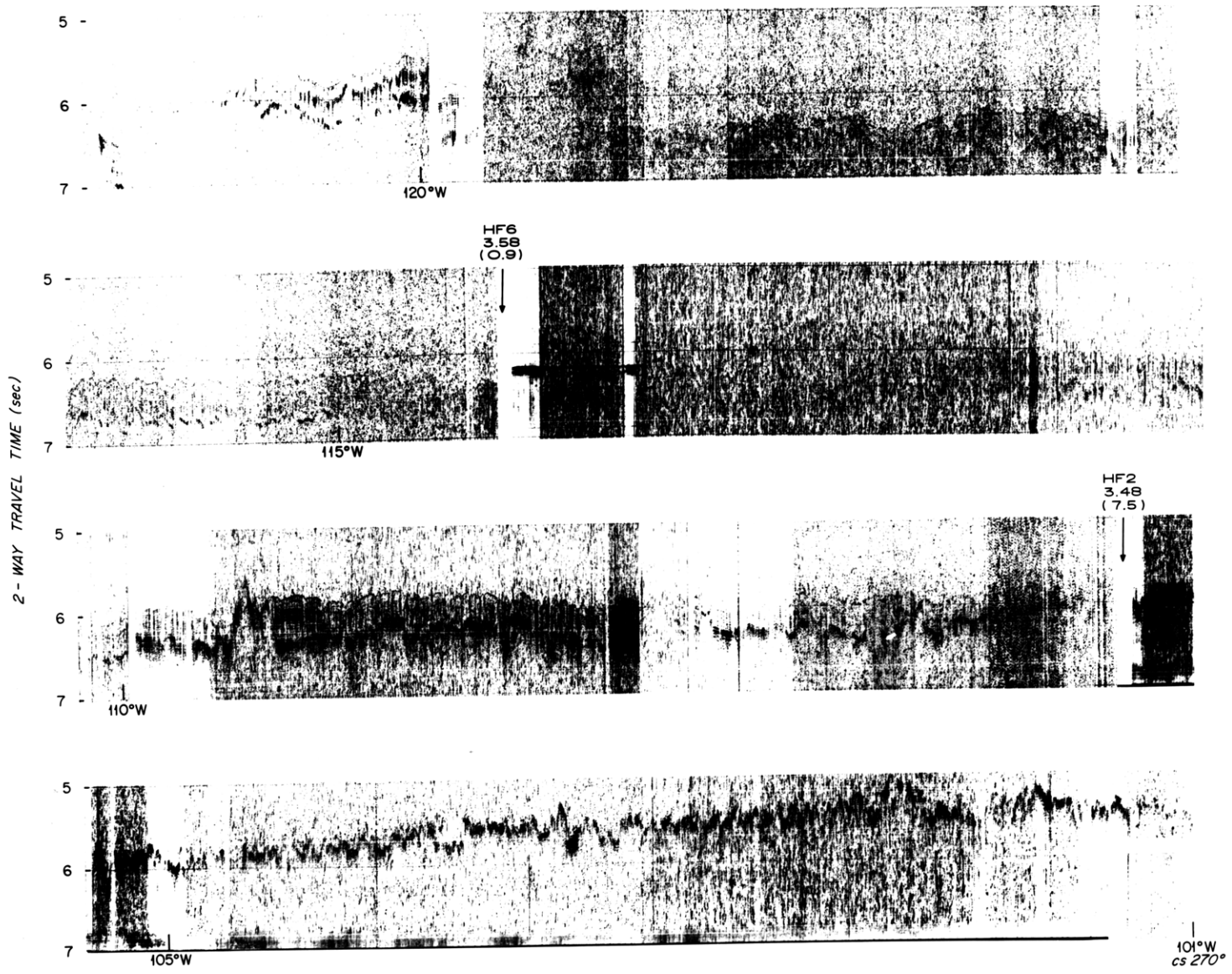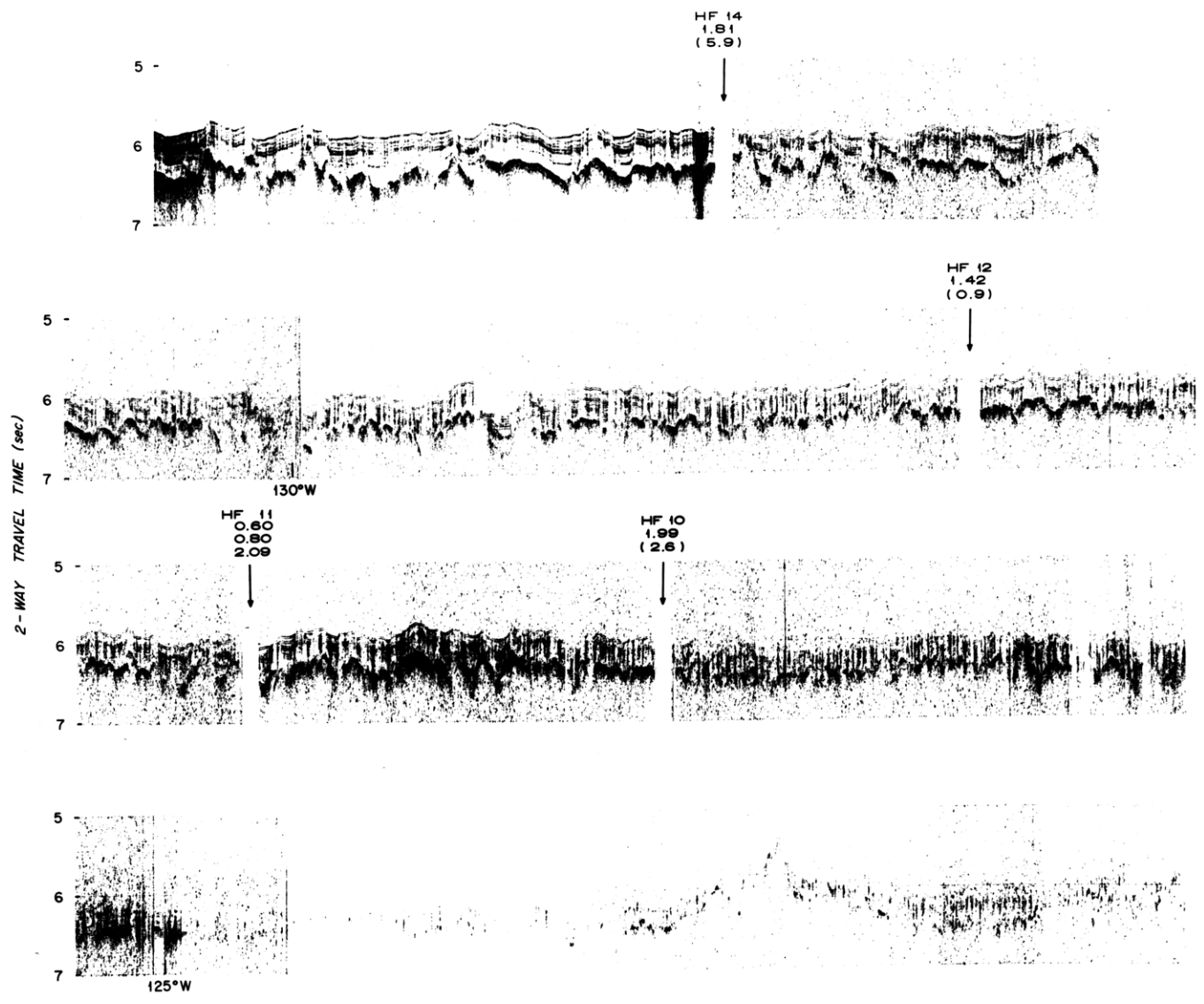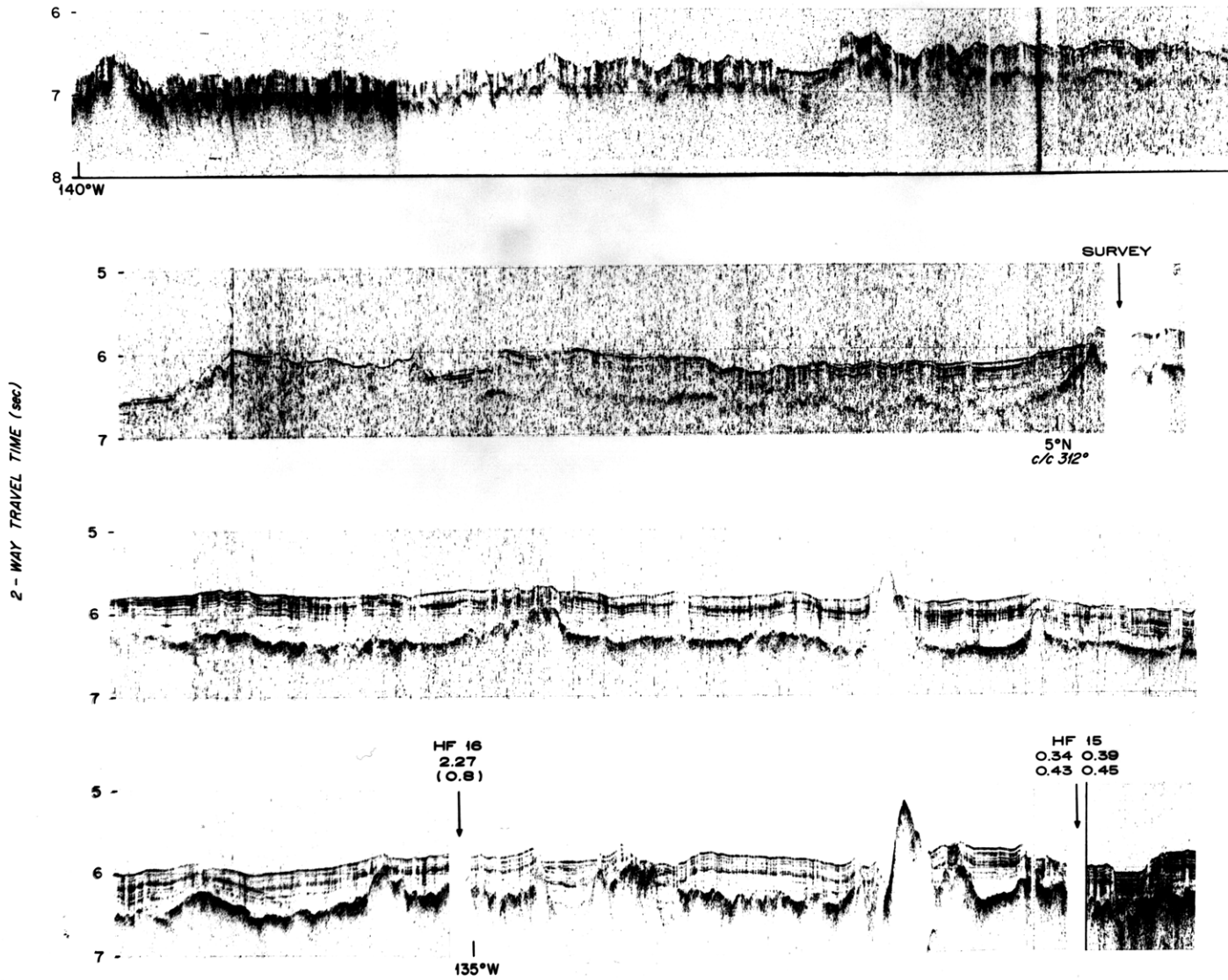
Figure 14. Continuous seismic profiling (CSP) records collected during KNORR 73-4, (a) from 117° 45' to 129^OW, (b) from 129° to 138^OW and (c) 138° to 145^OW, annotated with the results of the heat flow measurements and the geologic environment (Sclater et al., 1976). Volume flux values are in parenthesis. Ship's track is shown in Figure 10.

HF 15
1.75
(2.4)
A

6 –

7 –

8 – |
117°45'W
cs. 245°

120°W

c/c 265°

HF 16
1.06
(1.5)
A

6 –

7 –

8 –

2 – WAY TRAVEL TIME (sec)

HF 17
1.10
(0.3)
A

6 –

7 –

8 –
125°W

HF 18
1.31 1.50 1.55
(—) (0.3) (0.3)
A

HF 19
1.21 1.34 1.22
(—) (—) (—)
A

6 –

7 –

8 –
c/c 236°

2 - WAY TRAVEL TIME (sec)

5 — 130°W

SURVEY
c/c 270°
c/c 295°

HF 23
0.43
(0.6)
B
135°W

HF 24   HF 25
0.65 0.65 0.62 0.28
(3.0)(—)(2.9)(—)
B

c/c 315°

HF 26
1.88
(0.4)
A

CLIPPERTON
F.Z.

2 - WAY TRAVEL TIME (sec)

140°W

HF 27
1.49
(5.1)
B

10°N
145°W
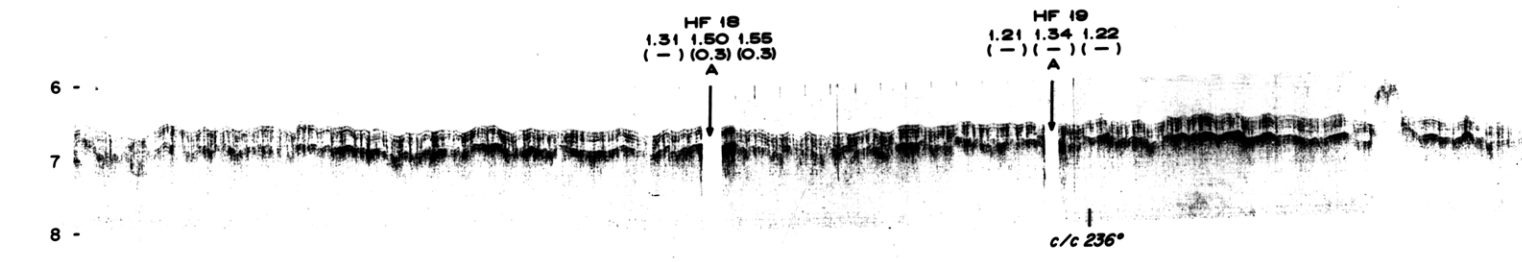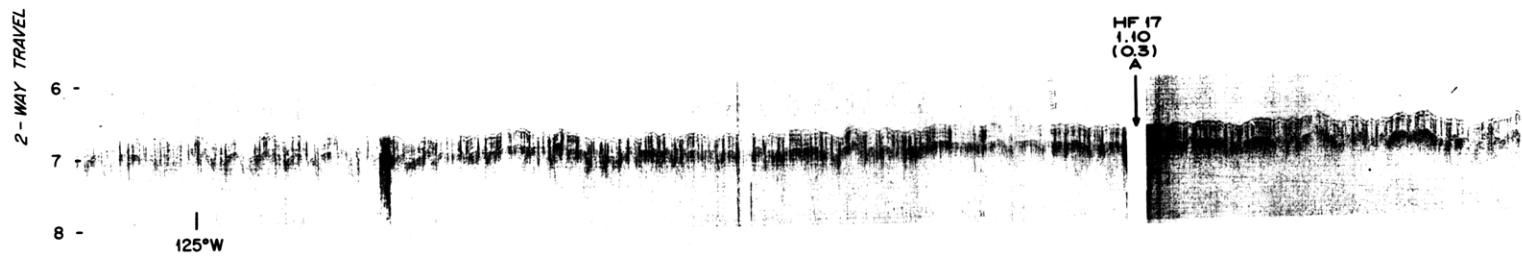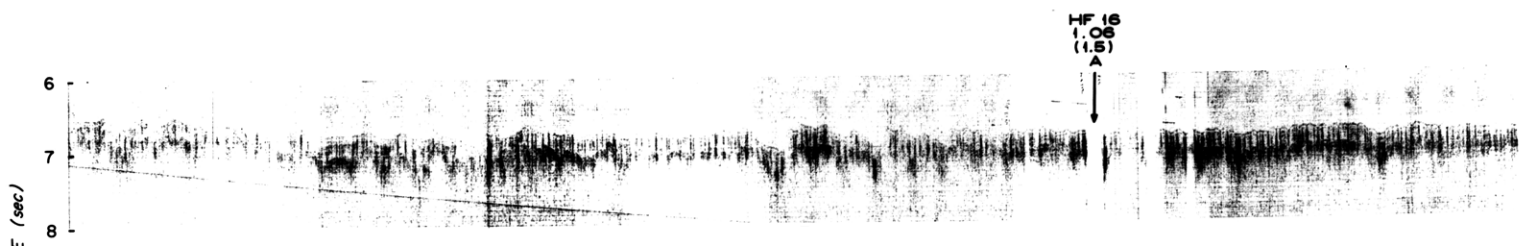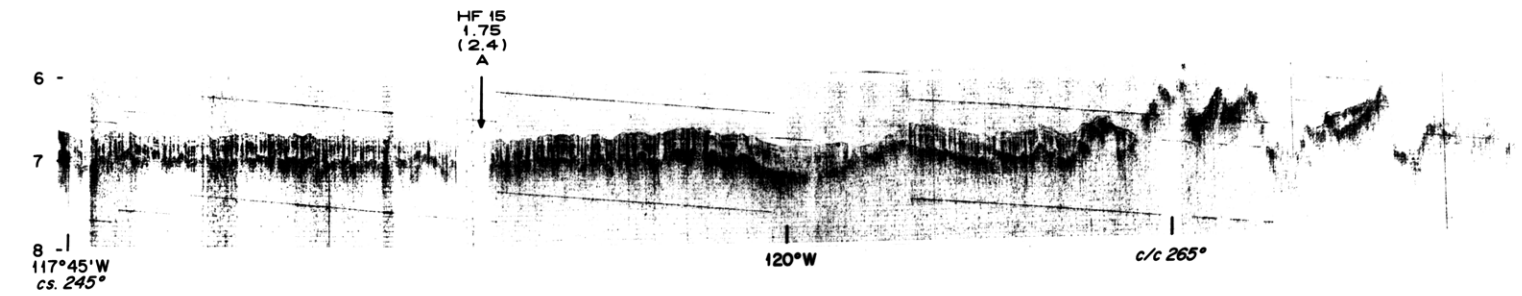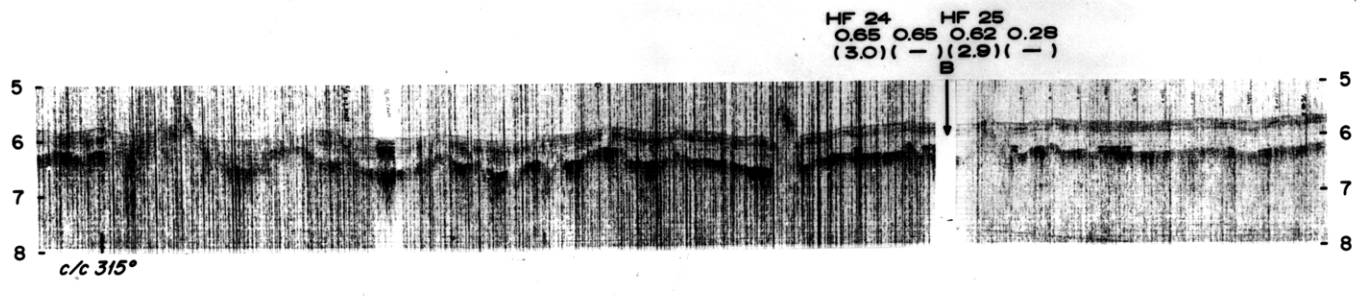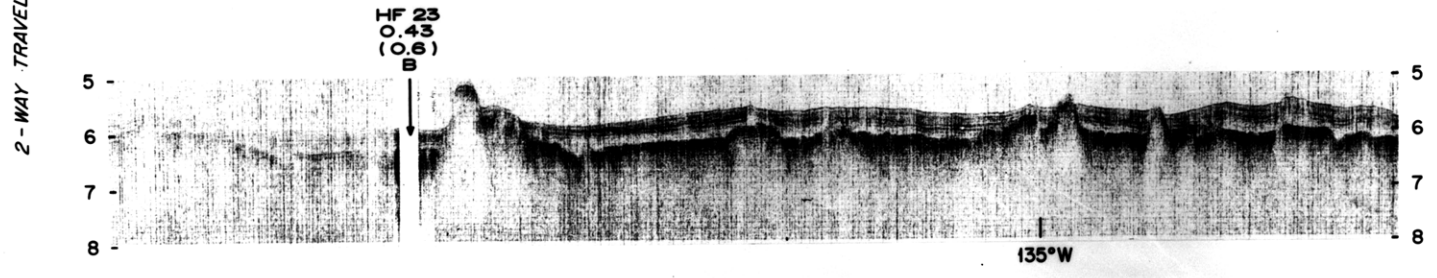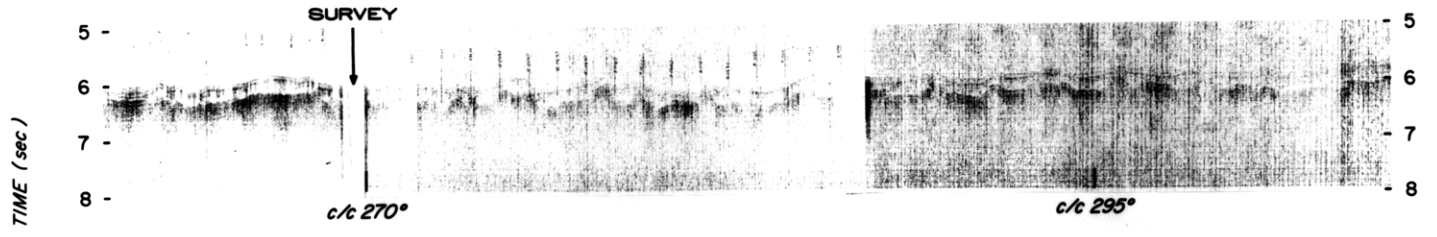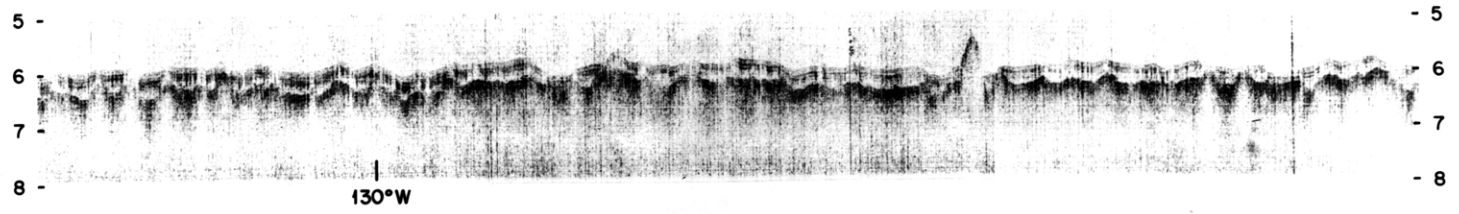
Figure 15. KNORR 73-4 CSP records collected along the east-west profile A-A'
across the boundary of the low heat flow zone annotated with the results of
stations 5 through 9. The boundary is located within the detailed survey area
(see Figure 17).

A

STATION 5

EAST

2.87(0.7)
2.76(0.6)
2.40

2.42

DETAILED SURVEY

STATION 9

1.06 (2.5)
1.10 (2.8)
1.22 (4.1)

SECONDS

5.0 — 5.0
5.5 — 5.5
6.0 — 6.0

c/c 297°   0300   10 km   c/c
c/s 8.0 kts   270°   0600   0900

STATION 8

2.17(10.1)
1.93(5.7)
2.02(5.5)

STATION 7

0.76(3.5)
1.01 (4.6)
1.14 (13.6)
1.65 (1.4)

STATION 6

1.80 (2.4)
1.52 (1.2)
1.82 (2.5)

A'

WEST

SECONDS

5.0 — 5.0
5.5 — 5.5
6.0 — 6.0

1200   1500
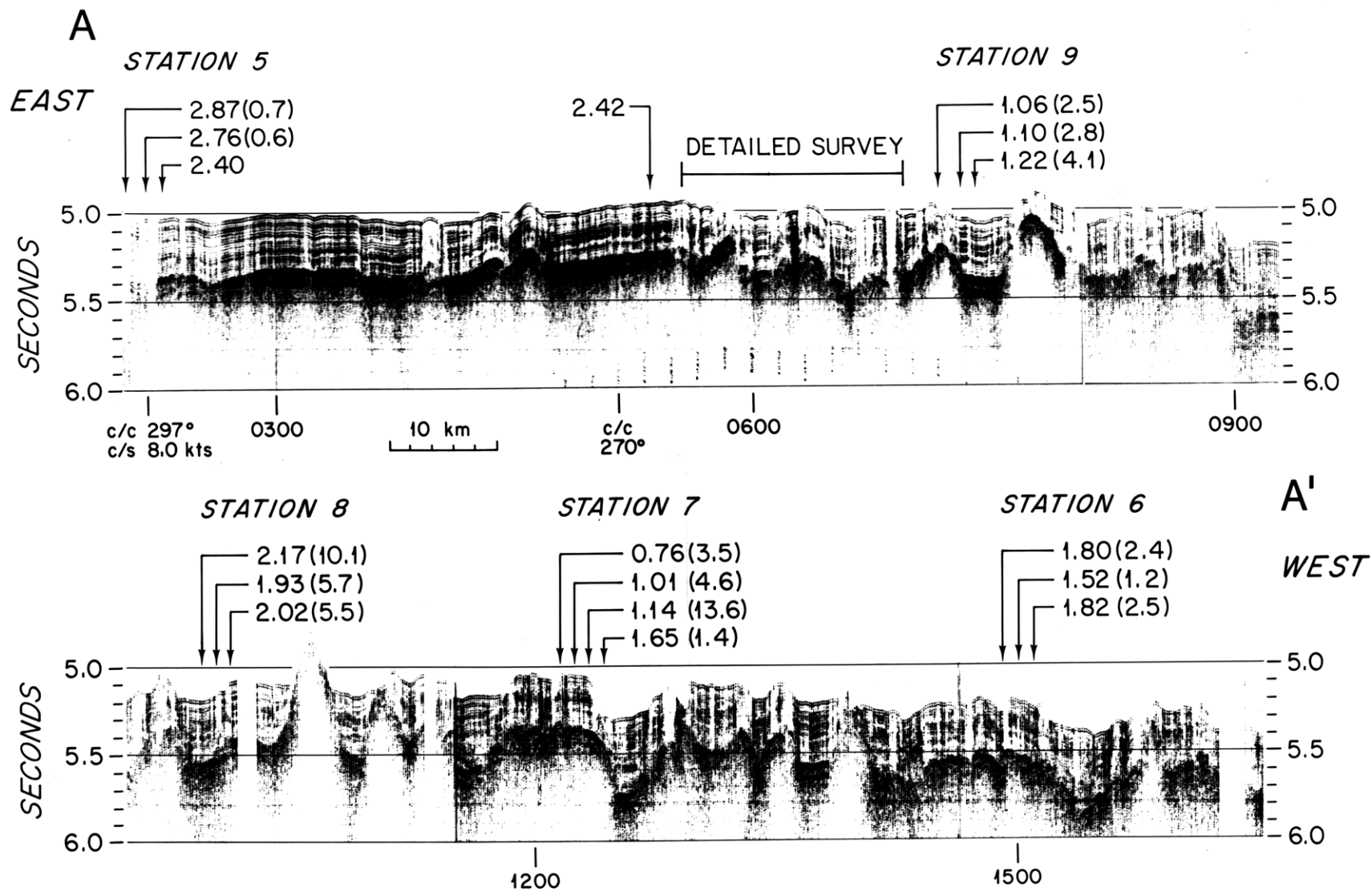
Figure 16. Classification scheme of geological environments evaluated from CSP data (Sclater et al., 1976).
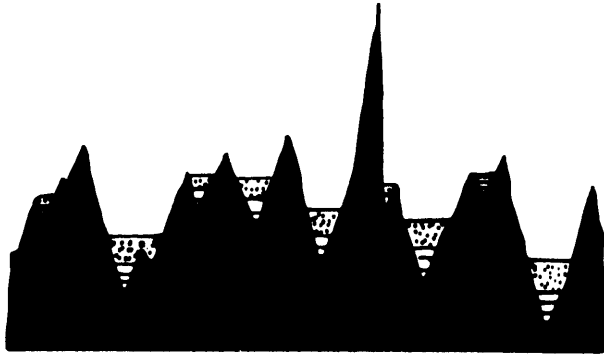
D
CREST
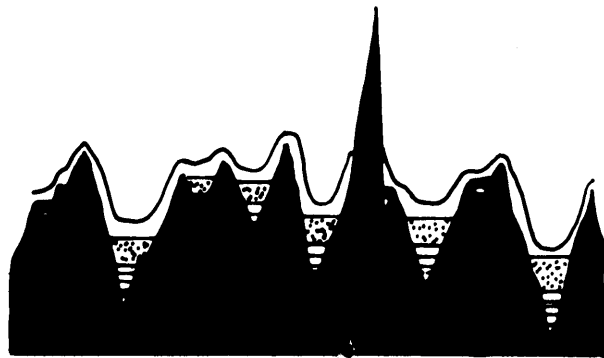
C
FLANK
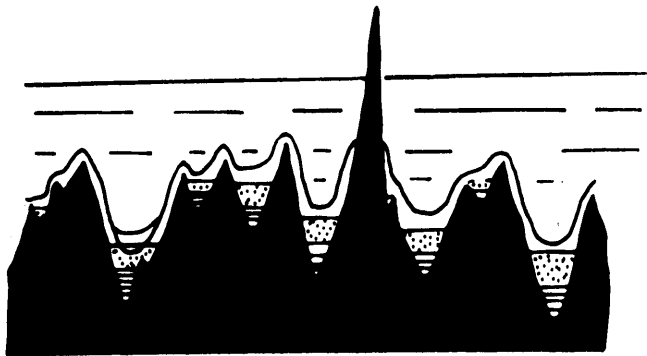
B
BASIN
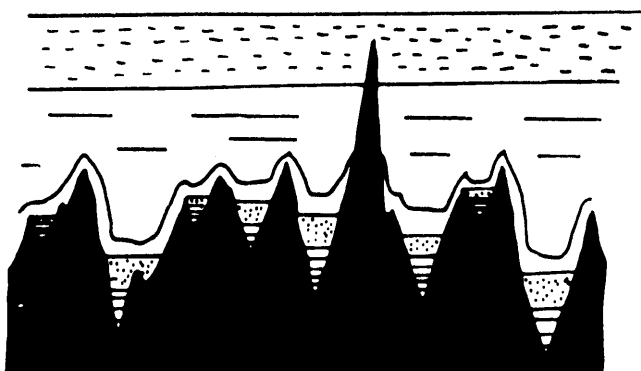
A
BASIN

subdivisions shown in Figure 16. The classifications are: A, flat or rolling hills with greater than 150-200 meters of continuous sediment cover within 18 km of the station; B, flat or rolling hills with generally greater than 20 meters of continuous sediment cover where outcropping basement highs or very thin sediment cover is observed; C, a site in an area of rolling hills or rough topography with a thin or variable sediment cover; and D, a site in a sediment pond between or next to an obvious outcropping basement high.

The CSP records in Figures 11 through 15 are annotated with the station identification, the heat flow results and an evaluation of the geological environment. There is a clear relationship between heat flow and geological environment illustrated in these figures. As the thickness of the sediment increases, uniform heat flow is found. Where the sediment cover is less than 200 meters and basement can be seen to outcrop, the values are generally low and variable.

Figure 11 is a line drawing of a section of CSP records from Scripps cruise SCAN 10 transecting the sediment bulge from south to north at 114°W. These records are shown with a dashed line marked A-B in Figure 10. Apart from the 1.16 HFU value in the middle of the bulge, five values (2.72, 2.80, 2.42, 2.51, 2.31 HFU) show remarkably little scatter and a clear correlation of A environments and the 200 meter isopach. The average heat flow of these A stations and crustal age (15-20 m.y.) is plotted in Figure 3.

The east-west profile of L-DGO cruise VEMA 24-3 is shown in Figures 12 a and b. The stations assigned an A environment along this track were the basis for the average heat flow value for the equatorial Pacific plotted in Figure 3 (average crustal age of 55 m.y.). Stations 27-31 ranged in environment from B

to D. Station 32, located near the intersection of the VEMA 24-3 and SCAN 10 tracks, has an A environment of heat flow value 2.77, similar to the average value of the SCAN 10 data. With the exceptions of stations 38 and 45, all of the heat flow measurements west of 115° are less than 1.20 HFU. Some of these stations clearly cannot be classified as A (stations 34, 37, 39, 40 and 43). From the two-dimensional reconaissance of the CSP track, stations 35 (0.81 HFU), 38 (1.45 HFU), 41 (0.50 HFU), 42 (0.51 HFU), 44 (0.89 HFU) and 45 (1.55 HFU) appear to be A environments. We cannot determine the cause for the discrepancy with the sediment blanket model presented by this data without additional three dimensional CSP coverage.

The CSP data from PLEIADES 3 is shown in Figures 13 a, b and c. Temperature gradients and thermal conductivity profiles for the deeply penetrating stations from PLEIADES 3 and KNORR 73-4 are plotted in Figure 2. Between 101° and 120°W the records are poor in quality, making it difficult to assign an environment to stations 2 and 6. Station 2 was assigned a B environment and station 6 was not assigned an environment. At both of these stations the heat flow was high, 3.48 and 3.58 HFU respectively. The temperature gradient at station 2 was very non-linear (W = 7.5 x 10^{-6} cm/sec). West of 120°W, environments could be evaluated, however, only three stations were assigned an A environment, 10, 12 and 16. The values of W calculated for stations 12 and 16 were relatively small (0.9 and 0.8 x 10^{-6} cm/sec respectively) and although a large value of W was calculated for station 10 (2.6 x 10^{-6} cm/sec), it is poorly resolved as the magnitude of its standard deviation (2.2 x 10^{-6} cm/sec) is large. Stations 11, 14 and 15 were located in B environment. At station 14 a high heat flow

of 1.81 HFU and a W of 5.9 ± 2.0 x 10^{-6} cm/sec were observed. At stations 11 and 15 several short probe measurements (2.5 meter penetration) sampled low heat flow, less than 1 HFU, with the exception of one high value of 2.09.

The CSP records from KNORR 73-4 west of $117^{\circ}45'W$ are shown in Figure 14. Stations 15 through 19 were all assigned A environments. At each of these stations a heat flow greater than 1 HFU was observed. Two of these stations were slightly non-linear (stations 15 and 16). At station 26, also an A environment, a heat flow of 1.88 HFU and a volume flux of 0.4 x 10^{-6} cm/sec were measured. Stations 23, 24, 25 and 27 were assigned B environments. At stations 23, 24 and 25, low heat flow and high volume fluxes with large standard deviations were observed.

A short east-west CSP line was run during KNORR 73-4 to investigate an apparent transition between low and "normal" heat flow observed in the vicinity of $4^{\circ}N$ and $115^{\circ}W$. The CSP records from this line are shown in Figure 15. The track of this profile marked A-A' is shown in Figure 17 along with the existing coverage of heat flow measurements. The profiles of temperature versus depth are plotted in Figure 18. This area is one of the few sectors of the equatorial Pacific heat flow low where the data coverage is dense enough to confidently define its boundary. To the east along $114^{\circ}W$ are heat flow measurements from SCAN 10 that are compatible with the theoretical heat flow for the appropriate age crust. A few degrees to the west, Von Herzen an Uyeda (1963) observed several measurements which are low and scattered.

Several pogo heat flow stations were deployed eastward, retracing the CSP profile. In Figure 15, the projection of these measurements onto the CSP line is shown, however, these positions are approximate as the actual

Figure 17. Map of the well-defined eastern boundary of the low heat flow

zone. Included are the locations of the ship's track of the CSP line crossing

this boundary, the locations of multi-penetration stations along the CSP

profile, the detailed survey at 4°N, 114°W and all other heat flow data in

the vicinity.
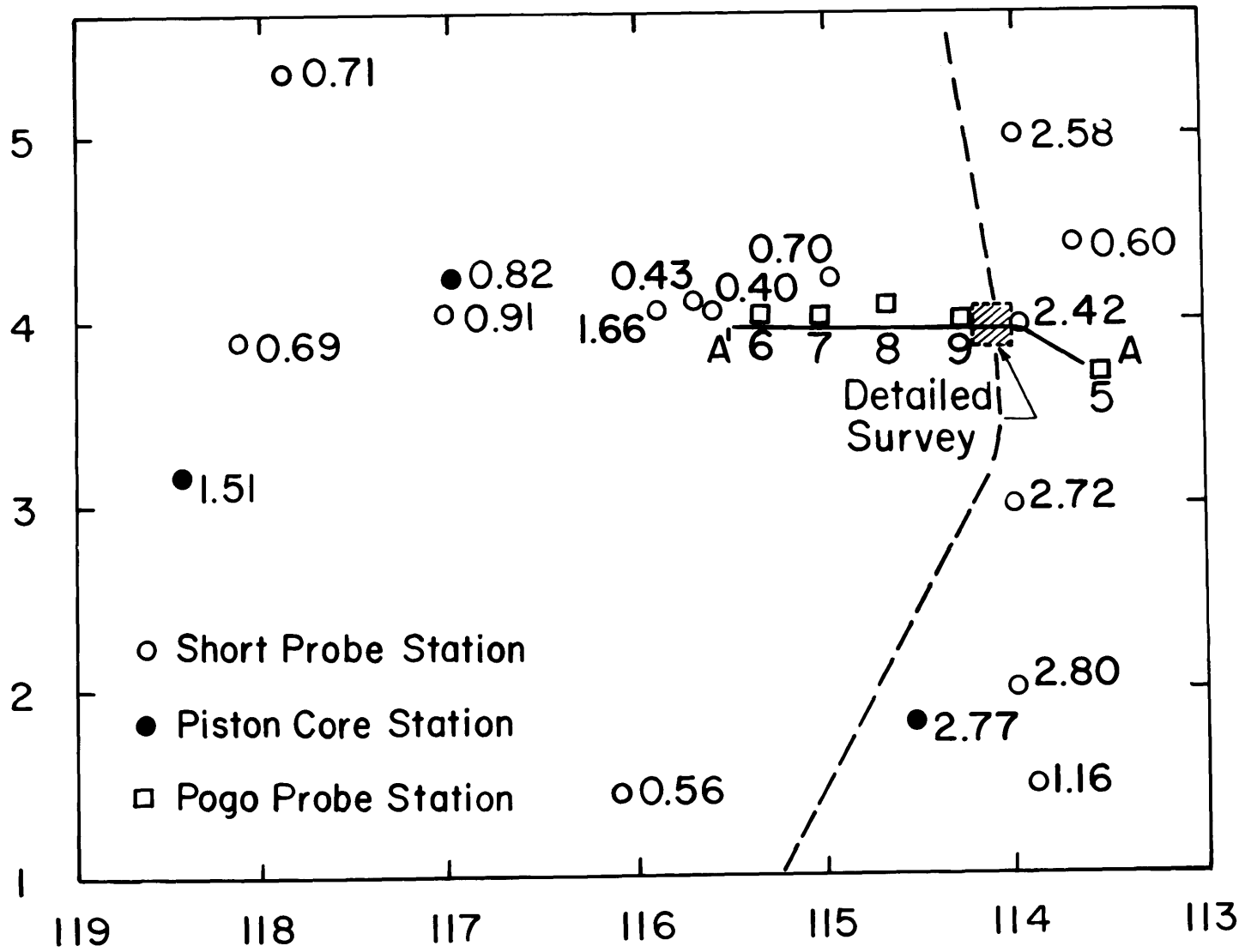
Figure 18. Temperature versus depth data corresponding to the stations located along profile A-A'. Each profile is identified by station number along with the value of heat flow and volume flux. The horizontal scale divisions are 0.1°C. Errors bars assigned to the temperature data are shown. The lines drawn through the temperature data represent the best fit of a simple conductive/convective thermal model (see text).

There is no text material missing here.
Pages have been incorrectly numbered.

stations were located less than a degree to the north of the profile (Figure 17). In Figure 15 the CSP line is annotated with the results of these measurements, (volume flux in parentheses). The bathymetry observed during the heat flow measurements closely followed the CSP bathymetry suggesting that the features observed in the CSP records are roughly lineated north-south. Throughout the profile the basement is draped by over 0.2 sec. of sediment except where outcropping basement occurs. It is most likely that in the area of rough basement (to the west), the sediment cover is pierced by numerous outcrops, in addition to those visible in the CSP records.

The basement topography along this line changes from smooth (statiom 5) to rough (station 9) towards the west as the geological environment changes from A to B. The corresponding heat flow observations change from "normal" values with nearly zero flow rates for A environments (at station 5, W ranged from 0 to < $7x10^{-7}$ cm/sec) to variable heat flux with W ranging from 1.2 to $13.6x10^{-6}$ cm/sec for B environments (stations 6 through 9).

Detailed Survey Studies:

Detailed studies of the relationship between heat flow and geological environment were conducted at three sites (Figure 1). These surveys consisted of closely spaced heat flow measurements within a grid of CSP tracks. Contoured maps of both bathymetry and sediment thickness were obtained. The surveys were located as follows: survey 1 (PLEIADES 3) was outside the low heat flow zone at $4^{o}N$, $136^{o}W$; survey 2 (KNORR 73-4) was inside the low zone, just north of the Galapagos Fracture Zone at $1^{o}30'S$, $131^{o}30'W$; and survey 3 (KNORR 73-4) was at a transition between the low heat flow zone

and the "normal" heat flow values previously discussed in Figures 15, 17 and 18 at 4°N, 114°W.

The contoured bathymetry and sediment thickness maps for survey 1 are shown in Figures 19 and 20. Sediment thickness for this region is greater than 0.4 seconds reflection time, with the exception of a northwest-southeast trending trough, around which the sediment cover thins to less than 0.2 seconds reflection time. This trough is bounded to the north by a 75 meter scarp which represents a step-jump in the bathymetry from 4500 meters in the southwest to 4425 meters in the northeast. It is difficult to determine from the CSP records whether the basement outcrops along the scarp. However, it appears that the thinnest sediments occur just southwest of the scarp in the deepest section of the trough. Twenty heat flow measurements were made in the survey area. The heat flow station identifications are plotted in Figure 19 and the results of the heat flow measurements are included in Figure 20. Two measurements were deeply penetrating (squares in Figures 19 and 20), both of which defined linear temperature gradients (stations P18 and P20 in Figure 3). The other eighteen measurements were taken using a short probe, penetrating 2.5 meters (circles in Figures 19 and 20). Since the survey and the heat flow measurements were navigated by satellite, errors in position up to 1 km are possible. The sixteen heat flow measurements located at and southwest of the trough are remarkably uniform (average value of 1.89 ± 0.09 HFU and crustal age of approximately 55 m.y.). To the northeast, four measurements of lower heat flow were observed (0.93, 1.18, 1.31 and 1.56 HFU). The temperature gradient measured down to 10 meters at one of these sites, station 20 (1.31 HFU), did not show any sign of non-linearity.

Figure 19. Bathymetry in corrected meters contoured at 25 meter intervals and locations of heat flow measurements in the PLEIADES 3 detailed heat flow survey centered at 4°N, 136°W. Pogo and piston core stations are marked by circles and squares respectively. The location of the ship's track during the CSP and bathymetric survey is shown by light dashed lines.

Figure 20. Sediment thickness in seconds of two way travel time contoured at
0.2 second intervals and heat flow values in heat flow units in the PLEIADES 3
detailed heat flow survey centered at 4^oN, 136^oW. Pogo and piston core
stations are marked by circles and squares respectively. The location of the
ship's track during the CSP and bathymetric survey is shown by light dashed
lines.
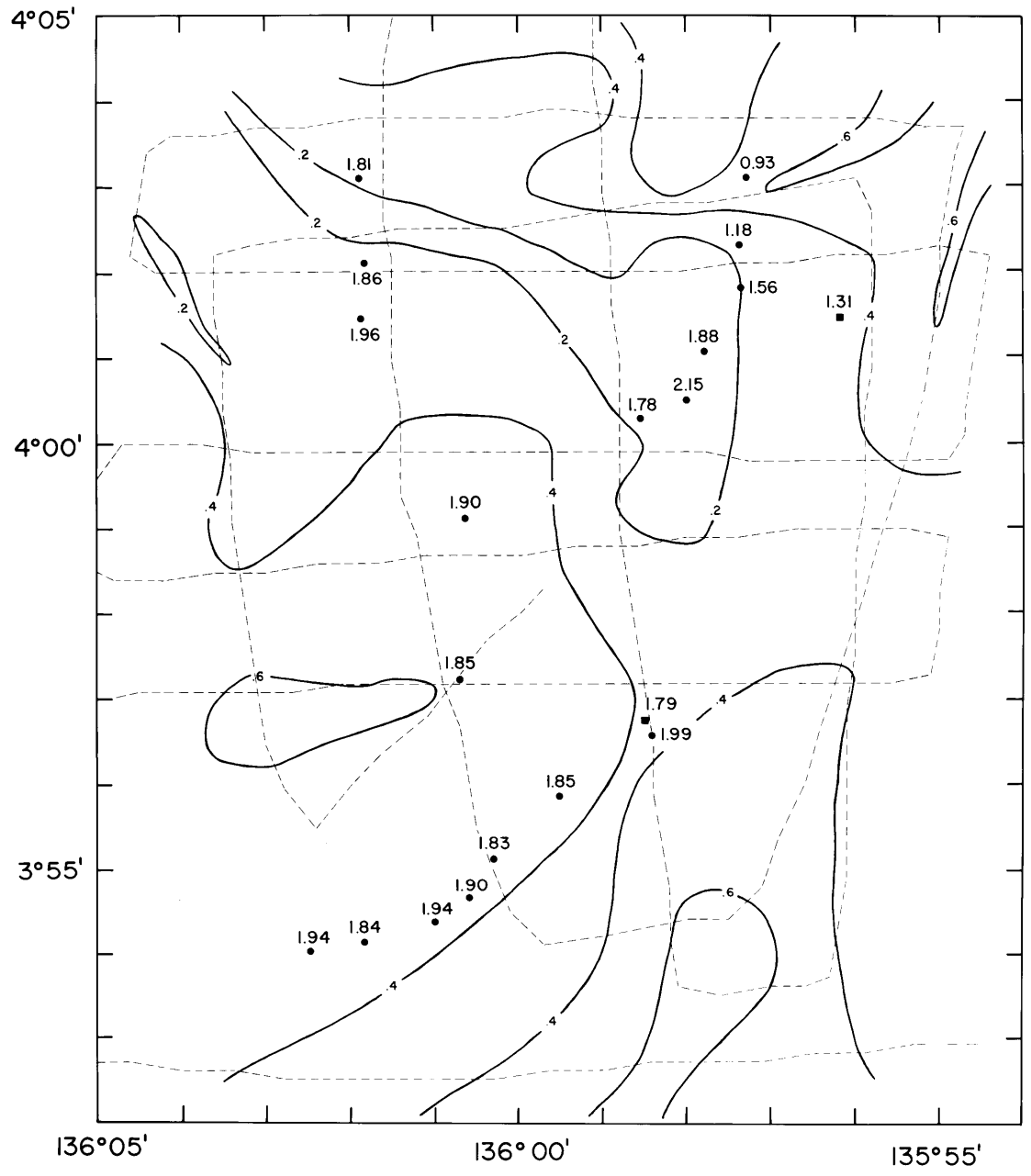
Analysis of the refraction of heat due to the contrast in thermal conductivity between basement and sediment using the technique of Sclater and Miller (1969) could not explain the observed low heat flow to the northeast of the scarp. Due to their proximity to local topographical highs, it is possible that these four low measurements have resulted from recent sediment slumping or creep. The average value for all the measurements within survey 1 is 1.76 ± 0.30 HFU.

The second survey was conducted around a radar reflector buoy centered at $1^\circ25'$S and $131^\circ27'$W. Figures 21 and 22 are contoured maps of the bathymetry and sediment thickness. There is a north-south lineation in the bathymetry most noticeable in a wide valley at 4500 meters depth passing through its center. At the southern end of this valley, this depression is 7 km wide, broadening northward to over 15 km. The topography reaches its shallowest point in the northeastern part of the survey where it reaches 4350 meters. The sediment thickness is variable ranging from 0.05 to 0.4 seconds reflection time.

Twelve heat flow measurements were made within survey two. The locations of these stations are shown in Figure 21 and the results are included in Figure 22. With the exception of one piston core station (station 20), all heat flow measurements fall along an east-west profile marked D-D' in Figures 21 and 22. This line transects the valley at the southern part of the survey. Figure 23 is a drawing of the vertical cross section of this transect. Included in this drawing are plots of the results of the heat flow data reduction, showing the calculated values for Q and W with standard deviations. The heat flow values range between 0.3 and 1.0 HFU with standard deviations of up to 50%. The best fit volume fluxes are high, generally

Figure 21. Bathymetry in corrected meters contoured at 25 meter intervals and locations of heat flow measurements in the KNORR 73-4 detailed heat flow survey centered at $1°30'S$, $131°30'W$. Multi-penetration and piston core stations are marked by circles and squares respectively. The location of the ship's track during the CSP and bathymetric survey is shown by light dashed lines.
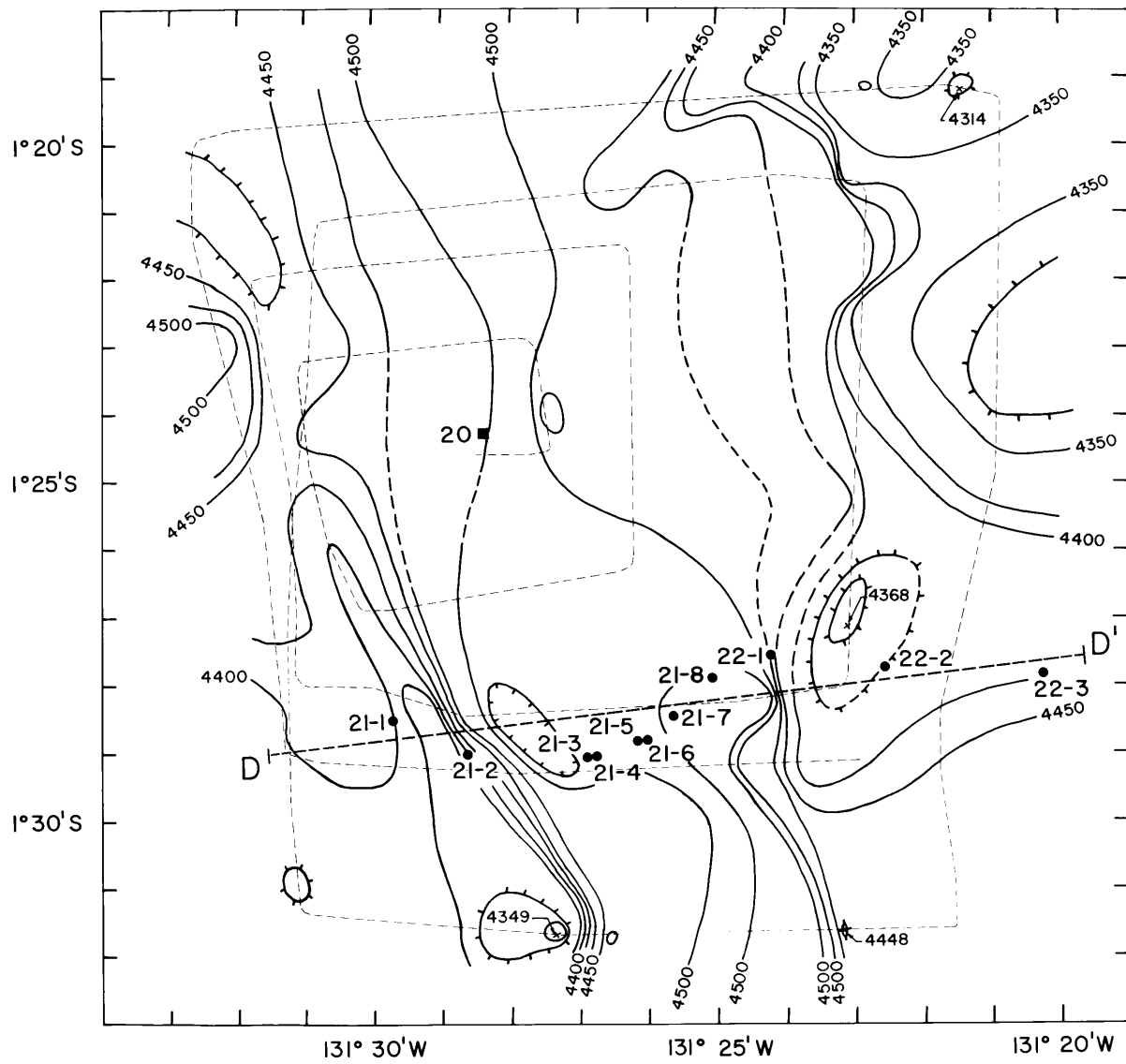
Figure 22.   Sediment thickness in seconds of two way travel time contoured in 0.05 sec intervals and heat flow values in heat flow units in the KNORR 73-4 detailed heat flow survey centered at $1^\circ 30'S$, $131^\circ 30'W$.   Multi-penetration and piston core stations are marked by circles and squares respectively.   The location of the ship's track during the CSP and bathymetric survey is shown by light dashed lines.
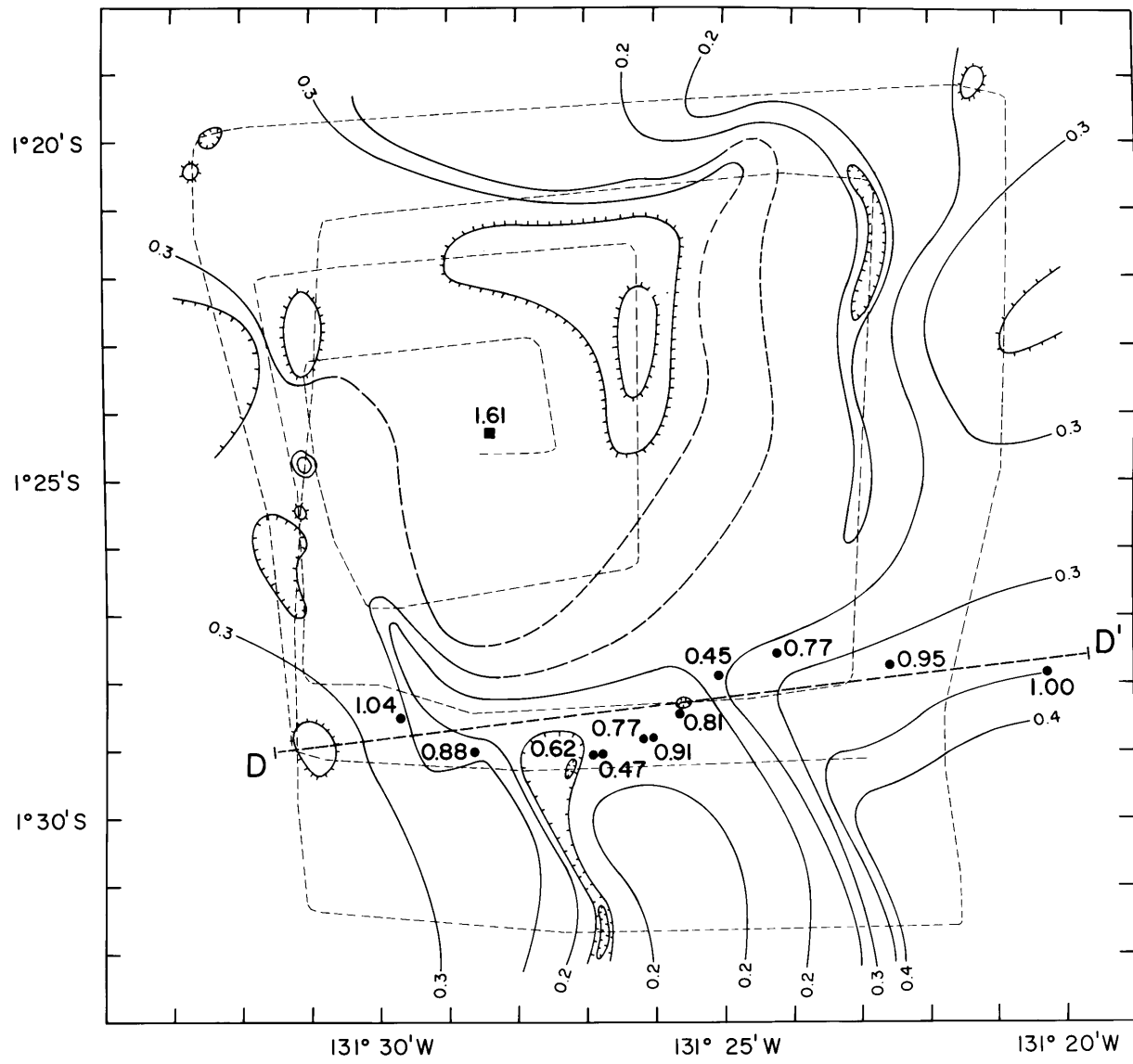
Figure 23. Schematic diagram of basement and sediment thickness along profile D-D'. Also plotted are the best fit values and standard deviations of both heat flow and volume flux.
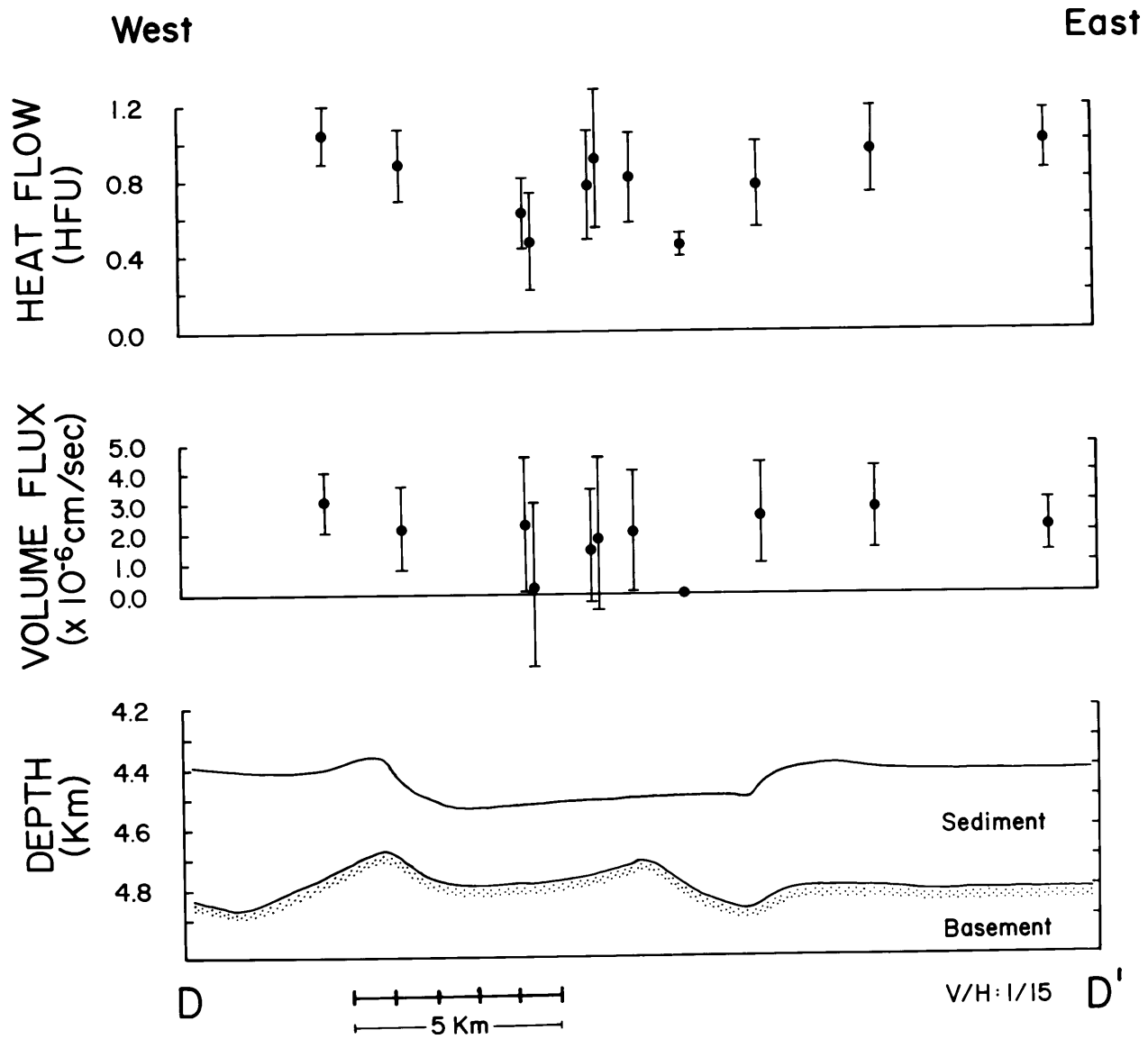
between 1 to 3×10^{-6} cm/sec, however, the standard deviations of these values are also very large. These results are consistent with the conclusions drawn in Appendix II based on the statistical analysis of the non-linear regression technique. For small values of Q, the resolution of the model parameters is poor, and it is difficult to determine with confidence the volume flux. In the real data this is shown by the large standard deviations in Figure 23 and Table 2.

All measurement locations in survey 2 have been assigned a B environment. Although there is definite curvature in these temperature measurements, due to the low heat flow and the uncertanties of the temperature measurements we cannot draw definite conclusions about the small scale variability of the thermal structure. However, the heat flow is remarkably low, well below 1 HFU, and the temperature gradients are non-linear.

The third survey was located at a transition from the low heat flow zone to the "normal" heat flow observed on the SCAN 10 profile (Figure 11). Figures 24 and 25 are the contoured maps of bathymetry and sediment thickness. The heat flow station identifications are plotted in Figure 24 and the results of the heat flow measurements are included in Figure 25. The seafloor topography consists of rolling hills of 50 meters relief with the exception of a large hill at $4^{\circ}01.5'N$, $114^{\circ}06'W$. Basement is covered by a uniform sediment blanket of 0.3 seconds reflection time thickness, except in the vicinity of the hill where it thins to about 0.05 seconds reflection time.

Twenty heat flow measurements were made in this survey located roughly along two east-west profiles marked B-B' and C-C'. The survey and the heat flow measurements were navigated around a radar reflector buoy centered

Figure 24. Bathymetry in corrected meters contoured at 25 meter intervals and locations of heat flow measurements in the KNORR 73-4 detailed heat flow survey centered at 4^ON, 114^OW. The location of the ship's track during the CSP and bathymetric survey is shown by light dashed lines.
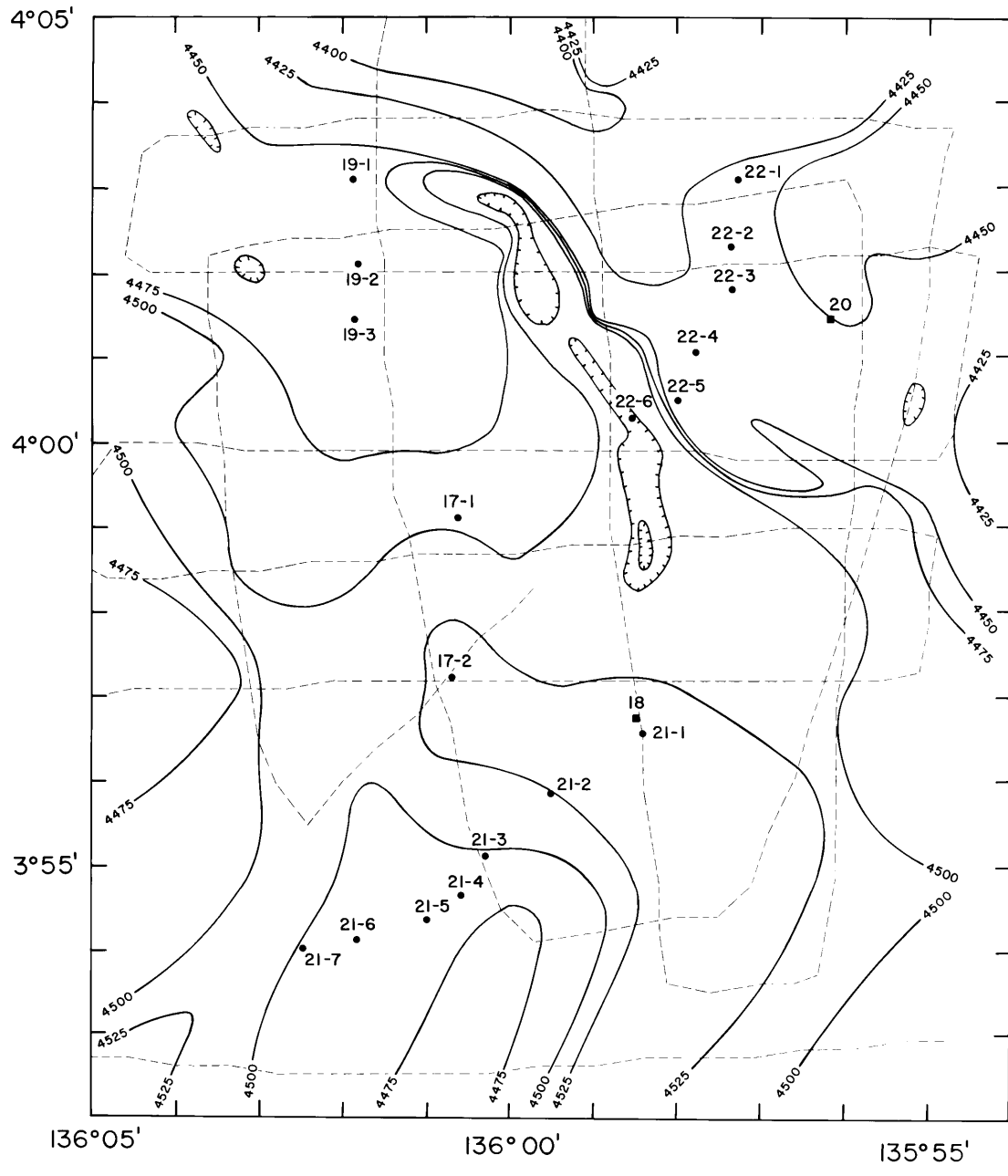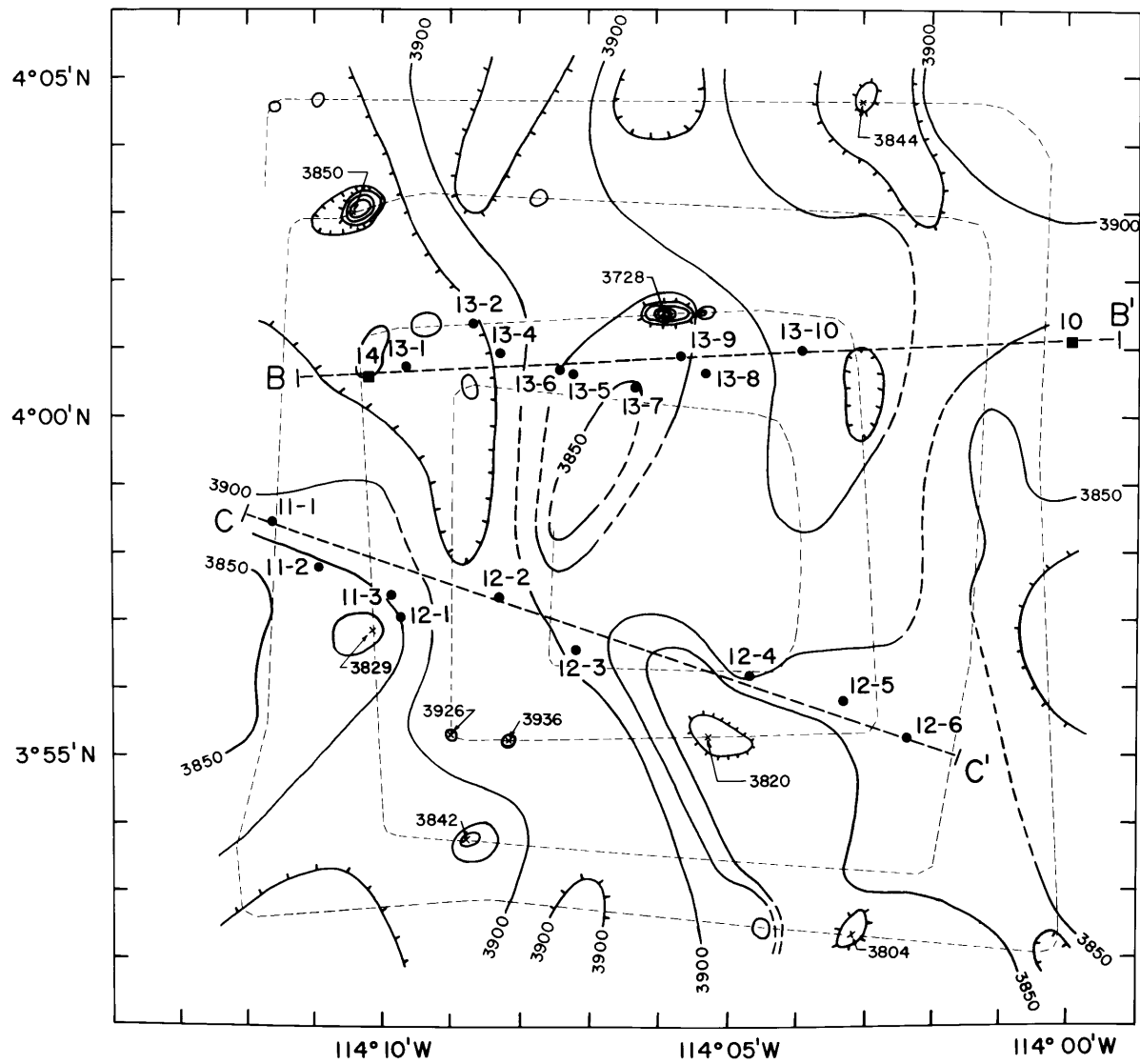
Figure 25. Sediment thickness in seconds of two way travel time contoured at 0.05 second intervals and heat flow values in heat flow units in the KNORR 73-4 detailed heat flow survey centered at $4^{\circ}N$, $114^{\circ}W$. The location of the ship's track during the CSP and bathymetric survey is shown by light dashed lines.
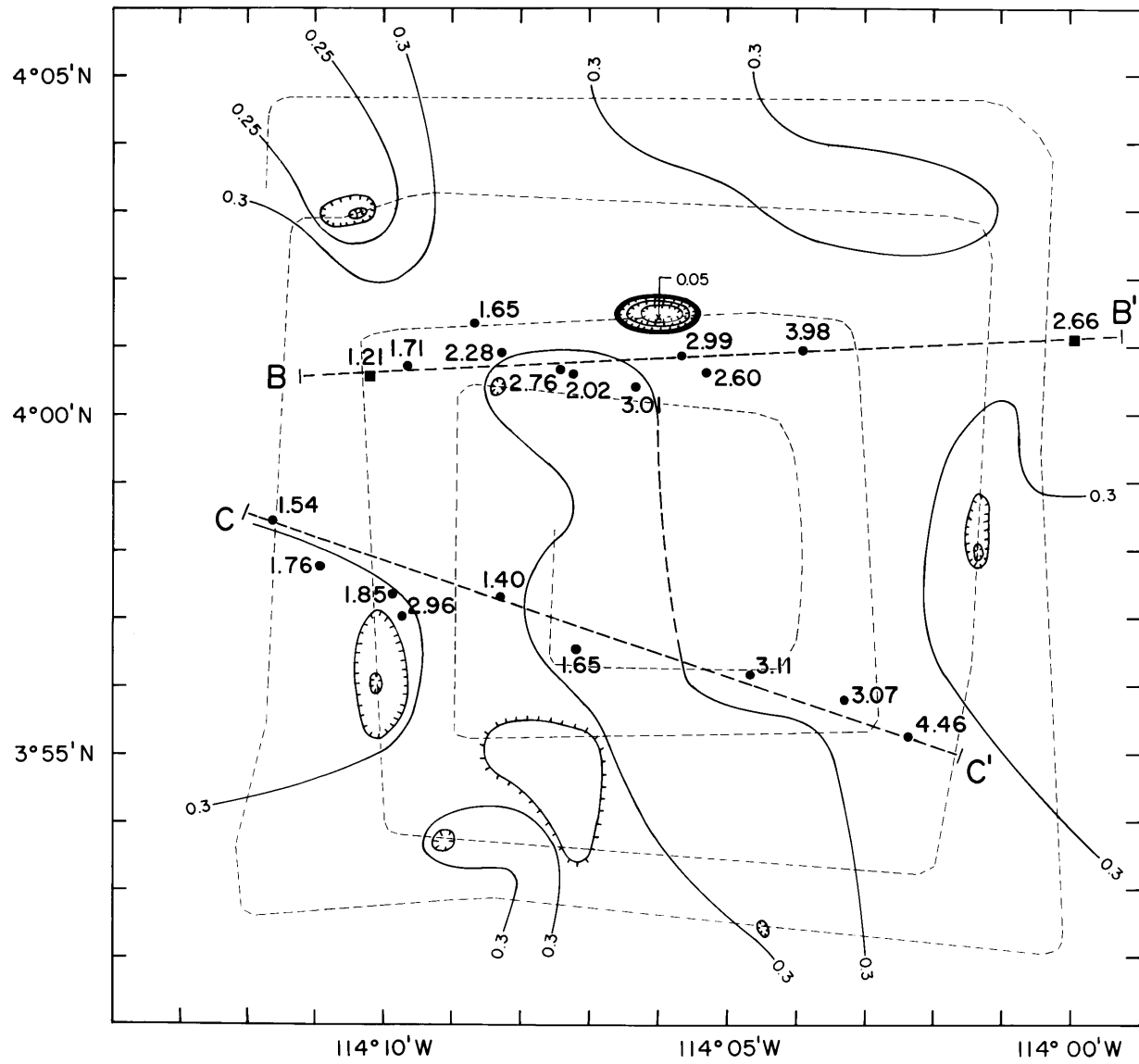
$3^{o}55'N$, $114^{o}07'W$. Cross-sectional line drawings of the basement and sediment cover along these two profiles and plots of heat flow results are shown in Figures 26 and 27. In both profiles the heat flow increases from west to east from about 1.2 HFU to over 3.0 HFU. All values of volume flux are positive, thus indicating flow out of the seafloor. There is no evidence of recharging flow. The temperature versus depth profiles for these stations are shown in Figures 28 and 29. For the situation where recharge occurs we would expect to observe an isothermal or very low gradient temperature profile depending on the rate of recharge, and to calculate essentially a low heat flow value.

For line B-B' the calculated flow rates show a cyclic pattern that varies from less than 10^{-6} cm/sec to about 7.5×10^{-6} cm/sec over 10 km. However, this is somewhat obscured by the uncertainty in the determination of these values. Along line C-C' the flow rates range between 1 to 3×10^{-6} cm/sec and do not follow any particular pattern.

The hill 2-3 km north of line B-B' does not appear to influence to observed heat flow pattern. At station 5 from the 114°-$115^{o}30'W$ east-west profile (Figures 15 and 18), a high heat flow and a linear temperature gradient were observed. With the exception of station 10 the high heat flow observed in the eastern portion of the survey is associated with high flow rates (as high as 3×10^{-6} cm/sec). From Figures 26 and 27 there does not appear to be an obvious relationship between heat flow, basement topography and sediment cover. We cannot determine the cause of the observed eastward increase in heat flow from this small survey. From our regional data we know that the nature of the crust and sediment cover changes dramatically

Figure 26. Schematic diagram of basement and sediment thickness along profile B-B'. Also plotted are the best fit values and standard deviations of both heat flow and volume flux.

West   HILL   East

2KM NORTH
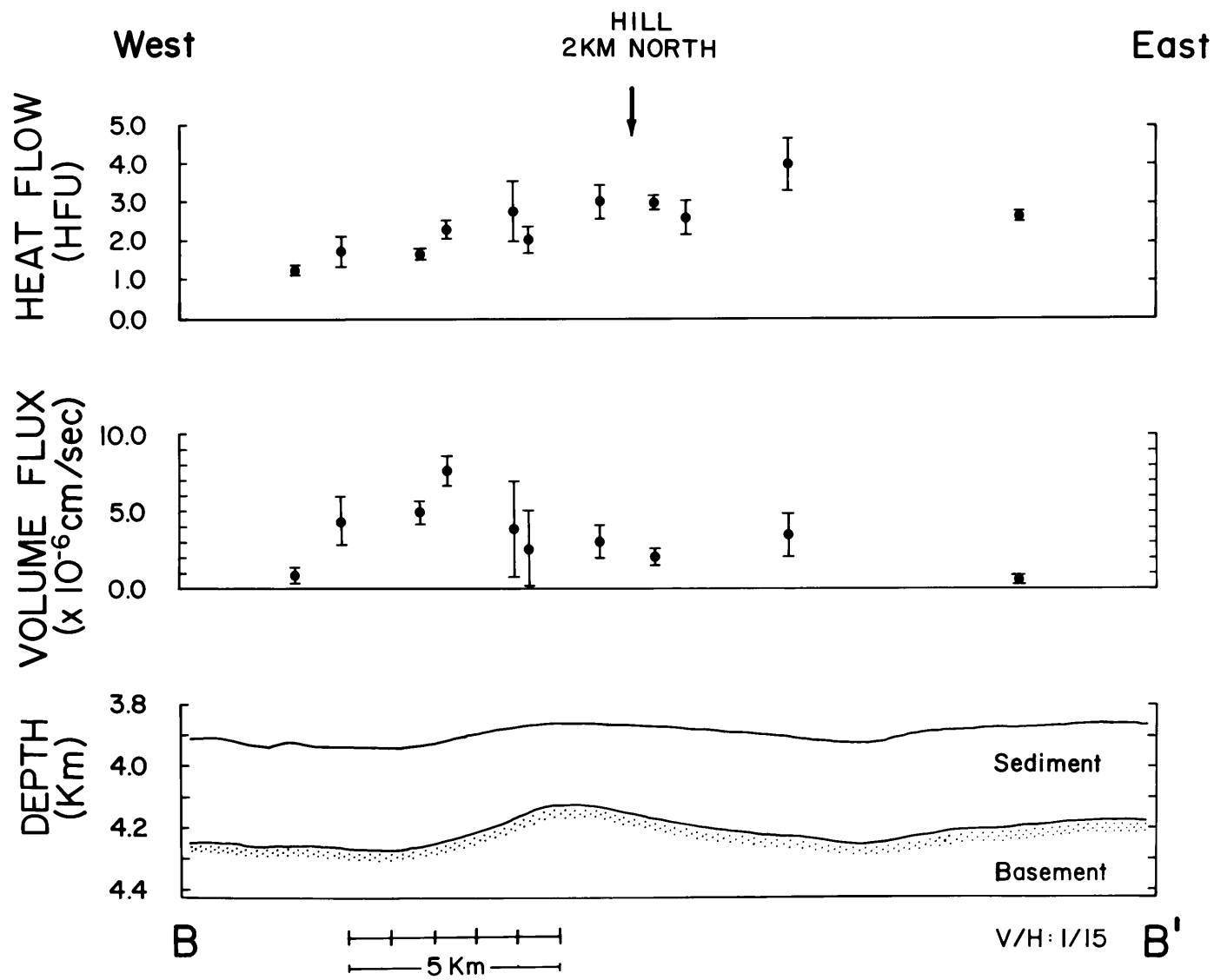
Figure 27. Schematic diagram of basement and sediment thickness along profile C-C'. Also plotted are the best fit values and standard deviations of both heat flow and volume flux.

West   East
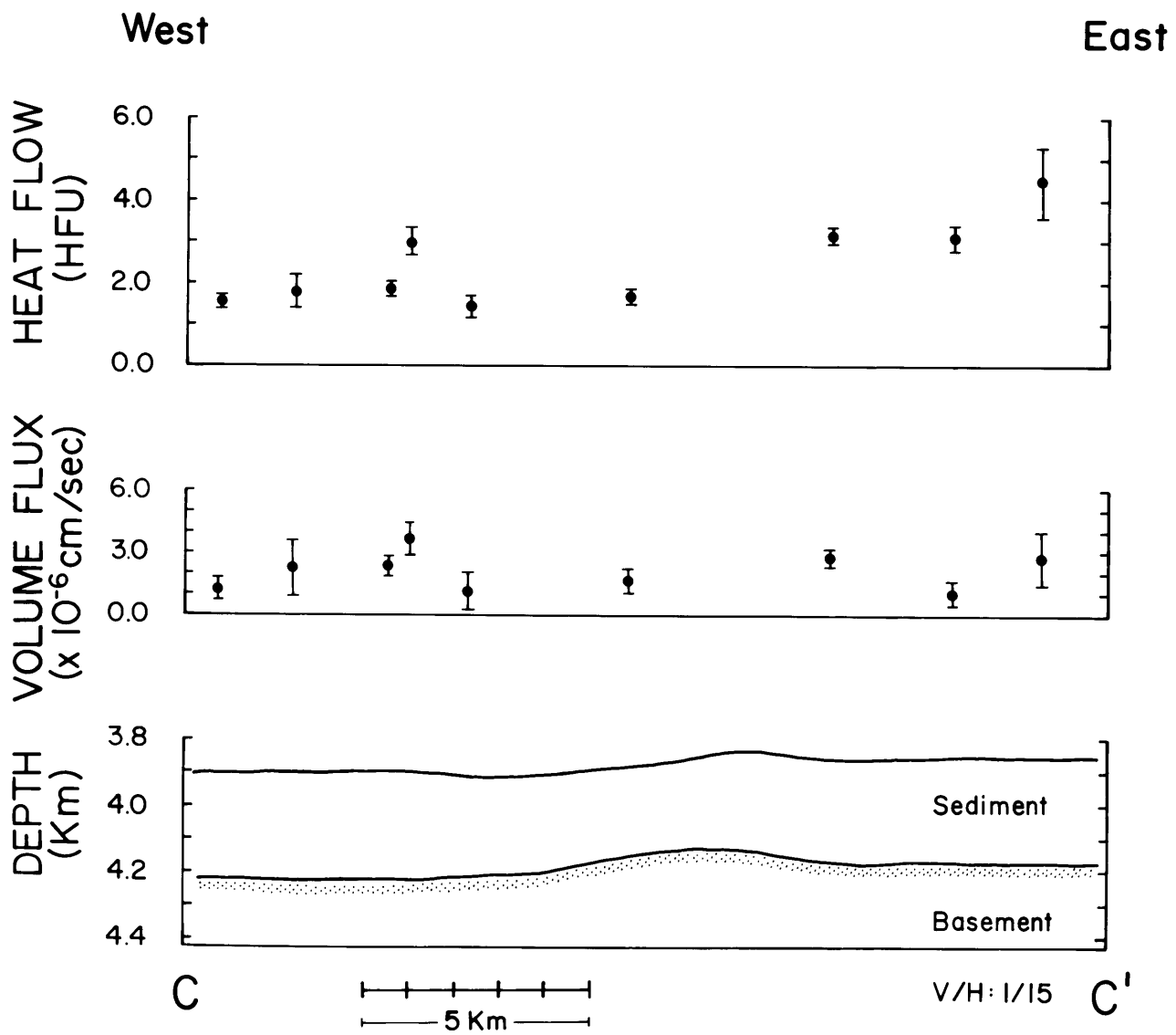
Figure 28. Temperature versus depth data corresponding to the stations

located along profile B-B'. Each profile is identified by station number

along with the value of heat flow and volume flux. Error bars assigned to

the temperature data are shown. The lines drawn through the temperature data

represent the best fit of a simple conductive/convective themal model (see

text). The profiles are staggered to avoid overlap.

DEPTH (meters)

B'
East

West
B

0.1°C

10
2.66
0.6

13-10
3.98
3.5

13-8
2.60
2.1

13-9
2.99
2.1

13-7
3.01
3.0

13-5
2.02
2.5

13-6
2.76
3.8

13-4
2.28
7.6

13-2
1.65
4.9

13-1
1.72
4.3

14
1.21
0.8

0 1 2 3 4 5 6 7 8 9 10 11 12

Figure 29. Temperature versus depth data corresponding to the stations located along profile C-C'. Each profile is identified by station number along with the value of heat flow and volume flux. Error bars assigned to the temperature data are shown. The lines drawn through the temperature data represent the best fit of a simple conductive/convective thermal model (see text). Each temperature profile is shifted to the right by several tenths a degree to avoid overlap.

West C

East C'

DEPTH (meters)

11-1	11-2	11-3	12-1	12-2	12-3	12-4	12-5	12-6
1.54	1.76	1.85	2.96	1.40	1.64	3.11	3.07	4.41
1.2	2.2	2.3	3.6	1.1	1.6	2.7	1.0	2.7

0.1°C
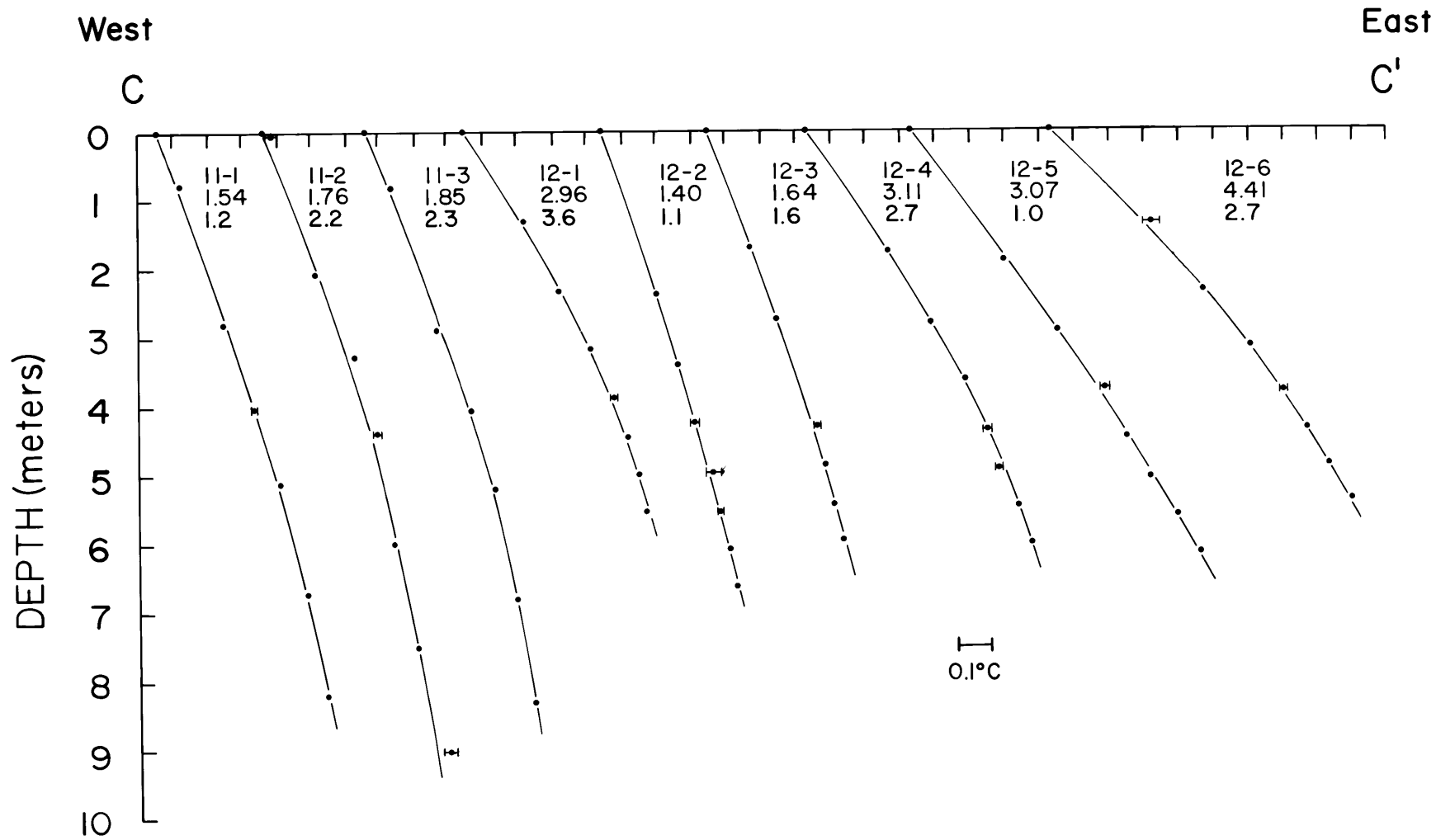
from west to east, accompanied by an equally dramatic change in heat flow (Figure 16). It is possible that the scale of the transition from the low heat flow zone to "normal" gradients is larger than the size of our survey, and that linear gradients would be observed (similar to the SCAN 10 data) if our profiles extended further to the east.

From the results collected on PLEIADES 3 and KNORR 73-4, a relatively high heat flow and a volume flux less than 10^{-6} cm/sec have been observed for measurements located in A environments (see Tables 2 and 3). Scattered heat flow values and a wide range of volume flux with large standard deviations characterized the measurements observed in other environments. In Figure 30 the results of all the heat flow measurements including the survey data from KNORR 73-4 are plotted as heat flow versus volume flux. A environments are indicated by circles and B, C and D environments are marked with crosses. Also included in this figure are the standard deviations of these parameters shown as thin lines. There is a high correlation of low volume flux and small standard deviations with A environments. In Figure 31 heat flow values observed in A environments are plotted versus crustal age. It is clear that many of these stations have values substantially less than theoretical. Likewise, in Figure 30 there is a high correlation of poorly constrained large values of W with B, C and D environments. In other words, more nearly linear gradients are associated with A environments and non-linear with the other classifications.

The assignment of environments to stations using the 2-D CSP profiles are straightforward, however, there is always some uncertainty in assigning A environments due to the obvious lack of information perpendicular to the track. In Figure 30, two stations assigned A environments have volume fluxes

Figure 30. Heat flow plotted versus volume flux for all data from KNORR

73-4. A environments and B, C and D environments are respectively indicated

by circles and crosses. Standard deviations of these parameters are shown by

thin lines.

- A environment
- × B,C and D environments

HEAT FLOW

VOLUME FLUX   (x 10^{-6}cm/sec)
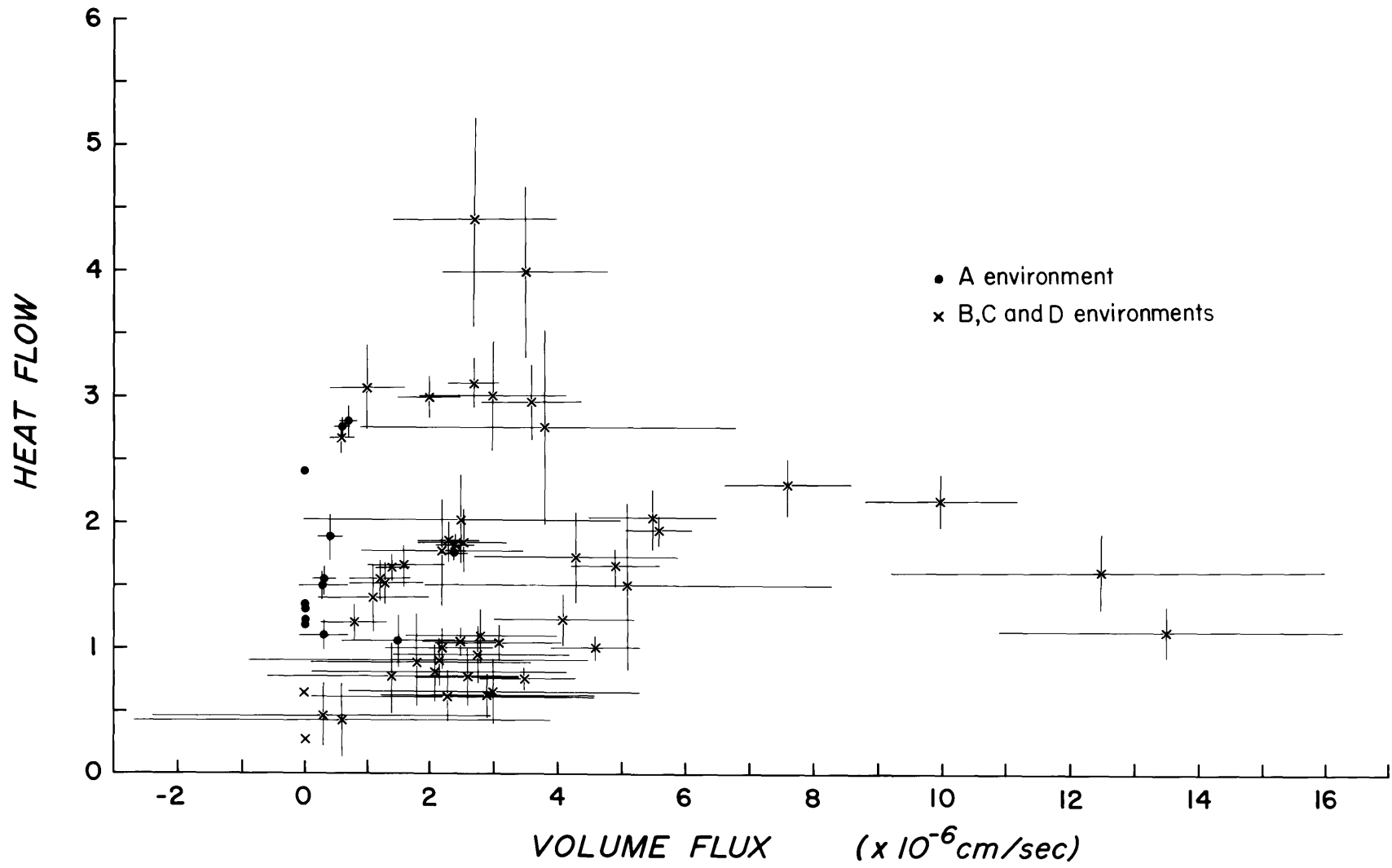
Figure 31. A plot of the log of A environment heat flow values against the log of crustal age. Also shown is the average heat flow value from survey 1 and the VEMA 24-3 average value from Figure 3.
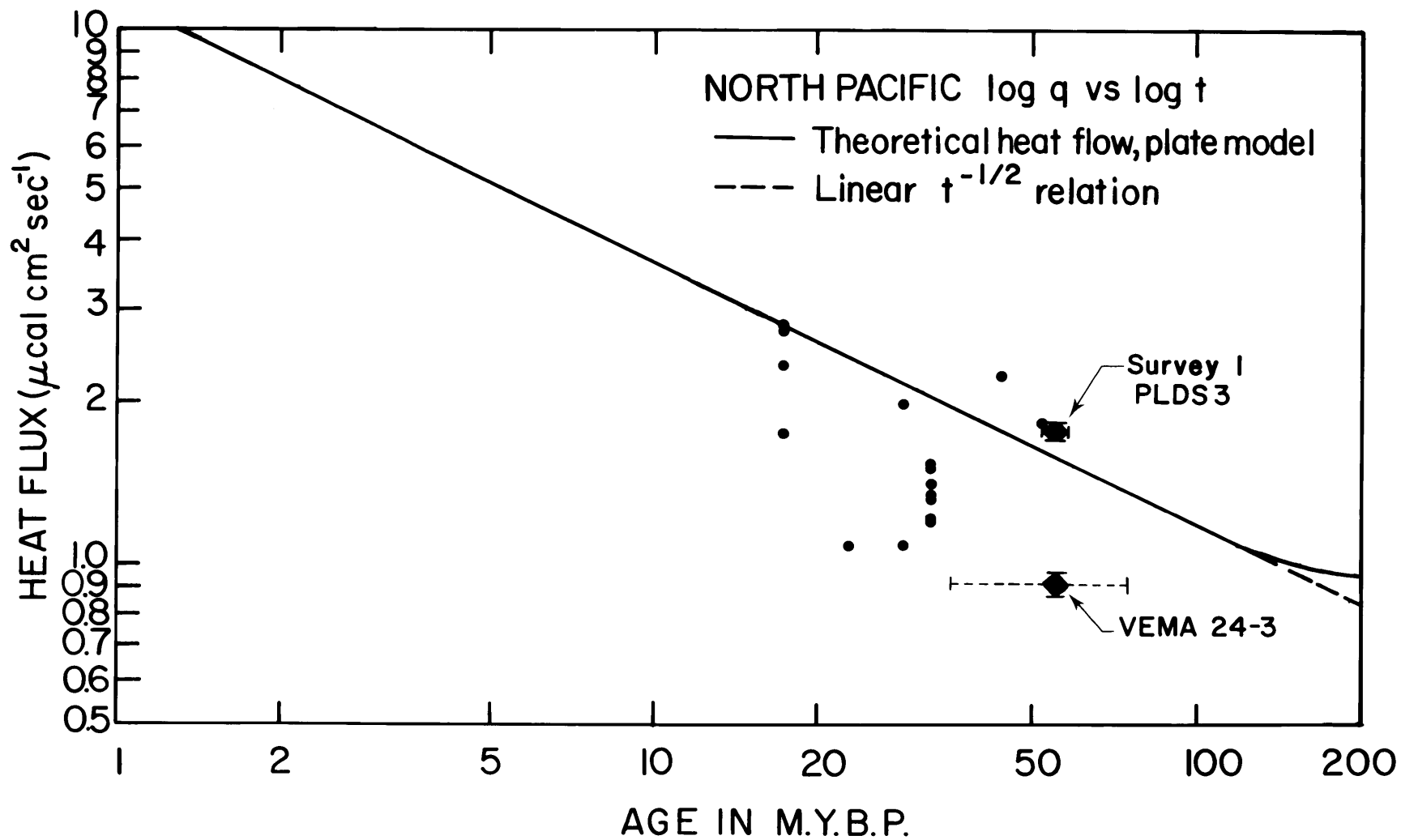
greater than 10^{-6} cm/sec and plot well with the other stations. One of

these measurements has a poorly constrained volume flux that may reflect the

quality of the data. The other measurement was a piston core, station 15,

where the thermal conductivity structure was well determined (Figure 2).

There is little correlation between heat flow and volume flux irrespective of

environment.

We cannot resolve why several of the A environment stations from VEMA

24-3 are incompatible with the sediment blanket model. Two possible

explanations are that due to the two-dimensionality of the CSP tracks, they

were misassigned A environments, or less likely that the heat flow

measurements themselves are of poor quality. In the next section we show

support for the former explanation.

Regional Study of Heat Flow:

Figures 1 and 10 show the distribution of heat flow measurements and

summarize the tectonic and sedimentary environment of the equatorial Pacific

Ocean. In some areas the heat flow coverage is sparse. This region is well

traversed with CSP tracks enabling the sediment cover to be adequately

contoured. The tectonic reconstruction is complicated due to the low

inclination of the magnetic field near the equator. Based on DSDP,

topographic and CSP data the tectonics of the equatorial Pacific appears to be

complex, as previously discussed. Although the sediment cover between the

equator and 5°N is thick, it is perforated by numerous outcrops, many

located in regions of intense basement roughness. Most of the low heat flow

zone is covered by over 200 meters of sediment and broad areas of flat

basement, probably horizon B, exist between 115° and 131°W.

There are several areas within the low heat flow zone that should be discussed in light of the observations from the CSP track and detailed survey studies. In the vicinity of 2°N, 119°W, three high heat flow measurements exist, all located in A environments (one from KNORR 73-4 and two from VEMA 18-15). Located slightly to the west are three low heat flow measurements, located in B environments (one from VEMA 24-3 and two from VEMA 18-15). From the VEMA 24-3 CSP records (Figure 12), it appears that to the west of VEMA 24-3 station 34 (0.41 HFU) the basement is rough and to the east it is smooth.

Several stations from PLEIADES 3 and KNORR 73-4 are located at 1°N between 127° to 129°W, nine of which are in A environments. Flat basement (horizon B) is observed throughout this area. The average heat flow for these measurements is 1.40 ±0.26 HFU. Although this is significantly higher than the other measurements within the low zone, for an estimated crustal age of 26 to 30 ma this average value is still quite low.

Between 131° and 138°W, the roughness of the basement increases dramatically. This is shown in the CSP records from VEMA 24-3 (Figure 13), however, in these and other east-west profiles the basement roughness is not as striking as some other tracks oriented in a more north-south direction such as CONRAD 10-06, SCAN 8, SCAN 9 and DSDP 9. This broad area of rough basement appears in the east-west CSP records from PLEIADES 3 (Figure 14) only as a short segment of rough basement along a profile that otherwise shows very flat basement. We have already speculated that this localized basement roughness may be related to the termination of the Galapagos Fracture Zone and the reorientation of spreading direction. The heat flow in this region is very

low, directly correlated with the basement roughness. To the west the CSP coverage is sparse and the nature of the basement is unknown. Many of the A environment VEMA 24-3 heat flow stations that contradict the thermal models are located west of 135°W. Figures 1 and 10 show that very little data exists in the vicinity of these measurements. If the rough basement observed between 131° and 140°W continues westward, it is possible that the single line CSP data at these stations is not adequate for the assignment of environments.

South of 5°N significant changes in the basement roughness occur at 131°W. To the west the basement is very rough and to the east there are isolated outcrops and localized areas of rough basement. Within both areas, heat flow well below 1 HFU has been observed. From the existing CSP coverage many of these values have been correlated with outcropping basement, however, at several stations located in A environments, heat flow well below the theoretical was measured. From the data plotted along the CSP tracks, there are significantly fewer outcrops east of 131°W than to the west. It is likely that between 115° and 130°W there are broad areas of flat basement and thick sediments where normal heat flow would be measured, however, due to the lack of measurements and the high occurrence of B environments at the stations that do exist, we cannot confirm this.

Average values of the A environment heat flow values plotted in Figure 31 are listed in Table 4. The three KNORR 73-4 measurements located at 114°W have been averaged with the SCAN 10 A environment data. This revised heat flow average is 2.48 ± 0.50 HFU. The average of the A environment measurements located on crust between the ages of 23 and 32 ma is 1.37 ± 0.27 HFU. Although

this is greater than the average value obtained from the VEMA 24-3

measurements west of 130°W, 0.92 ± 0.48 HFU, this average is still well below

the theoretical for this range of crustal age. We cannot account for this

discrepancy between observed and theoretical heat flow. The heat flow average

for the measurements in survey 1 is 1.76 ± 0.30 HFU which is in good agreement

with the theoretical value of 1.60 HFU for crust of about 55 m.y. From

Figures 19 and 20, survey 1 is located in a B geological environment. It is

possible that hydrothermal circulation within the survey 1 crust has ceased or

has been attenuated to the point where it no longer has an influence on the

surficial heat flow.

In Figure 32 the log of the heat flow averages reported in Table 4 are

plotted versus the log of crustal age. The agreement of the data from 114°W

and the PLEIADES 3 detailed survey with the theoretical values is apparent as

well as the lack of agreement of the KNORR 73-4 and VEMA 24-3 averages.

SEDIMENT PHYSICAL PROPERTIES:

The convection/conduction heat transport model used in the data reduction

predicts vertical fluid velocities on the order of 10^{-6} cm/sec. Such flows

appear surprisingly high, especially when compared to the hydraulic

resistivity of the sediment layer. Crowe and Silva (in preparation) conducted

a laboratory study of the permeabilty characteristics of several biogenic

sediment samples obtained from KNORR 73-4 station 15 and found permeabilities

of order of magnitude 10^{-6} cm/sec at in-situ values of void ratio.

Several of the geomechanical properties of the sediments in this core are

plotted versus depth in Figure 33. From this figure we can observe the

Table 4. Mean and Standard Deviations of Heat Flow Data
From the Equatorial Pacific Ocean

Area	Age Range m.y. B.P.	No. of Stations	Mean $\mu cal/cm^2$-sec	Standard Deviation $\mu cal/cm^2$-sec	Standard Error
a	15 - 20	10	2.48	0.50	0.17
b	23 - 32	10	1.37	0.27	0.09
c	35 - 75	6	0.92	0.48	0.20
d	50 - 60	20	1.76	0.30	0.07

a SCAN 10 and KNORR 73-4 A environment values at 114°W
b PLEIADES 3 and KNORR 73-4 A environment values 117°W-130°W
c VEMA 24-3 A environment values 130°W-150°W (Sclater et al., 1976)
d PLEIADES 3 detailed survey at 4°N, 136°W

Figure 32. Log of the heat flow averages and standard errors from PLEIADES 3 and KNORR 73-4 plotted versus the log of crustal age. Also included are the previously reported heat flow averages for the North Pacific (Sclater et al., 1976). The solid symbols represent the values listed in Table 4.
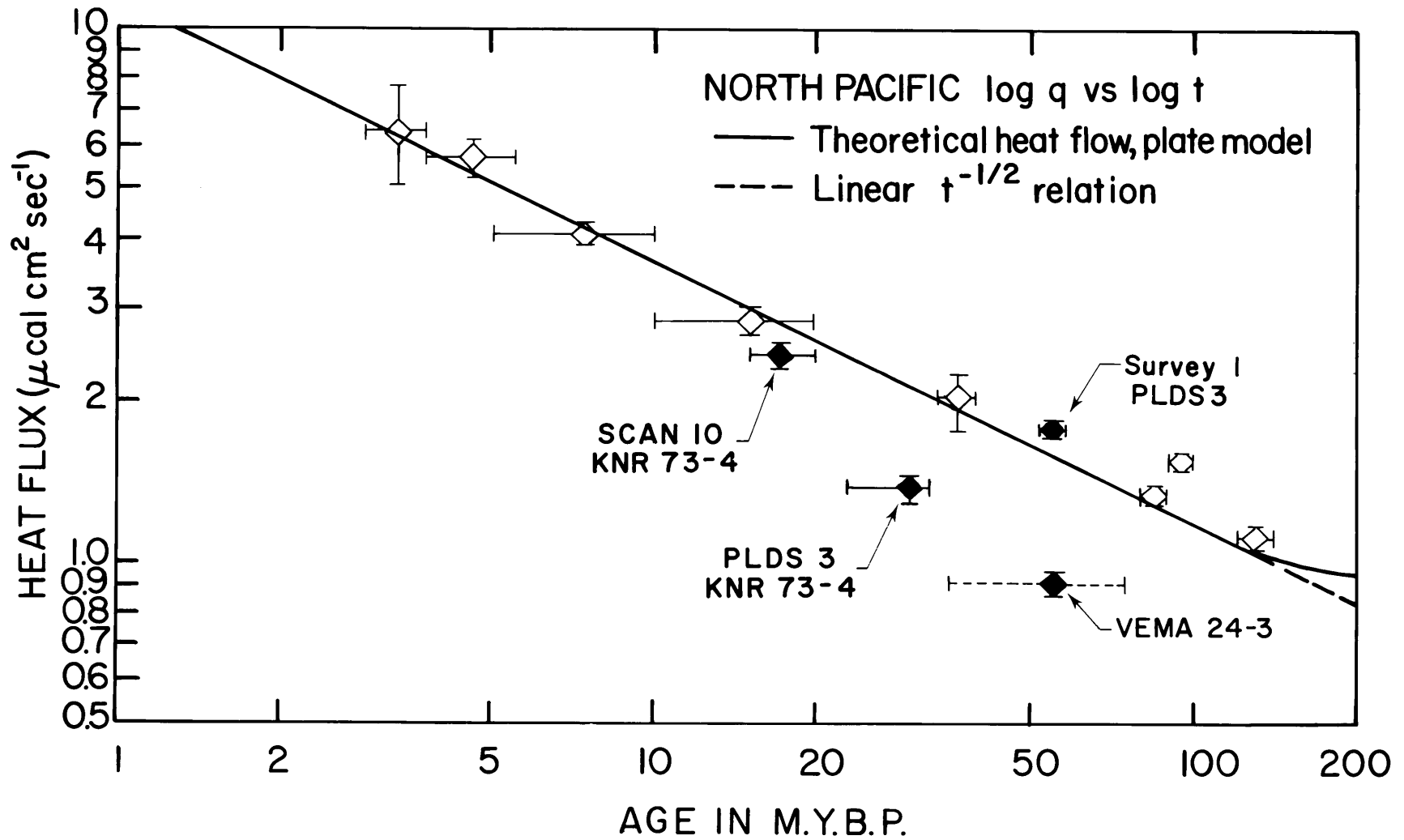
Figure 33. Geomechanical properties measured on sediment from KNORR 73-4 station 15. Water content is the ratio of the weight of water to solids x 100, void ratio is the ratio of void volume to solid volume, bulk density is in gm/cm^3, specific gravity is the ratio of solid density to that of water, shear strength is a relative measure of the resistence of the sediment to a penetrating cone, carbonate content (circles) and silica content (squares) in percent weight, thermal conductivity in $cal/cm-sec-^{0}C$ $x10^{-3}$.
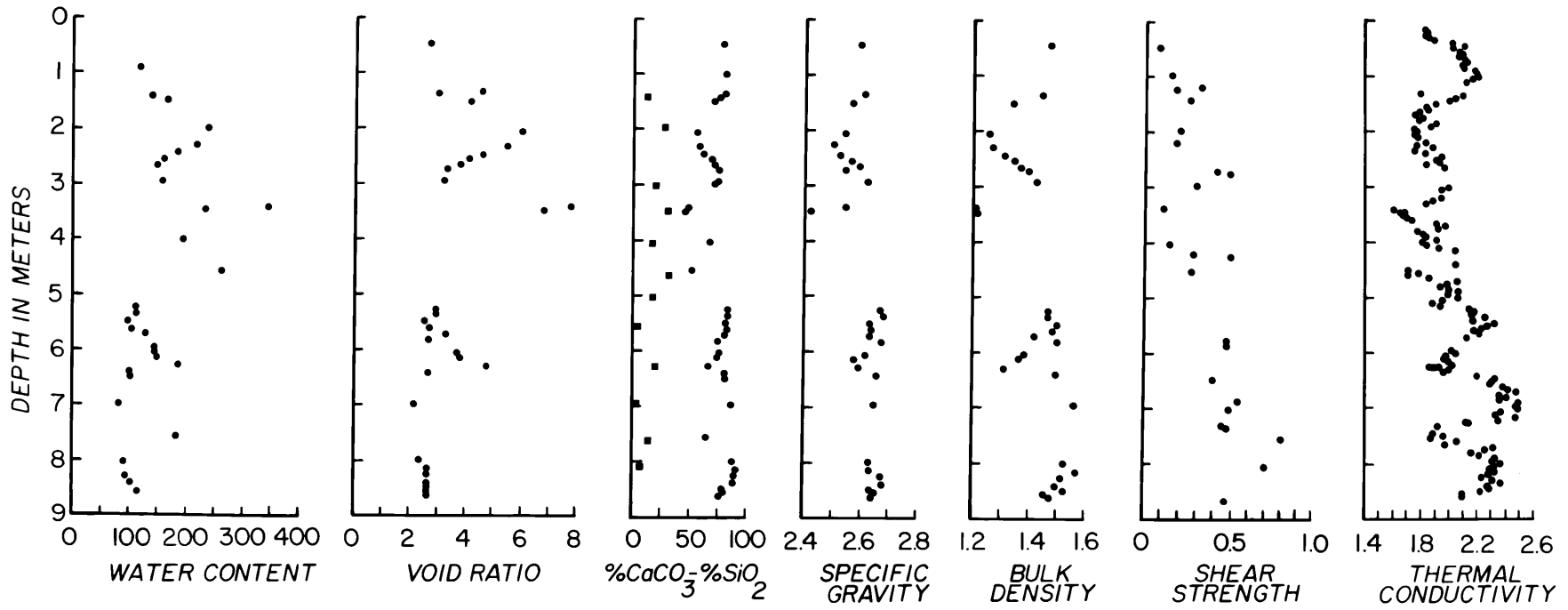
KNR73-4 STATION 15
PHYSICAL PROPERTIES

variation of thermal conductivity with respect to other physical properties. Of interest is the good inverse correlation of both thermal conductivity and $CaCO_3\%$ with water content.

Values of thermal conductivity measured on sediment recovered during KNORR 73-4 station 15 using the needle-probe technique of Von Herzen and Maxwell (1959), corrected to in-situ pressure and temperature, are plotted versus weight percent water in Figure 34. Also plotted are the relationships between thermal conductivity and percent weight of water from Ratcliffe (1960) and Lachenbruch and Marshall (1966). The equation for our best fit to the data is

$$K = \frac{1}{1.475w - 0.160} \tag{6}$$

where w is water percent wet weight. This relationship parallels that of Lachenbruch and Marshall (1966), and is offset slightly towards higher conductivities. This data appears to be the result of a two end member system, $CaCO_3$ and SiO_2. The study of Lachenbruch and Marshall (1966) involved Arctic Ocean sediments. There is no reason to expect these data sets to be similar. Values of thermal conductivity of globigerina oozes published in Clark (1966) are slightly less than the values observed for glacial clays/globigerina oozes. When the accuracy of our measurements is considered (between 5 and 10 percent), the two data sets are somewhat compatible. The relationship of Ratcliffe (1960) is well out of the range of the errors in our measurements, reflecting the wide range of sediment types used in that study.

Carbonate content is plotted versus water content in Figure 35. Changes

Figure 34. Plot of thermal conductivity versus percent water of total weight for KNORR 73-4 station 15 . The solid line is the best fit of an equation of the form $K = (a + bw)^{-1}$ to this data where K is thermal conductivity and w is percent water by weight (see text). The dashed and dotted lines are the best fits of the same equation to other sets of deep sea sediment thermal conductivity measurements published respectively by Lachenbruch and Marshall (1966) and Ratcliffe (1960).
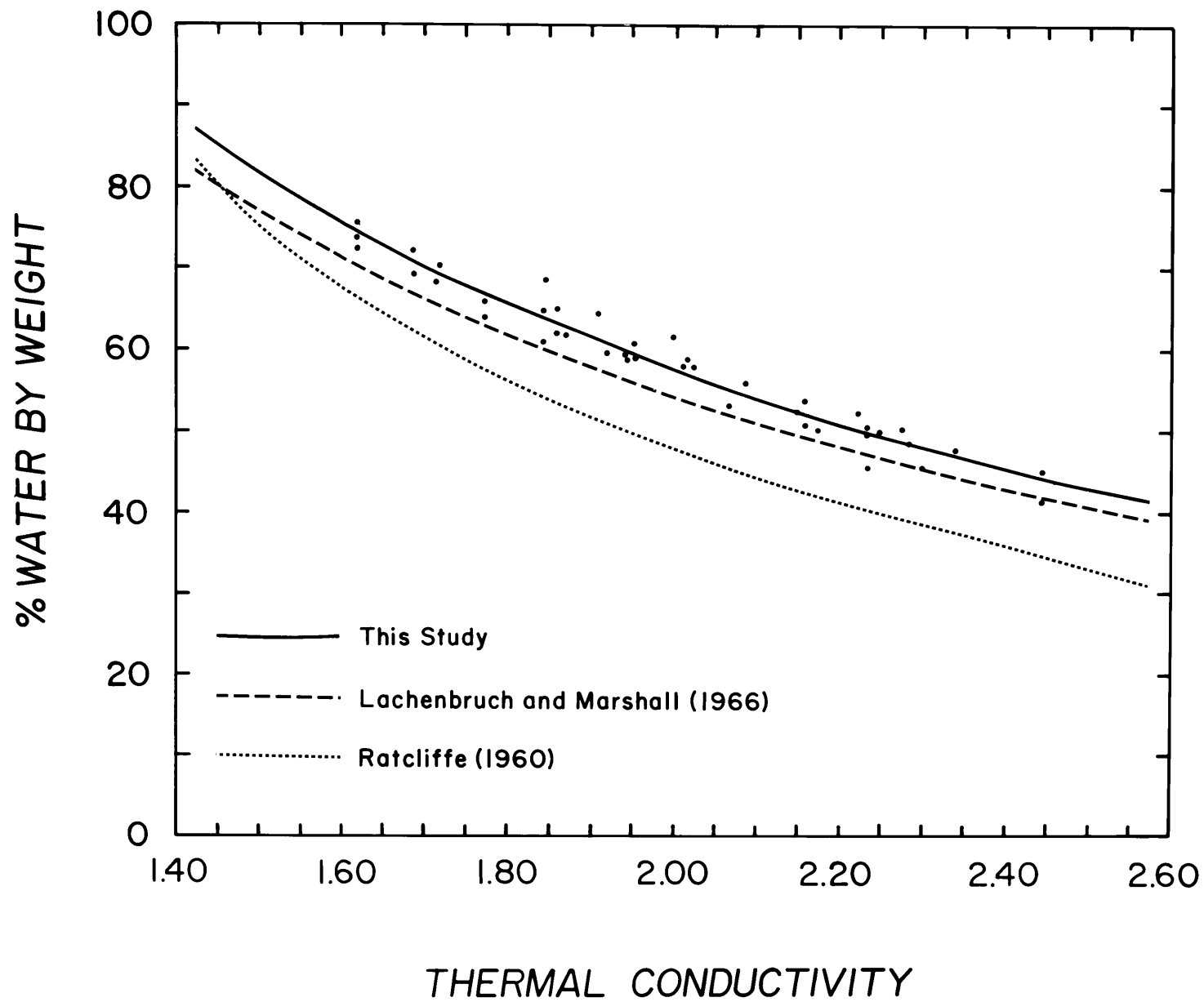
in the sedimentation pattern related to glacial/interglacial stages control the carbonate content (Arrhenius, 1952). This is apparent in Figure 33. During glacial periods, the concentration of carbonate particulates greatly exceeds that of siliceous, resulting in a low water content (about 100%) and a high thermal conductivity (greater than 2.0 mcal/cm ^{o}C sec). During interglacial periods the sedimentation rate for carbonate is low while the siliceous component stays somewhat constant resulting in a major SiO_2 component. Higher water contents (greater than 200%) and lower values of thermal conductivity (less than 1.8×10^{-3} cal/cm^2 ^{o}C sec) occur.

Profiles of thermal conductivity based on widely spaced measurements (25 cm or greater) along the recovered core from stations in the equatorial Pacific exhibit great scatter (Figure 2). From Figures 34 and 35 this scatter in the thermal conductivity measurements appears to be real and reflects changes occuring in the sedimentation patterns.

As a sediment consolidates, void ratio varies as the log of vertical stress (Skempton, 1970). The relationship between permeability and vertical stress is also logarithmic. Crowe and Silva (in preparation) measured sediment permeability at various states of sample consolidation. From this data a rough model of permeability as a function of overburden stress can be constructed. This is formulated as follows:

$$\sigma_v = \int_0^z \gamma_b \, dz \qquad\qquad (7)$$

where σ_v is effective vertical stress and γ_b is buoyant density. γ_b can be written as

Figure 35. Percent $CaCO_3$ plotted versus water content for measurements

obtained from KNORR 73-4 station 15.
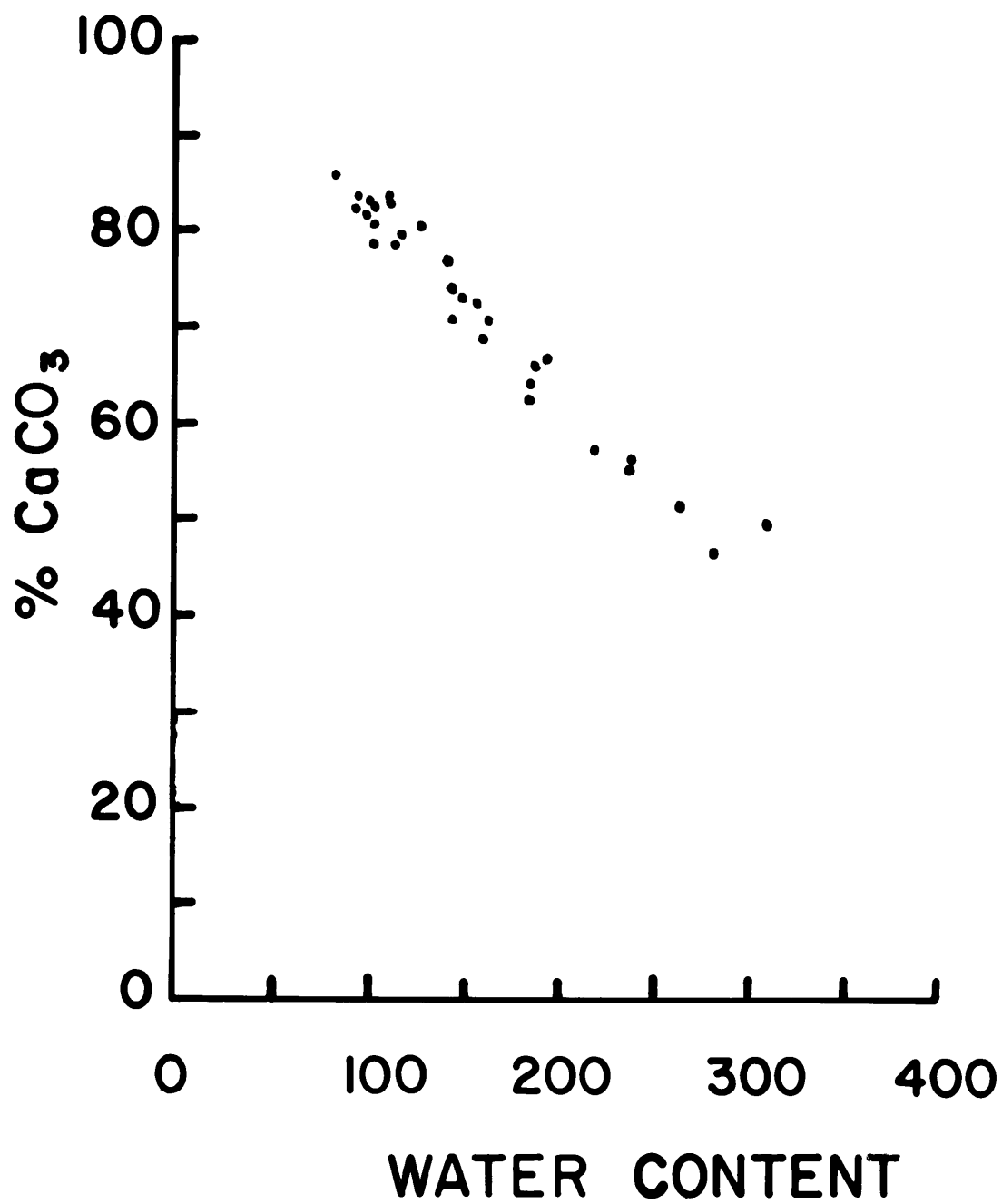
$$\gamma_b = \frac{G - 1}{1 + e} \gamma \qquad (8)$$

G equals specific gravity of the solid fraction, e equals void ratio and   is the density of water. Using the experimental data from Crowe and Silva (in preparation) and other unpublished consolidation data from PLEIADES 3 and KNORR 73-4 stations, relationships of both permeability and void ratio with the log of vertical stress have been constructed for equatorial Pacific sediments. Assuming a log relationship between e and σ_v, e = $f(\sigma_v)$ = a + b log σ_v, and solving equations 7 and 8 for z we get a relationship between vertical stress and depth

$$z = z_0 + \frac{1}{\gamma} \int_0^{\sigma_0} \frac{1 + f(\sigma_v)}{G - 1} dz \qquad (9)$$

where z_0 and σ_0 are the in-situ depth and vertical stress for the function $f(\sigma_v)$. Evaluating the integral in equation 9 gives

$$z = z_0 + \frac{1}{\gamma (G-1)} [(1 + a - b)(\sigma - \sigma_0) + b(\sigma \log \sigma - \sigma_0 \log \sigma_0)] \qquad (10)$$

Figure 36 is a plot of the change of effective stress and permeability with depth based on equation 10 using the consolidation and permeability data obtained from the KNORR 73-4 samples. The range of values plotted for vertical stress versus depth represents the cumulative results of over ten consolidation measurements. The two ranges of values plotted for permeability versus depth correspond to results obtained from both a calcareous ooze, 82% $CaCO_3$, 5% SiO_2, and a carbonate-siliceous ooze, 55% $CaCO_3$, 30% SiO_2. The maximum vertical stress applied during the consolidation measurements was

Figure 36. Plot of the change of effective stress and permeability with depth based on consolidation and permeability measurements conducted using sediments from 7PC, station 15.

VERTICAL STRESS (kg/cm²)

DEPTH (meters)

PERMEABILITY (cm/sec)

82% CaCO₃
5% SiO₂

55% CaCO₃
30% SiO₂

DEPTH (meters)
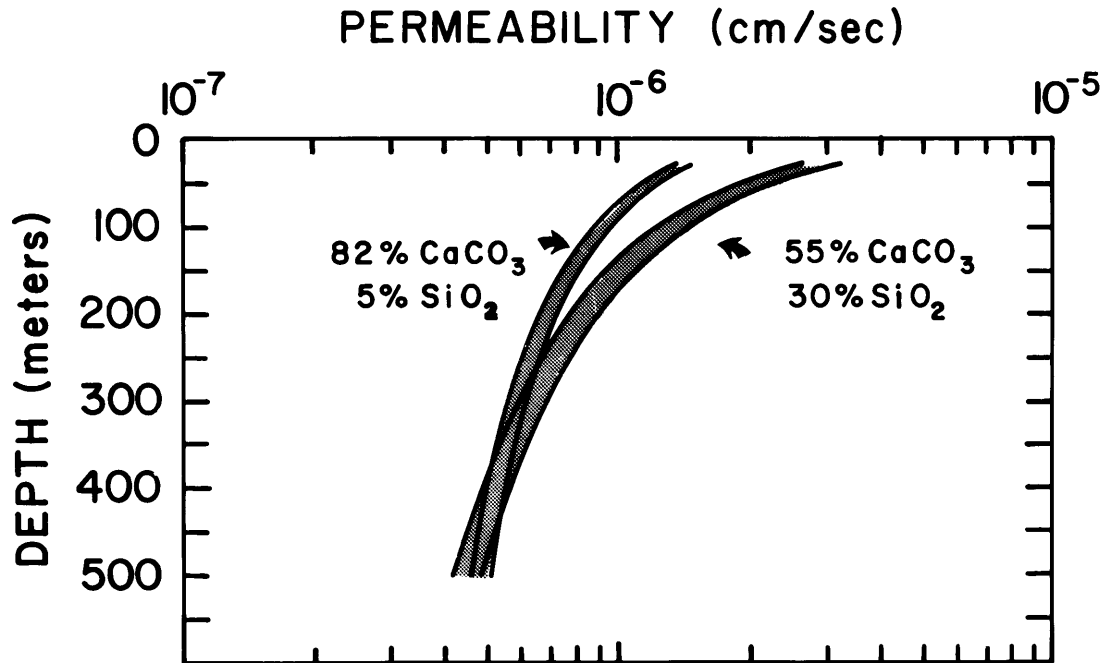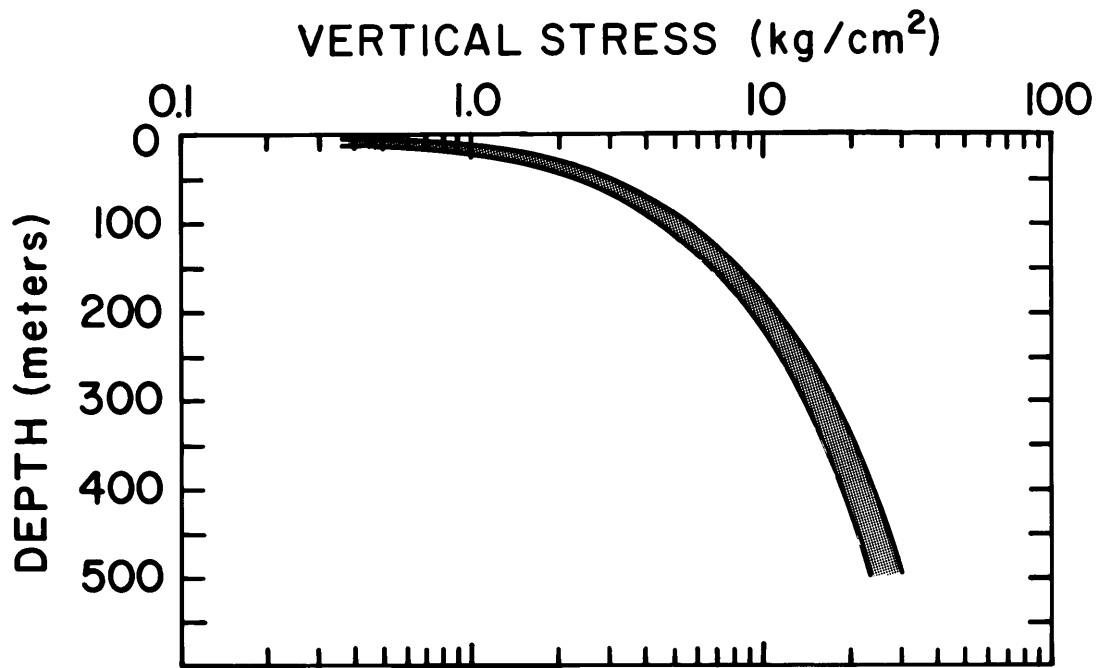
8.2 kg/cm^2 which corresponds to the overburden stress at between 150 to 200 meters in Figure 36. This plot suggests that permeability changes by less than an order of magnitude over the sediment thicknesses observed in the equatorial Pacific.

If we ignore such processes as diagenesis and slow chemical reactions that occur over millions of years, we can calculate the pressure gradients across the sediment layer necessary to drive the fluid flow predicted by the volume flows calculated using the non-linear temperature gradients. Using Darcy's law (Darcy, 1865) we have

$$v = -(\frac{k}{\gamma}) \nabla P \tag{11}$$

where k is hydraulic conductivity (cm/sec) and ∇P is the pressure gradient. The balance of forces at any point in the sediment column is expressed in the effective stress ($\bar{\sigma}$) equation (Terzaghi, 1936)

$$\bar{\sigma} = \sigma - u \tag{12}$$

where σ is the total stress applied to the sediment and u is the pore pressure. Using Darcy's law, equation 12 can be rewritten as

$$\bar{\sigma} = \int_0^z \gamma_b \, dz - \gamma \frac{W}{k} z \tag{13}$$

The ratio of volume flux to permeability is critical in equation 13. For large values of W the values of permeability shown in Figure 36 will result in extemely large pressure gradients across the sediment layer. It is possible that if such a such a system existed the bulk permeability of the sediment layer would increase and probably never allow excessive pressure to build up,

(i.e. quicksand). However, from the consolidation tests run on samples from KNORR 73-4 cores there is no evidence of quick conditions existing (zero effective stress), in fact the sediments appear to be normally consolidated (zero excess pore pressure).

In Figure 37 excess pore pressures calculated for a range of volume flux values using the permeability profile from Figure 36 are compared with the profile of vertical stress from Figure 36. A volume flux of 10^{-7} cm/sec (profile A in Figure 37) does not require pore pressures that are large with respect to the lithostatic stress (L in Figure 37). It appears that a volume flux of 10^{-6} cm/sec will require pore pressures exceeding the overburden stress at some depth within the sediment column. For the results presented in Figure 37 it appears that a volume flux of 10^{-6} cm/sec (profile B) would not produce underconsolidated sediments in the upper few tens of meters, which is compatible with our consolidation tests. However, our results suggest that a volume flux on the order of 10^{-5} cm/sec (profile C) requires an extremely large pressure gradient to sustain it.

VOLUME FLUX ESTIMATES FROM PROFILES OF PORE WATER CHEMISTRY:

At three KNORR 73-4 sites, (stations 10, 14 and 15), estimates of volume flux based on profiles of temperature and pore water chemistry over a depth of eleven meters were compared (Crowe and McDuff, in preparation). The volume flux rates based on the geothermal data (Table 2) were approximately three orders of magnitude greater than those based on profiles of sulfate, 1.2 - 2.4×10^{-9} cm/sec. This difference is difficult to explain by experimental uncertainty, and attempts to account for the observed geothermal data using

Figure 37.   Comparison of excess pore pressures calculated for a range of

volume flux values using the permeability versus depth profile from Figure 36

with the profile of lithostatic stress from Figure 36.   Profiles A, B and C

are the excess pore water profiles corresponding to volume flux rates of

10^{-7}, 10^{-6} and 10^{-5} cm/sec respectively.   The lithostatic stress profile

is marked L.

STRESS (kg/cm²)

DEPTH (meters)

A W = 10^{-7} cm/sec
B W = 10^{-6} cm/sec
C W = 10^{-5} cm/sec
L Lithostatic Stress
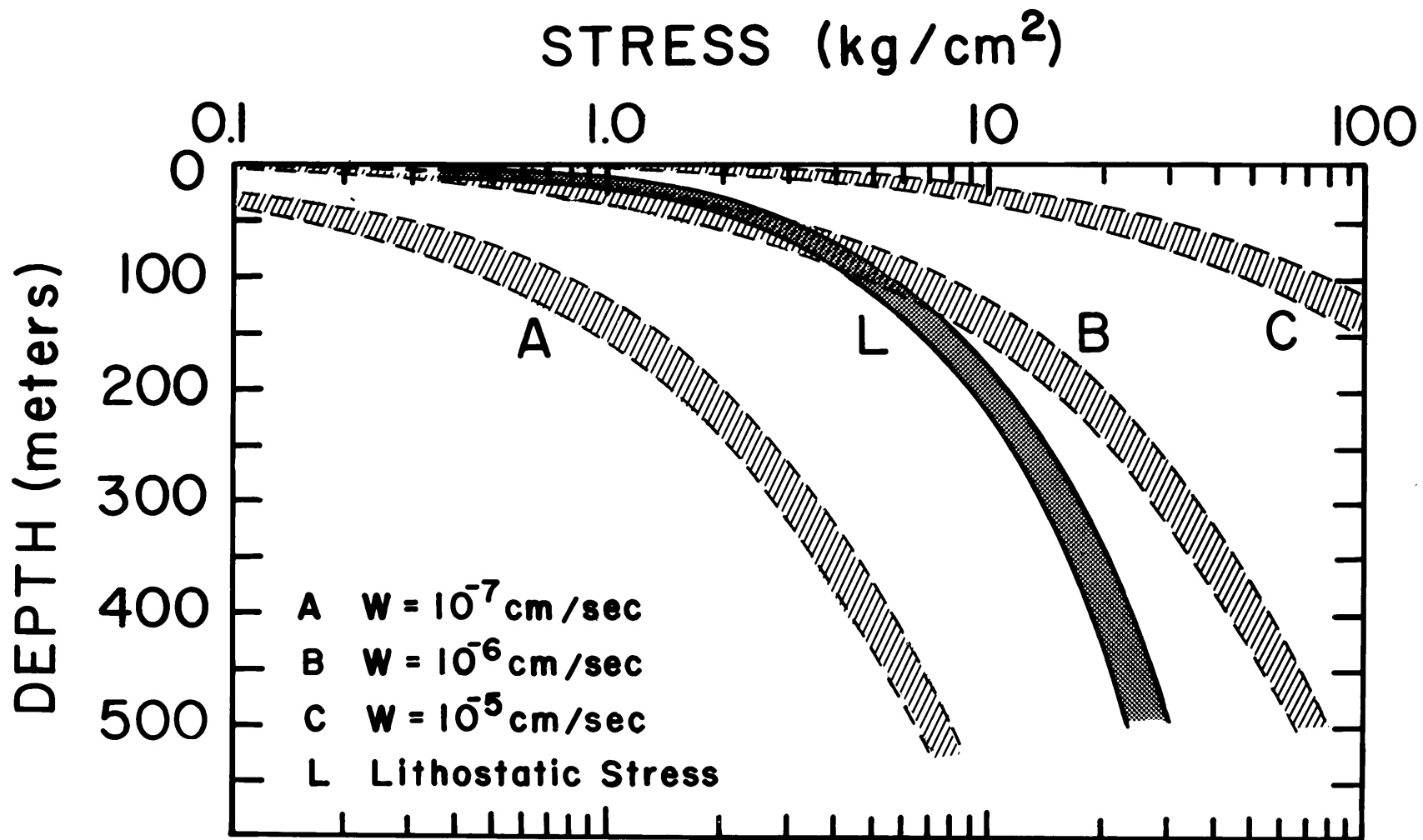
purely conductive thermal models are unsuccessful.

Conclusions

Low heat flow and non-linear temperature gradients were observed within the equatorial Pacific low heat flow zone using deeply penetrating temperature probes (6 to 11 meters). A simple relationship between heat flow, temperature gradient linearity and the geological environment of the measurement was observed. Measurements located in the vicinity of basement outcrops exhibited low heat flow and non-linear gradients. Where thick sediments completely covered the basement, higher values of heat flow and linear gradients were observed. However, these higher values of heat flow were not always compatible with values predicted by thermal models of oceanic crust.

A CSP study of the geological environment of the equatorial Pacific showed that although the region is covered by thick sequences of sediment, this sediment blanket is perforated by numerous basement outcrops. An area of intensive basement roughness was observed between 131° and $138^{\circ}W$ south of $5^{\circ}N$. The low heat flow zone is the direct consequence of the transport of heat by hydrothermal circulation controlled by these outcrops.

The transition of heat flow across a well-defined boundary of the low zone at $4^{\circ}N$, $114^{\circ}W$ was controlled by basement roughness. High heat flow was observed where the basement was flat and a variable heat flux where the basement was rough. Heat flow increased from 1.21 HFU to values greater than 3 HFU over a horizontal distance of 10 km. However, non-linear gradients were observed regardless of heat flow value. A detailed survey within the low zone showed consistently low heat flow values (about 0.5 HFU) over a 25 km

profile. Outside the low zone on crust of about 55 ma, an average heat flow value of 1.76 HFU was observed in a detailed survey where outcropping basement occurred. The theoretical value for crust of this age is 1.60 HFU. It is possible that that at this site crustal convection has ceased or has been greatly attenuated.

Application of a model of heat tranport through the sediment layer by both conduction and convection resulted in volume fluxes on the order of 10^{-6} cm/sec. A statistical analysis of our resolution of this parameter showed that flows less than 10^{-7} cm/sec could not be distinguished from the case of a linear temperature gradient if an instrumental precision of 0.001°C was assumed, and that as the value of heat flow decreased so did our resolution of the parameter. For values of heat flow less than 1 HFU, the ability to resolve flows of order of magnitude 10^{-6} cm/sec is greatly impaired.

Estimates of the pressure gradients necessary to drive the flow of fluid predicted by the convection/conduction model were made using the results of laboratory measurements of permeability and consolidation for equatorial Pacific sediments. These results showed that for volume fluxes greated than 10^{-6} cm/sec, excessive hydraulic pressures (greater than lithostatic) are required unless drastic alterations in the permeability of the sediment layer occur. The results of the consolidation tests and independent estimates of fluid flow using geochemical gradients at three sites in the equatorial Pacific do not support the volume flux model.

Conductive models fail to explain the low heat flow and non-linear gradients observed in the equatorial Pacific. The sense of fluid flow

suggested by the non-linear gradients is upward, out of the sediment column. No evidence of fluid recnarge was found. We feel that the large values of volume flux estimated from the geothermal data are difficult to support and should not be openly accepted as a valid heat transport mechanism until strong evidence, independent of the geothermal data, such as in-situ pore water chemical profiles or in-situ pore water pressure measurements, are obtained. Alternative explanations for the non-linear gradients include temperature perturbations resulting from the deployment of the temperature probe or incorrect estimates of sediment permeability due to unrepresentative samples or failure to reproduce in-situ conditions in the laboratory.

This page is intentionally blank.

P 147

BIBLIOGRAPHY:

Anderson, R. N., M. A. Hobart and M. G. Langseth, Geothermal convection through oceanic crust and sediments in the Indian Ocean, Science, 204, 828-832, 1979.

Anderson, R. N., M. G. Langseth, V. Vacquier And J. Francheteau, New terrestrial heat flow measurements on the Nazca Plate, Earth Planet. Sci. Letts., 29, 243-254, 1976.

Arrhenius, G., Sediment cores from the East Pacific. Properties of the sediment. Rep. Swed. Deep-Sea Exped. 1947-1948, 1, 1-228, 1952.

Berger, W. H. and T. C. Johnson, Deep-sea carbonates: dissolution and mass wasting on the Ontong-Java Plateau, Science, 192, 785-787, 1976.

Bookman, C. A., I. Malone And M. G. Langseth, Sea floor geothermal measurements from Conrad cruise 13, Columbia Univ. Tech. Rept., 5-CU-5-72, NTIS AD749983, 279pp., 1972.

Bredehoeft, J. D. and I. S. Papadopulos, Rates of vertical groundwater movement estimated from the Earth's thermal profiles, Water Resour. Res., 1, 325-328, 1965.

Brewer, P. G., Minor elements in sea water, in Chemical Oceanography, 1, 415-496, Riley, J. P. and G. Skirrow eds., Academic Press, 1975.

Broecker, W. S., Chemical Oceanography, Harcourt Brace Jovanovich, 214p., 1974.

Bullard, E. C., A. E. Maxwell and R. R. Revelle, Heat flow through the deep sea floor, Advances in Geophys., 3, 1956.

Bullard, E. C., The flow of heat through the floor of the Atlantic Ocean, Proc. Royal Soc. London A, 222, 408-429, 1954.

Carslaw, H.S. and J.C. Jaeger, Conduction of heat in solids, 2nd ed., Clarendon Press, Oxford, England, 1959.

Chase, T. E., Topography of the world's oceans, IMR Tech NCR PR 57, Scripps Inst. of Oceanogr. La Jolla, CA, 1975.

Clark, S. P., Handbook of Physical Constants, Geol. Soc. America. Mem. 97., 587p., G.S.A., New York, 1966.

Corliss, J. B., J. R. Dymond, L. I. Gordon, J. M. Edmond, R. P. Von Herzen, R. D. Ballard, K. Green, D. L. Williams, A. Bainbridge, K. Crane, and Tj. H. van Andel, Submarine thermal springs on the Galapagos Rift, Science, 203, 1073-1083, 1979.

Crowe, J. and A. J. Silva, Permeability measurements of Equatorial Pacific carbonate oozes using a direct measurement back-pressured technique, submitted to J. Geophys. Res.

Crowe, J. and R. E. McDuff, Comparison of geochemical and geophysical estimates of convective flow through marine sediments, submitted to Earth. Planet. Sci. Lett.

Darcy, H. P. G., Les fontaines publiques de Dijon, Victor Delmont, Paris, France, 1856.

Dixon, W. J. ed., BMO Biomedical Computer Programs, 773 p., Univ. of Calif. Press, 1974.

Draper, N. R. and H. Smith, Applied Regression Analysis, Wiley, New York, 407 p., 1966.

Ewing, J., M. Ewing, T. Aitken and W. J. Ludwig, North Pacific sediment layers measured by seismic profiling, American Geophysical Union, Geophysical Monograph 12, 147-173, 1968.

Galson, D. A., An investigation of the thermal structure in the vicinity of IPOD sites 417 and 418, M. Sci. Thesis, Massachusetts Institute of Technology, 155p., 1979.

Green K. E., R. P. Von Herzen and D. L. Williams, The Galapagos Spreading Center at 86oW: a detailed geothermal field study, 1980.

Herron, E. M., Sea-floor spreading and the Cenezoic history of the east-central Pacific, Geol. Soc. America Bull., 83, 2119-2136, 1972.

Horn, D. R., B. M. Horn and M. N. Delach, Ocean manganese nodules metal values and mining sites, Tech. Report No. 4, NSF GX 33616, 57 p., IDOE, NSF, Washington, D.C., 1973.

Jessop, A. M., M. A. Hobart and J. G. Sclater, World wide compilation of heat flow data, Geothermal Ser., no. 5, Department of Energy, Mines and Resources, Ont., 1976.

Lachenbruch, A H. and B. V. Marshall, Heat flow through the Arctic Ocean floor: the Canada Basin-Alpha Rise boundary, J. Geophys. Res., 71, 1223-1248, 1966.

Langseth, M. G. and B. M. Herman, Heat transfer in the oceanic crust of the Brazil Basin, submitted to J. Geophys. Res.

Langseth, M. G., P. J. Grim and M. Ewing, Heat-flow measurements in the East Pacific Ocean, J. Geophys. Res., 70, 367-380, 1965.

Langseth, M. G., I. Malone And D. Berger, Sea floor geothermal measurements from Vema cruise 24, Columbia Univ. Tech Rept. 3-CU-3-71, NTIS AD729682, 452pp., 1971.

Lister, C. R. B., Heat flow west of the Juan de Fuca Ridge, J. Geophys. Res., 75, 2648, 1970.

Lister, C. R. B., On the thermal balance of a mid-ocean ridge, Geophys. J. R. astr. Soc., 26, 515-535, 1972.

Lisitzen, A. P., Sedimentation in the world ocean, Special Publication No. 17, Soc. Eco. Paleontologists and Mineralogists, Tulsa, OK, 218 p., 1972.

Lubimova E. A., R. P. Von Herzen and G. B. Udintsev, On heat transfer through the ocean floor, in Terrestrial Heat Flow, Lee, W.H.K., ed., Amer. Geophys. Union, Mono. 8, 78-86, 1965.

McCoy, F. W. and R. P. Von Herzen, Deep-sea corehead camera photography and piston coring, Deep-Sea Research, 18, 361-373, 1971.

Parsons, B. A. and J. G. Sclater, An analysis of the variation of ocean floor bathymetry and heat flow with age, J. Geophys. Res., 82, 803-827, 1977.

Ratcliffe, E. H., The thermal conductivities of ocean sediments, J. Geophys. Res., 65, 1535-1541, 1960.

Sclater, J. G., and S. P. Miller, A machine method for computing the effect of a two-layered conductivity structure, Tech. Memo. 198, Mar. Phys. Lab., Scripps Inst. of Oceanogr., La Jolla, CA, 1969.

Sclater, J. G., R. N. Anderson and M. L. Bell, Elevation of ridges and evolution of the central eastern Pacific, J. Geophys. Res., 76, 7888-7915, 1971.

Sclater, J. G. and J. Crowe, A heat flow survey at anomaly 13 on the Reykjanes Ridge: a critical test of the relation between heat flow and age, J. Geophys. Res., 84, 1593-1602, 1979.

Sclater, J. G., J. Crowe and R. N. Anderson, On the reliability of oceanic heat flow averages, J. Geophys. Res., 81, 2997-3006, 1976.

Sclater, J. G., C. Jaupart and D. A. Galson, The heat flow through oceanic and continental crust and the heat loss of the Earth, Rev. Geophys. and Space Phys., 18 (1980) 269-311 .

Skempton, A. W., The consolidation of clays by gravitational compaction, Q. Jl. geol. Soc. Lond., 125, 373-411, 1970.

Sleep, N. H. and T. J. Wolery, Egress of hot water from midocean ridge hydrothermal systems: some thermal constraints, J. Geophys. Res., 83, 5913-5922, 1978.

Spiess, F. N., K. C. Macdonald, T. Atwater, R. Ballard, A. Carranza, D. Cordoba, C. Cox, V. M. Diaz Garcia, J. Francheteau, J. Guerrero, J. Hawkins, R. Haymon, R. Hessler, T. Juteau, M. Kastner, R. Lawson, B. Luyendyk, J. D. Macdougall, S. Miller, W. Normark, J. Orcutt and C. Ranjin, East Pacific Rise: hot springs and geophysical experiments, Science, 207, 1421, 1980.

Talwani, M., C. C. Windisch and M. G. Langseth, Reykjanes Ridge Crest: a detailed geophysical study, J. Geophys. Res., 76, 473-517, 1971.

Terzaghi, K., Tne shearing resistance of saturated soils, Proc. 1st Int. Conf. on Soil Mech., Harvard, 1, 54-56, 1936.

Tracy, J. I., G. D. Sutton, W. D.Nesteroff, J. S. Galenhouse, C. C. von der Borch, T. C. Moore, Jr., U. Z. Bilal-uh-haq and L. P. Beckmann, Leg 8 summary, in Tracy, J. I. and G. D. Sutton., eds., Initial Reports of the Deep Sea Drilling Project, Washington, D.C., U.S. Govt. Printing Office, 8, 17-42, 1971.

Vacquier, V., J. G. Sclater And C. E. Corry, Studies of the thermal state of the Earth, The 21st Paper - Heat Flow, Eastern Pacific, Bull. Earthq. Res. Inst. Tokyo Univ., 45, 375-393, 1967.

van Andel, T. H., G. R. Heath and T. C. Moore, Jr., Cenozoic history and paleoceanography of the central equatorial Pacific Ocean, Geol. Soc. Am. Memoir, 143, 134 p., 1975.

Von Herzen, R. P. and A. E. Maxwell, The measurement of thermal conductivity of deep-sea sediments by a needle-probe method, J. Geophys. Res., 64, 1557-1563, 1959.

Von Herzen, R. P., J. Crowe and K. E. Green, Fluid convection in Eastern Pacific Ocean crust, EOS, 60, 382, 1979.

Von Herzen, R. P., And R. N. Anderson, Implications of heat flow and bottom water temperature in the eastern equatorial Pacific, Geophys. J. R. Astr. Soc., 26, 427-458, 1972.

Von Herzen, R. P. And S. Uyeda, Heat flow through the Eastern Pacific Ocean floor, J. Geophys. Res., 68, 4219-4250, 1963.

Williams, D. L., K. E. Green, T. H. van Andel, R. P. Von Herzen, J. R. Dymond and K. Crane, The hydrothermal mounds of the Galapagos Rift: observations with DSRV Alvin and detailed heat flow studies, J. Geophys. Res., 84, 7467-7484, 1979.

Winterer, E. L., Anomalies in the tectonic evolution of the Pacific, in: The Geophysics of the Pacific Ocean Basin and its Margin, eds. Sutton, G. H., M. H. Manghnani and R. Moberly, American Geophysical Union, Mono. 19, 269-278, 1976.

APPENDIX I

Description of Least-Squares Non-linear Iteration Program

Equation 5 was fit to the observed temperature versus depth data using a non-linear multivariate regression program (Dixon, 1974). The model can be formulated as follows (Draper and Smith, 1966):

$$d = f(\xi, \underline{P}) + e \tag{A1}$$

where d = an observed temperature

ξ = the depth of this measurement

$\underline{P} = (P_1, P_2, \ldots, P_p)$ the parameters of the model

e = residual of the temperature observation.

For N observations we have N equations

$$d_i = f_i(\underline{P}) + e_i \quad i = 1, N \tag{A2}$$

To find an estimate $\hat{P}$ of $\underline{P}$, equation A2 must be linearized. Carrying out a Taylor series approximation about an initial guess $\underline{P}^0$ we have

$$d_i = f_i(\underline{P}^0) + \frac{df_i}{dP_j}\bigg|_{\underline{P}^0} (\underline{P} - \underline{P}^0) + \ldots + e_i \tag{A3}$$

where

$$\frac{df_i}{dP_j} = \begin{bmatrix} \dfrac{df_1}{dP_1} & \cdots & \dfrac{df_1}{dP_n} \\ \vdots & & \vdots \\ \dfrac{df_N}{dP_1} & \cdots & \dfrac{df_N}{dP_n} \end{bmatrix}$$

$$(\underline{P} - \underline{P}^0) = \begin{bmatrix} P_1 & P_1{}^0 \\ P_2 & - & P_2{}^0 \\ & \vdots & \\ P_n & - & P_n{}^0 \end{bmatrix}$$

In matrix form we have:

$$d_i - d_i{}^0 = \left.\frac{df_i}{dP_j}\right|_{\underline{P}^0} (P - P^0) + e_i \qquad (A4)$$

$$(N \times 1) \qquad (N \times M) \ (N \times 1) \qquad (N \times 1)$$

where $d_i = f_i(\underline{P}^0)$. We can rewrite A4 as:

$$\Delta\underline{d} = A \cdot \Delta\underline{P} + \underline{e} \qquad (A5)$$

where $\Delta\underline{d}$ is the difference between the observed data and the values the initial guess would produce, $\Delta\underline{P}$ is the difference between real $\underline{P}$ and the initial guess and $A = df_i/dP_j$.

When the errors of the observations can be estimated, each equation can be weighted be dividing it by the standard deviation of the error.

If there are more equations than parameters (N > P) the least squares estimate $\Delta\hat{\underline{P}}$ of $\Delta\underline{P}$ is

$$\Delta \hat{\underline{P}} = (A^T \cdot A)^{-1} \cdot A^T \cdot \Delta d \tag{A6}$$

Equation A6 has the property that the sum of the squared residual is minimized.

$$\sum_{i=1}^{N} e_i = \sum_{i=1}^{N} (d_i - \sum_{j=1}^{M} A_{ij} P_j)^2 = minimum \tag{A7}$$

The initial guess can be improved by correcting it with ΔP obtained from the least squares process

$$\hat{\underline{P}}^1 = \hat{\underline{P}}^0 + \Delta \underline{P} \tag{A8}$$

Using $\hat{\underline{P}}^1$ as the new initial guess we can repeat the calculations in equations A2 through A7. The process converges, if, at each iteration, the new set of parameters, $\hat{\underline{P}}^k$ can improve the fit of the model. The model is considered to have converged when

$$\left| \frac{\alpha^{k+1} - \alpha^k}{\alpha^{j+1}} \right| < C \tag{A9}$$

where $\alpha^k = \sum_i (\Delta d_i^k - \sum_j A_{ij}^k \cdot \Delta P_j^k)^2$ and C is a specified convergence criterion.

APPENDIX II

Evaluation of Resolution and Sensitivity

of the Non-Linear Estimator

It is important to establish the ranges of parameters for which

meaningful results can be obtained using the procedure discussed in Appendix

I. We wish to determine the suceptibility of our results to random and

systematic errors in the data and also to establish the accuracies necessary

to obtain useful results. Major objectives of the study are to establish:

(1) the minimum and maximum parameters that can be resolved within

accuracy of the data

(2) the effect of one or more individual poor quality data points within

an otherwise high quality set of observations

(3) the identification of data (individual or collective) that are of

questionable reliability

(4) the ranges of parameters that fit the observed data adequately.

In order to accomplish the above the response of our parameter estimator

to artificially generated data sets of known precision was studied. For a

given heat flow and mass flux, temperature profiles consisting of seven

discrete observations over 11.5 meters were generated using the thermal

conductivity structure of station 15. For a more general study of this

problem, the spacing of these temperature observations should be varied. To

each value, normally distributed random noise of a chosen standard deviation

was added. The response of the nonlinear estimator to fifty of these

artificial data sets was compiled and a mean value and standard deviation for

the resulting parameters was computed.

In Figure 38 are examples of the response of the nonlinear estimator to four such data sets where Q was either 0.5, or 2.0 HFU, W was either 10^{-7} or 10^{-6} cm/sec, b was equal to zero and the standard deviation of the random noise ranged from 0.0001°C to 0.1°C. For data accurate to 0.001°C the results are excellent. For errors greater than 0.001°C the response of the estimator begins to degenerates, especially for low values of both Q and W. Values of W equal to 10^{-7} cm/sec could not be distinguished from W = 0 for errors of standard deviation of 0.01°C, however, the estimates of Q were quite satisfactory. At levels of noise greater than 0.01°C, the estimation of b is very poor.

It appears that as Q and W increase, the resolution of the estimator increases. The minimum values of the parameters distinguishable at the level of accuracy of our data, is a function of both Q and W. Figure 39 contrasts the estimates of Q, W and B obtained from (1) a 1 HFU conductive temperature profile, and (2) a convective profile corresponding to a heat flow of 1 HFU and mass flux equal to 10^{-7} cm/sec, both perturbed in the manner previously discussed. The comparison of these results shows that the estimator has trouble resolving flows less than 10^{-7} cm/sec from the linear case.

The data used in Figures 38 and 39 all consist of seven discrete values, which corresponds to the data collected during KNORR 73-4. On PLEIADES III, only five thermistors were used. The problem is poorly constrained for both cruises as the degrees of freedom are 4 and 2 repectively. The effect of the number of observations on the response of the estimator is very important. Results obtained from a profile consisting of five temperature values spaced

Figure 38.   Error estimation of heat flow (Q), volume flux (W) and penetration depth (b) as a function of temperature errors based on a numerical scheme described in Appendix I.   The errors resulting from normally distributed errors of 10^{-4}, 10^{-3}, 10^{-2} and 10^{-1} ^{o}C for heat flows of 0.5 and 2.0 HFU and volume fluxes of 10^{-7} and 10^{-6} cm/sec are contrasted.   Note the differing vertical scales for Q and W between the upper and lower graphs and the decreasing resolution of the non-linear estimator as heat flow decreases.

2 HFU
10^{-7} cm/sec

2 HFU
10^{-6} cm/sec

0.5 HFU
10^{-7} cm/sec

0.5 HFU
10^{-6} cm/sec
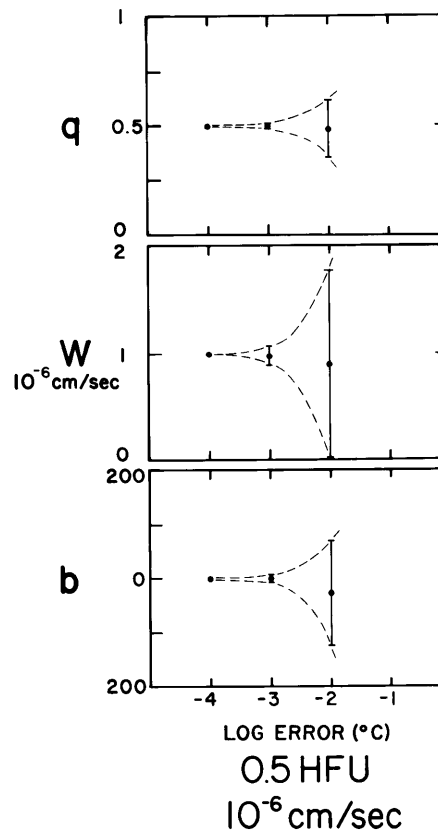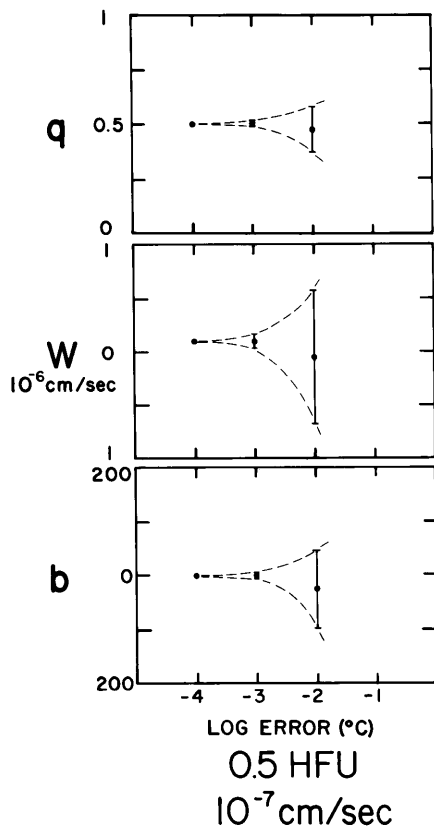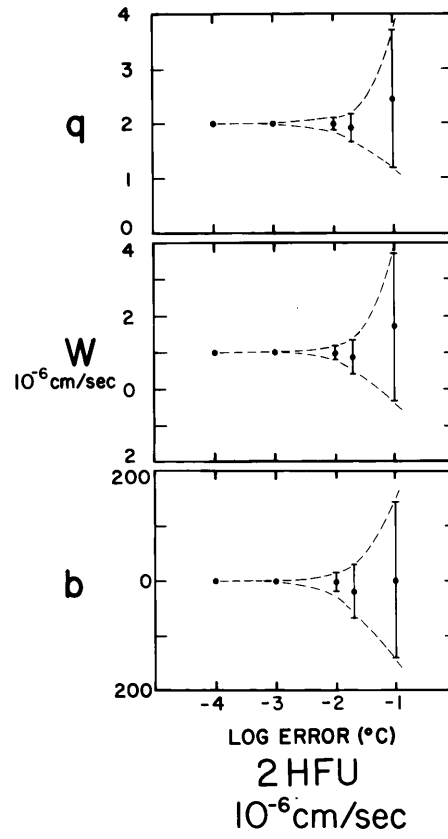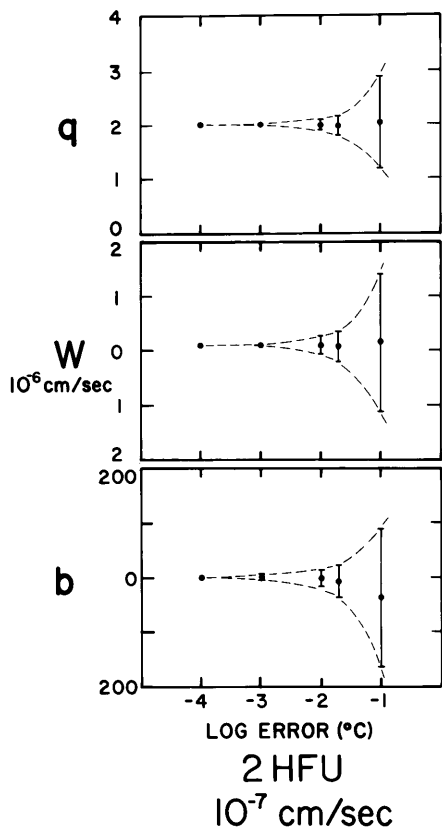
Figure 39. Comparison of the errors resulting for a volume flux of 10^{-7} cm/sec and the case of no flow at a heat flux of 1.0 heat flow unit. It appears that the non-linear estimator is not capable of distinguishing flows of less than 10^{-7} cm/sec.

I HFU
NO FLOW
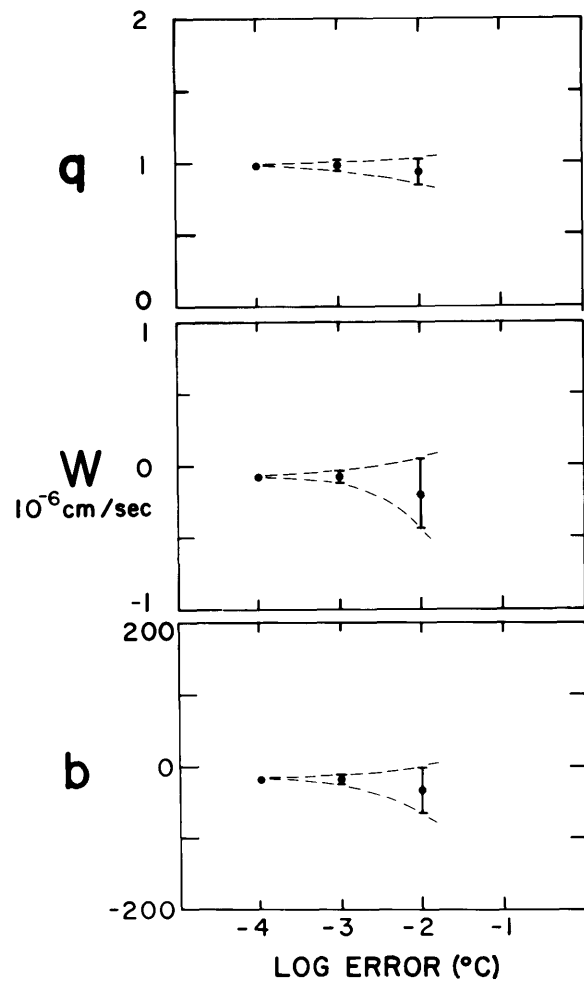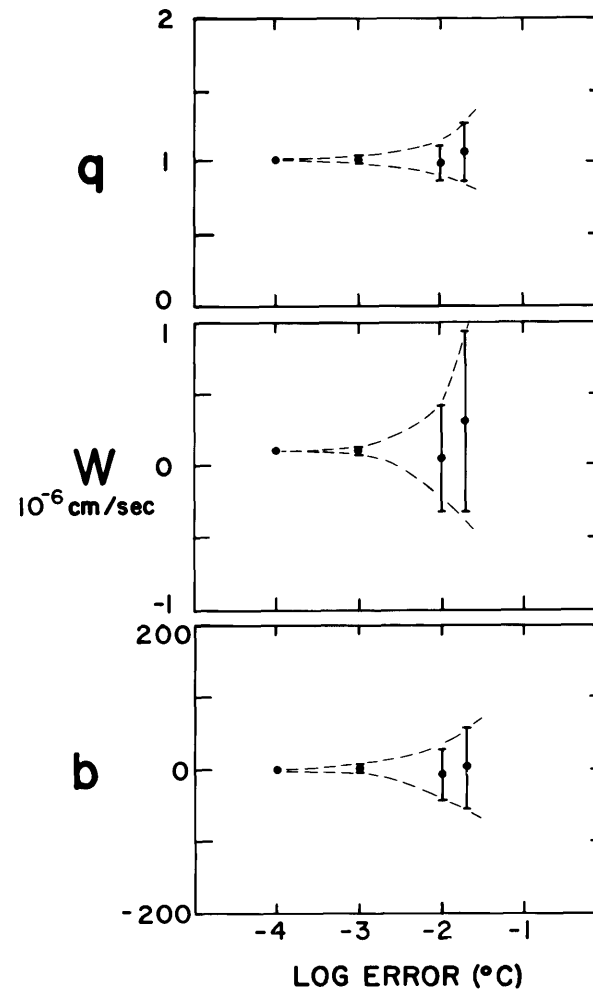
I HFU
10^{-7} cm/sec

over 11.5 meters for 1.0 HFU and 1×10^{-6} cm/sec showed that up to a certain magnitude of noise, the case with five observations is as sensitive as the seven observation case. However, a point is reached where resolution is lost quickly. From the reduction of the actual data, we found that for many stations where less than six thermistors define the temperature profile, the results were very sensitive to small perturbations in the observations.

The set of residuals (observed minus predicted) associated with the reduction of real data sometimes include one or two that are significantly large. It is apparent that the effect of gross errors in one or two observations can be very complicated and significant. To get a feeling for this type of error, one temperature value was perturbed with noise of $0.01^{\circ}C$ while the six other observations were held at constant accuracy of 10^{-5} $^{\circ}C$ for Q and W equal to 1 HFU and 10^{-6} cm/sec respectively. We found that for W the effect of perturbing one thermistor is very similar to that of perturbing all seven. Also it is interesting to see that some parameters are more sensitive to inaccuracies at a given depth than others. For example, B appears to be more sensitive to errors in shallow observations, while W is more sensitive to errors in deeper observations.

The minimum magnitude of the residuals of the real data is about $\pm 0.002^{\circ}C$. The accuracy of our data collection system, (thermistor calibrations and digital recording system) is assumed to be 1 millidegree. The accuracy of our data with respect to the true equilibrium temperature value has been estimated as between 1 and 30 millidegrees. In order to incorporate these error estimates, a weight, w, was assigned to each temperature observation. The weights are defined as the inverse of the

standard deviation of the measurements, with the assigned errors interpreted as a rough estimate of the standard deviation of the errors. The correlation between the residuals and the assigned errors was improved by this choice of weighting.

The residuals of some of our stations are on the $\pm 0.01^{\circ}C$ level and must be accounted for. Errors due to poorly defined conductivity structure over the depth of our measurements cannot explain these stations. The effect of using a varying thermal conductivity structure instead of a uniform structure equal to the harmonic mean conductivity did not result in significant changes in the residuals. However, changes in W of up to 50% occurred in some instances. In a series of several consecutive measurements, variation in the nature of the residuals has been observed suggesting that physical processes associated with the actual deployment of the experiment may be a factor.

CHAPTER THREE

Permeability Measurements of Equatorial Pacific Carbonate

Oozes Using A Direct Measurement Back-Pressured Technique

by

John Crowe

Dept. of Geology and Geophysics
Woods Hole Oceanographic Institution, Woods Hole, MA 02543

Dept. of Earth and Planetary Sciences
Massachusetts Institute of Technology, Cambridge, MA 02139

and

Armand J. Silva

Dept. of Ocean and Civil Engineering
University of Rhode Island, Kingston, RI 02881

ABSTRACT:

Permeabilities of deep-sea sediments from the North and Equatorial Pacific Ocean have been measured using a direct measurement technique under conditions of complete pore fluid saturation and one-dimensional consolidation. The complete saturation of pore fluid is assured by the application of back-pressure (hydrostatic pressure). The use of incrementally increasing vertical stress enables the determination of permeability as a function of void ratio at different stages of consolidation while also guaranteeing the stability of the sediment microstructure. The range in permeability measured for carbonate-rich biogenic sediments from the equatorial Pacific was 7.0×10^{-7} to 7.0×10^{-6} cm/sec for a void ratio range of 1.95 to 5.4. Previously reported permeability measurements of smectite and illite from the North Pacific are also summarized. The permeability of illite ranged from 1.5×10^{-8} to 1.5×10^{-6} cm/sec over void ratios of 1.3 to 4.4 while for smectite the range was from 3.5×10^{-9} to 9.0×10^{-7} cm/sec over void ratios of 2.6 to 5.6. The range in vertical stress applied to the specimens during the direct permeability measurements was from the in-situ stress of the specimen, order of magnitude 0.1 kg/cm^2, to values estimated for sediment overburdens of 150 to 200 meters, about 10 kg/cm^2. The pore structure of the biogenic sediments was studied using scanning electron microsope (SEM) photographs. Elongated pores, less than two microns in width, situated within flocculated structures of clay and silt sized particles appear to control permeability. The effect of applying vertical stresses estimated for 200 meters of overburden is to partially close these pores, reducing permeability by about 50%. The necessity of using both vertical stress

greater than or equal to in-situ and back-pressures of around 10 kg/cm^2 during these measurements was evaluated, as they represent a substantial increase in the complexity of an otherwise simple experiment. The results of this investigation suggested that tests run without these precautions may be in error by several orders of magnitude.

INTRODUCTION:

The need for accurate permeability measurements of deep-sea sediment has arisen in several phases of oceanographic research. Two important examples are the sub-seabed radioactive waste disposal program (D. Anderson, 1979) and the study of oceanic heat transport mechanisms (R. Anderson et al., 1977). Studies for the safe disposal of waste materials within the seabed requires a thorough understanding of the permeability characteristics of the sediment column both in the environment and as altered by the implaced material. The results of several oceanic heat flow studies (R. Anderson et al, 1979; Langseth and Herman, in press; Crowe et al., in preparation) have suggested the transport of heat through the oceanic sediment layer by the mass movement of fluid through the pores. To analyze this heat flow problem, a quantitative model of permeability throughout the sediment column is necessary.

Direct permeability measurements are usually based on Darcy's law (equation 1) involving the observation of a permeant volume flux through a porous medium under a pressure gradient. Other indirect methods infer permeability from the observation of processes such as consolidation, which are controlled by permeability (Mitchell, 1976). Simple direct permeability measurements can be made shipboard or in the lab applying falling head and

constant head techniques on samples obtained from sediment. These methods assume that the effects of incomplete saturation of pore fluid and alterations of the sediment structure by the applied pressure gradients are negligable. A number of results determined this manner have been reported in the literature (Pearson and Lister, 1973; Abbott et al., 1979, in press); however, these may be susceptible to several inherent errors. Possible contributions to these errors include (1) sample disturbance associated with the procedures of acquiring the core and selecting from it laboratory specimens, (2) the effects of environmental differences between laboratory and in-situ conditions including the effects of high ambient pressures and incomplete saturation and (3) systematic bias introduced by the laboratory methods used.

We report new permeability values for carbonate-rich biogenic sediments from the Equatorial Pacific Ocean and summarize the results of previously reported values for clay sediments from the North Pacific Ocean. These measurements were conducted under conditions of complete fluid saturation and in-situ vertical stress. The necessity of guaranteeing both the complete saturation of pore fluids by the use of back-pressure and the stability of the microstructure by the application of vertical stress is also discussed.

RELATIONSHIP BETWEEN PERMEABILITY AND THE DEGREE OF SATURATION:

Darcy's law (Darcy, 1856), valid for the steady flow of viscous, incompressible and chemically inactive fluids through saturated, homogeneous, isotropic and geometrically stable porous media at low Reynolds number and constant temperature (Irmay, 1954), is given by

$$\bar{v} = -(\frac{K}{\mu}) \nabla P = -(\frac{k}{\gamma}) \nabla P \qquad (1)$$

where $\bar{v}$ is the vector fluid velocity driven by pressure gradient ∇P, K is specific permeability (dimension L^2), k is hydraulic conductivity (dimension $L\ t^{-1}$), μ is dynamic viscosity (centipoise) and γ is the unit weight of fluid. Equation 1 can be considered as the macroscopic equivalent of the Navier-Stokes solution for a matrix of interconnected pores (Muskat and Meres, 1936). The physical properties of the porous media are completely described by K.

The case of a heterogeneous permeant is more complicated. Muskat and Meres proposed that for a heterogeneous permeant, a porous media is characterized by the variation of both liquid and free gas permeabilities as a function of the degree of saturation, S. The degree of saturation is defined as the ratio of partial volume of fluid to the volume of voids in a unit volume of soil. For a hetergeneous fluid system, K is different for the gas and liquid phases. A two phase permeant system is defined as consisting of two immiscible fluids, referred to as the wetting and non-wetting phases. In such a system it is convenient to define relative permeability as the ratio of the effective permeability of a phase to its permeability at a degree of saturation of 1.0 (Brooks and Corey, 1966). Therefore, for a given phase, relative permeability, K_r, is defined as

$$K_r = \frac{K_e}{K} \qquad (2)$$

where K is the value of permeability for S = 1.0 and K_e is the permeability pertaining to a particular value of S. Laboratory studies of K_r as a

function of S suggest that for a gas-liquid system initally at S = 0, a critical value of saturation must be exceeded before measureable liquid flow occurs. This threshold saturation, S_0, has been associated with the trapping of some liquid in the sharp angles occurring between grains, which remain stagnant (Irmay, 1954). From this concept, effective saturation, S_e, is defined as

$$S_e = (\frac{S - S_0}{1 - S_0})$$ (3)

Several models based on Poiseuille's law for flow in cylindrical capilillaries have been proposed to explain experimental K_r versus S_e data (referred to as K_r-S_e data). These results form a power function

$$K_r = S_e^n$$ (4)

The models of Brownescombe et al. (1950) and Yuster (1954) suggested a value of n equal to 2.0 while Averjanov (1950) calculated a value of 3.5. By deriving the Kozeny model (Carman, 1953) for the case of partial saturation, Irmay (1950) also arrived at a value for n of 3.5.

Mualem (1978) summarized these models and reviewed the published experimental data representing a wide variety of soil types. In general no single K_r-S_e relationship was found to be valid for all types of soils. Although equation 4 has been derived theoretically, experimental verification has been limited to sand sized particles. Mualem assumed equation 4 to be a valid description of the partially saturated system and determined n for the published data. The calculated values of n were in the range 2.5 to 24.5,

with a general trend of n increasing as grain size decreased. The experimental results pertaining to sand sized grains were consistent with the predicted values from the models (n of 2.0 to 3.5). However, for soils of finer grain size the value of n generally exceeds the theoretical values by a significant amount. In summary the theoretical models based on Poiseuille's law appear reasonably successful in predicting the behavior of cohesionless soils, but do not appear valid for clays.

At the microscopic level, the dynamics of fluid flow in a partially saturated system were discussed by Wyckoff and Botset (1936). They considered the "Jamin effect" which is the situation where gas bubbles are trapped by the presence of a constriction or an abrupt change in pore diameter, therefore impeding flow through the non-uniform section until a critical force is exerted. Such a system will behave as if some capillaries are obstructed with a reduction of the flow. The Kozeny-Carman equation (Carman, 1956) is an attempt to incorporate the effects on fluid flow of pore shape, pore volume, tortuosity of the fluid path and variation in particle specific surface:

$$K = \frac{1}{k_0 T^2 S_0^2} \frac{e^3}{(1 + e)} \tag{5}$$

where k_0 is a pore shape factor, T is a tortuosity factor and S_0 is the specific surface area defined as particle surface area per unit volume. For this model it is assumed that particles are approximately equidimensional, uniform, larger than one micron and the flow is laminar. Equation 5 is successful for analyzing many sands, however, for clays it is not adequate due to the tendency of fine grained soils to form flocculated structures (Mitchell, 1976).

SATURATION OF LABORATORY SAMPLES USING BACK-PRESSURE (HYDROSTATIC PRESSURE):

When a soil sample is removed from in-situ conditions, pore water pressure is reduced from in-situ to atmospheric or less depending on grain-size. The pore water pressure of a coarse grained soil will be atmospheric while a fine-grained soil will tend to expand upon the release of the in-situ intergranular pressures resulting in the developement of capillary forces to resist the expansion and less than atmospheric pore pressure (Lowe and Johnson, 1960).

Complete saturation of laboratory samples can be obtained by application of hydrostatic back-pressure to the pore fluid. If back-pressure is applied such that consolidation does not occur, the decrease of the gas volume within the pore space is governed by two processes. One is the influx of fluid necessary to compensate for the compression of pore gasses (Boyle's law), the rate being controlled by sediment permeability. The second is the dissolution of gas into the pore fluid (Henry's law) controlled by diffusivity (Lowe and Johnson, 1960; Black and Lee, 1973). As pore pressure is increased the amount of gas that can be dissolved is increased according to Henry's Law

$$[C] = H P \qquad (6)$$

where P is pressure, [C] is the concentration of gas in solution and H is Henry's coefficient of soluability. The use of deaired water increases the amount of gas that can be dissolved.

In the process of applying back-pressure, it is desirable that the pore structure not be deformed. The slow build-up of pore pressure allows water to displace the volume formerly occupied by dissolved gas without altering the

original soil structure. Lowe and Johnson (1960) calculated the change in pore pressure, dP, independent of soil type, necessary to increase the degree of saturation without altering the soil volume as

$$dP = P_i \left[\frac{1 - S_i(1-H)}{1 - S_f(1-H)} - 1 \right]$$
(7)

where P_i is the initial pressure and S_i and S_f are the initial and final degrees of saturation. For complete saturation, equation 7 reduces to

$$dP_{100\%} = 49P_i (1 - S_i)$$
(8)

(Black and Lee, 1973).

Lee and Black (1972) experimentally found that small air bubbles (diameter less than 2 mm) suspended in a container of water under hydrostatic pressures in the range 20-80 psi required up to several hours to dissolve. The same sized bubble located in a small diameter plastic tube required several days to dissolve, since the freedom of the air molecules was reduced. The time necessary to completely dissolve a bubble, where the bubble is suspended in a large body of water was found theoretically and experimentally by Lee and Black (1972) to be

$$t = (\frac{R_i^2}{K_t})$$
(9)

where R_i is the initial radius and K_t is a constant that depends on the

physical properties of the system (order of 10^{-7} cm^2/sec). For a bubble constricted within a tube, the time required for complete dissolution is

$$t = (\frac{V_i}{K_t})^2 \qquad (10)$$

where V_i is the initial volume of the bubble. The theoretical and experimental evidence suggested that the time necessary for complete saturation is controlled by the time required for the diffusion of pore air into the pore water rather than the permeability effect involved in transmitting and distributing water into and throughout the sample.

Lowe and Johnson (1960) achieved 99% saturation in a silty sand using back-pressures between 50-100 psi. For fine grained clay samples higher pressures were necessary, and they discussed an experiment where 200 psi appeared to be sufficient. Although it is desirable to conduct tests at 100% saturation, due to the time necessary to completely dissolve large bubbles, errors obtained at 99% saturation are probably acceptible and insignificant.

CONSOLIDATION OF SEDIMENTS:

Consolidation is the decrease in void ratio of a soil due to expulsion of pore fluid resulting from an increase in effective stress. In order to study permeability as a function of void ratio, samples are consolidated in conjunction with permeability testing. Void ratio, e, is the ratio of void volume to solid volume. Effective stress, $\bar{\sigma}$, is defined as

$$\bar{\sigma} = \sigma - u \qquad (11)$$

where σ is the total stress applied to the soil and u is the pore pressure (Terzaghi, 1936).

Figure 1 is a simplified diagram of the relationships between effective stress and void ratio for both in-situ and laboratory conditions. As a volume of sediment is deposited and buried, the change in e due to increasing follows the field (or virgin) compression curve. The maximum preconsolidation stress, $\bar{\sigma}_c$, is the greatest effective stress ever experienced by a sample with a corresponding void ratio. The field compression curve defines the void ratios at former values of effective stress and the virgin curve is an extension at void ratios that would occur for effective stresses exceeding the maximum preconsolidation stress. For most geological situations, $\bar{\sigma}_c$ is the in-situ stress. As a core is removed from in-situ conditions, this stress is relieved resulting in the swelling of the specimen, shown in Figure 1 as the sampling rebound curve. In the laboratory a sample is initially in a state where effective stress is zero and void ratio exceed in-situ.

Consolidation behavior can be studied by reloading of a sample in the laboratory. Loads are applied in such a way as to allow excess pore pressures to dissipate before the next load is applied and therefore the applied stress at the end of load cycles is the effective stress. The consolidation that occurs while the excess pore pressure generated by the applied incremental load dissipates is know as primary consolidation. Another form of consolidation, secondary consolidation, occurs in response to the constant vertical stress even after the excess pore pressures have dissipated. This gradual readjustment of the sediment fabric takes place over long time spans and the compression is usually much less than the primary consolidation.

Figure 1. A simplifed diagram of the relationship between void ratio and vertical stress.
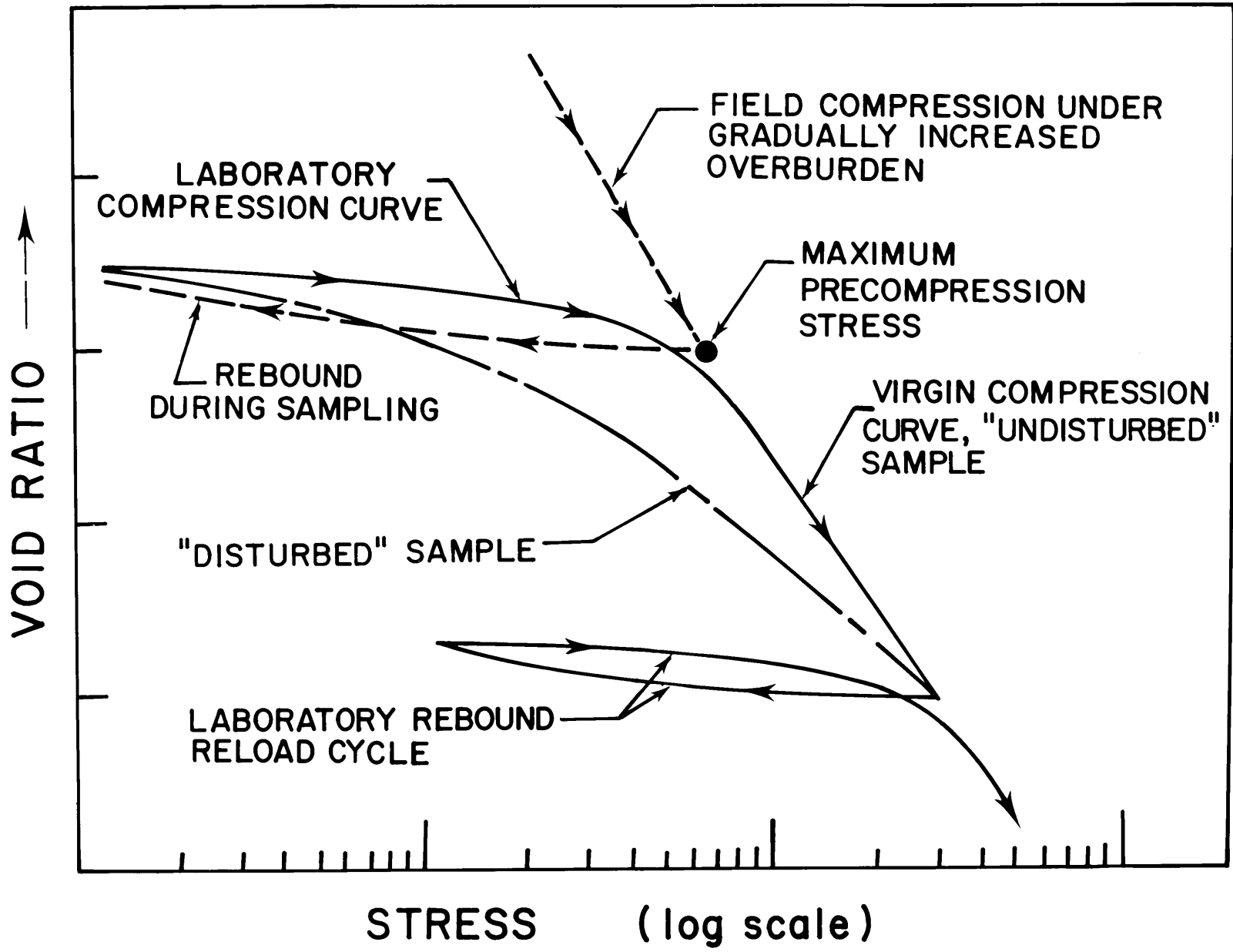
Initial laboratory loading does not appreciably change the void ratio of the specimen until the maximum preconsolidation stress is approached. In the vicinity of this stress, void ratio decreases more rapidly until the slope of the e log σ curve approaches a constant (the virgin curve). This transition from the laboratory rebound to the virgin curve reflects the maximum proconsolidation stress and is a property of the specimen. Several methods of estimating $\bar{\sigma}_c$ based on this transition have been proposed for samples of negligible disturbance (Casagrande, 1936; Jambu, 1965). The sharpness of the break in the e log σ curve is considered as a measure of sample disturbance. Studies show that badly disturbed samples have gradual breaks. The laboratory release and reloading of vertical stress mimics the actual stress release that occurs during coring and the comparison of the laboratory compression curve with the laboratory rebound-reload cycle (Figure 1) provide a basis of the determination of sample disturbance (Silva, 1974; Schmertmann, 1955).

In order to conduct permeability measurements at in-situ void ratio and effective stress, the sample must be reloaded to the maximum precompression stress. The results of direct permeability measurements conducted under conditions of negligible vertical stress may be susceptible to errors associated with the creation of flow channels through zones of weakness within the microstructure of the specimen or the venting of permeant along the boundary of the specimen and its confining ring. This problem can be avoided by loading the sample to the maximum precompression stress and using low hydraulic pressures.

EXPERIMENTAL PROCEDURES AND RESULTS:

A back-pressured consolidation system (Figure 2), modified to allow the direct measurement of fine-grained marine sediment permeability, was used in this study. This apparatus and the laboratory procedures used are described by Silva et al. (1980). Back-pressures of up to 450 psi and uni-axial stresses comparable to several hundred meters of sediment overburden are possible. The direct measurement of permeability can be conducted using either constant or falling head techniques with the flow of fresh or salt water permeants in either axial direction and gradients as low as 2.0.

In sampling the cores, a standard procedure was followed. Samples were selected at the center of core cross-section since the greatest degree of disturbance in a core occurs near the core liner wall. A stainless steel cylinder was inserted along the axis of the core using a piston-type device that aided in minimizing disturbance due to wall friction. These cylinders were carefully removed from the core, encased between plexiglass plates, sealed in wax, and stored in seawater at $4^{o}C$ until tested. Comparison of water contents measured during sampling and later in the laboratory indicated no measureable loss of water during storage.

Our experimental study can be divided into two parts. The aim of the first was to determine the permeability characteristics of biogenic oozes from the equatorial Pacific Ocean and to compare these results with previously determined permeability characteristics of North Pacific red clay. The second part investigated the necessity of both the application of in-situ vertical stress and the ensuring of complete pore water saturation.

Figure 2. Diagram of back-pressured consolidation unit (Silva et al., 1980).

MODIFIED ANTEUS BACK-PRESSURED CONSOLIDATION-PERMEABILITY UNIT

Anteus
Loading
Unit

Sliding
Column
Load
Reservoir

B

Sample

Back
Pressure
Reservoir

A

A

Volume Change
Burets
(Silicone Oil)

(Sea Water)

B

Porewater
Valve
B

Sliding
Column
Permea-
bility

Reservoir
(Silicone Oil)

B

Quick-Connect
Pressure
Readout

Pressure
Regulator
(0-500 psi)

B

Valve Types

A-Ball Valve (No-Volume Change)

B-Shut-Off Needle Valve
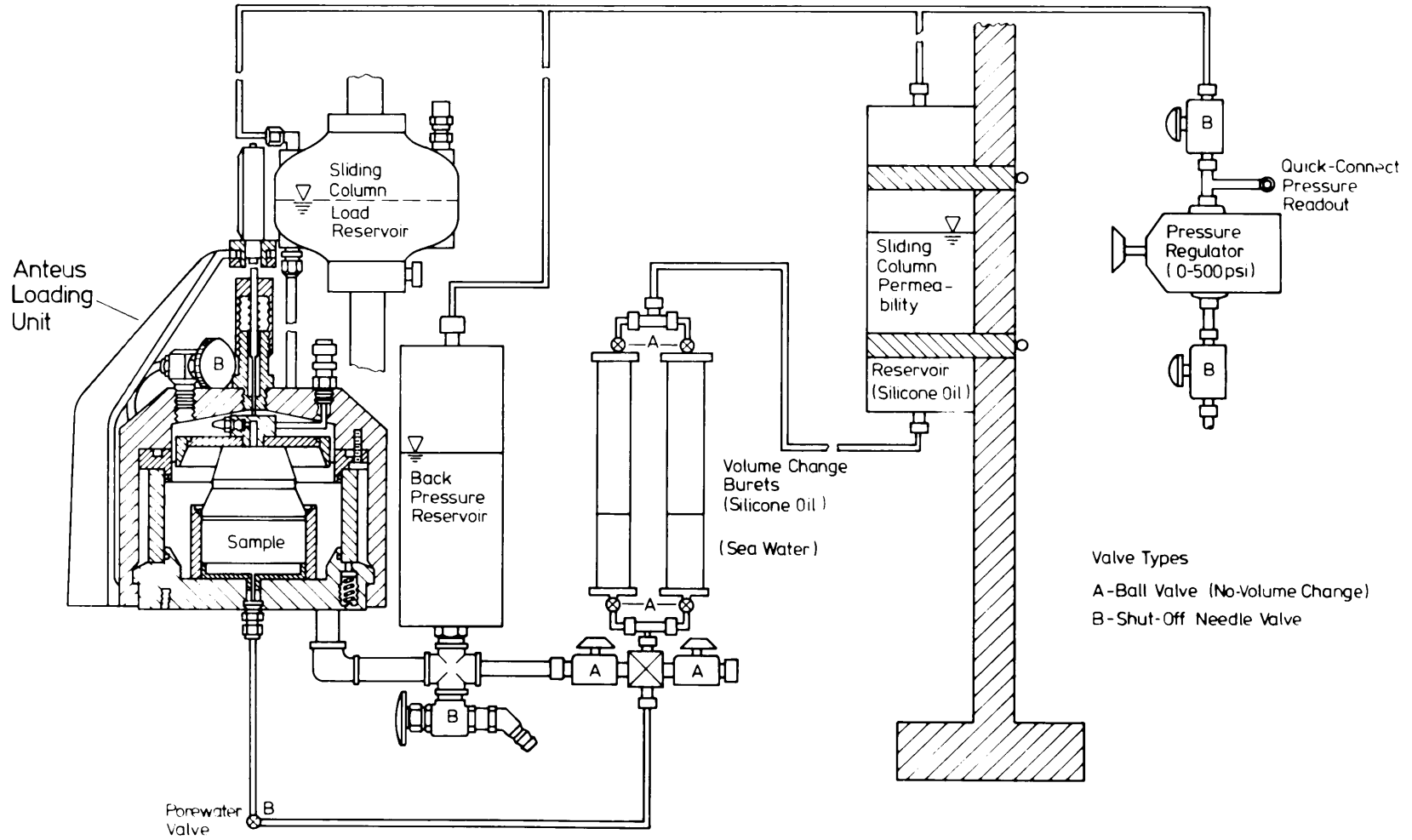
(A) Determination of Permeability Characteristics

For this study samples were placed in the consolidation system (Figure 2), with a slight stress applied to the piston that seats on top of the specimen to prevent further swelling. The entire system was filled with filtered deaired saltwater and precautions were taken to flush out all air bubbles. A loading schedule of incrementally increasing vertical stress, selected to enhance the determination of the maximum preconsolidation stress, was followed. Direct permeability tests were begun once the vicinity of the maximum preconsolidation stress was reached. An alternating sequence of vertical loading and direct permeability testing was then followed allowing the determination of permeability as function of void ratio.

The samples chosen for this study consisted of carbonate-rich biogenic oozes from the equatorial Pacific Ocean and clays of predominantly smectite and illite from the North Pacific. The oozes were sampled from a standard piston core obtained during the WHOI cruise KNORR 73-4 immediately after the core was raised. This particular core showed cyclic variations of biogenic composition, ranging from 45% to 90% $CaCO_3$ and 1% to 30% SiO_2, correlated with glacial/interglacial sedimentation regimes. Sediments deposited during glaciation roughly account for over 90% of the recovered core. To characterize the glacial component, two samples were selected, 692-699 cm (90% $CaCO_3$) and 852-859 cm (82% $CaCO_3$). The sample selected from 345-350 cm is representative of the minor component deposited during the interglacial (55% $CaCO_3$, 30% SiO_2). These samples are summarized in Table 1. The data pertaining to the clays has been reported elsewhere by Silva et al. (1980) and consists of samples obtained from the cruises LONG LINES 44, VEMA 32-11

Table 1. Summary of Properties: Biogenic Sediments
Measured At 150 PSI Back-Pressure and Incrementally Increasing Vertical Stress

Station	Sample Depth (cm)	In-Situ Void Ratio	In-Situ Permeability (cm/sec)	Specific Gravity	Grain Size[1]			Mineralogy
					%Sand	%Silt	%Clay	
KNR 73-4	345-350	5.82	7.24×10^{-6}	2.45	12	37	51	Carbonate-Siliceous Ooze 55% $CaCO_3$ 30% SiO_2
7PC	692-699	2.15	2.92×10^{-6}	2.67	13	42	45	Calcuim Carbonate Ooze 90% $CaCO_3$ 4% SiO_2
1 02.2'N	797-804[2]	2.19	-	2.66	15	33	52	Calcium Carbonate Ooze 84% $CaCO_3$ 7% SiO_2
121 10.4'W	852-859	3.15	2.64×10^{-6}	2.68	8	56	36	Calcium Carbonate Ooze 82% $CaCO_3$ 5% SiO_2

1 Sand greater than 0.065mm diameter, clay less than 0.002mm diameter.
2 Consolidation sample studied without back-pressure.

and YALOC 74-3. The mineralogy of the cores from which these specimens were sampled ranged in composition from surficial illites (upper 6 meters) to smectitie-rich clays at greater depths.

The biogenic samples were studied using the constant head permeability test while both falling head and constant head tests were used in studying the clay specimens. Hydraulic gradients used for the constant head tests were in the range 5 to 10, while the initial gradients used in the falling head tests were less than 10. Hydraulic gradient, i, is a non-dimensional representation of the applied hydraulic pressure gradient. Derived directly from Darcy's law (equation 1), it is the ratio of hydraulic head, H, to the length of the specimen, L

$$\bar{v} = -(\frac{k}{\gamma}) \nabla P = ki \qquad \text{where } i = \frac{H}{L} \qquad (12)$$

Throughout these tests the height of the sample was monitored (to within 0.0025 mm) in order to determine void ratio changes accurately.

Figure 3 is a plot of the e log σ curve obtained for the three biogenic samples on which direct permeability measurements were conducted. Similar results obtained by consolidating a fourth sample, also selected from the KNR 73-4 core at 797-804 cm, using a standard consolidometer (no back-pressure), is included in Figure 3. The loading sequence followed while studying this sample was continuous (the pause between loads needed to run the direct permeability measurements in the back-pressured experiment was not necessary). In Figure 3 the values corresponding to σ_o and σ_c for each sample are indicated. The comparison of σ_o and σ_c is a rough measure of the past stress history of the sediment specimen (Skempton, 1970). The 797-804 cm and

Figure 3. Void ratio versus log of vertical stress results (e log σ)

pertaining to the three biogenic samples analysed (KNR 73-4, 7PC, 345-350 cm,

carbonate-siliceous ooze; 692-699 cm and 832-838 cm, carbonate ooze) and a

fourth sample (KNR 73-4, 7PC, 792-796 cm, carbonate ooze) studied using a

standard consolidometer. Maximum preconsolidation stress and the calculated

overburden stresses are indicated by σ_c and σ_o respectively.

VERTICAL STRESS
(Kg/cm²)

VERTICAL STRESS
(Kg/cm²)

345-350 cms.
55% CaCO₃-30% SiO₂

797-804 cms.
84% CaCO₃-7% SiO₂

VOID RATIO

692-699 cms.
90% CaCO₃-4% SiO₂

852-859 cms.
82% CaCO₃-5% SiO₂

VOID RATIO
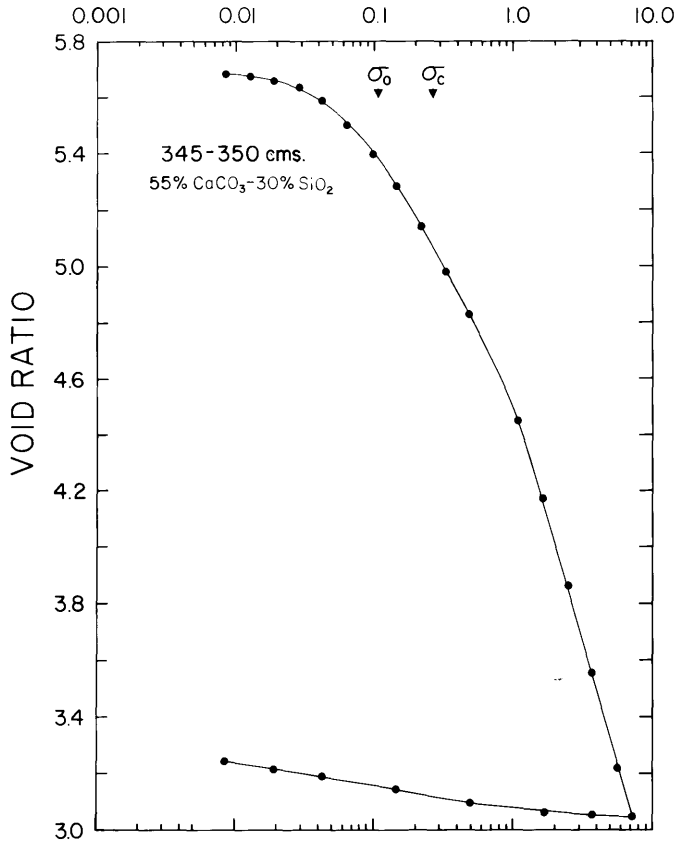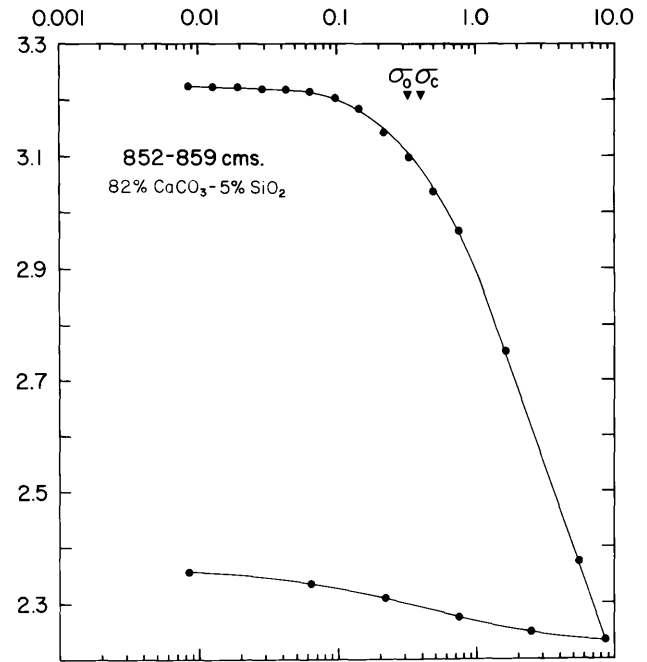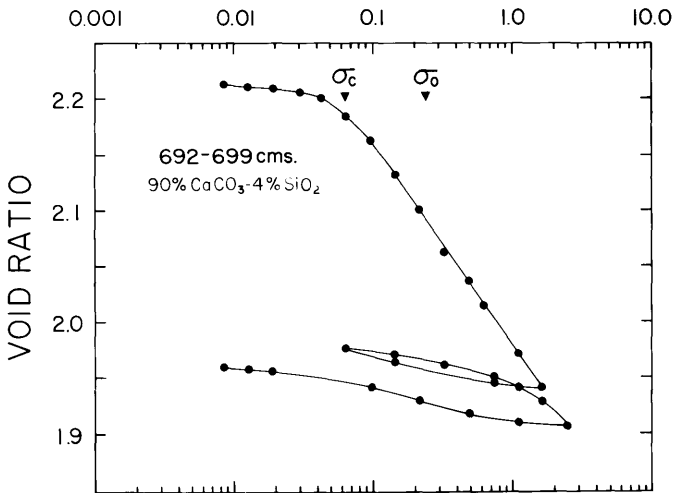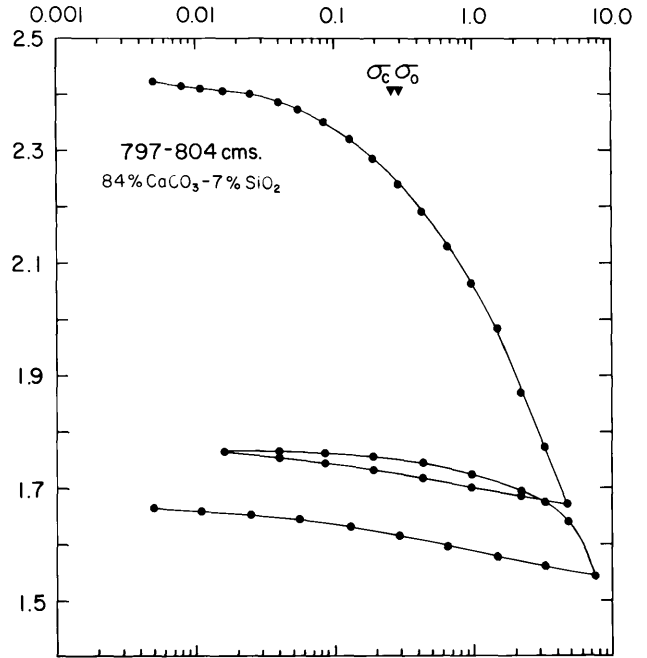
CONSOLIDATION RESULTS
KNORR 73-4
Piston Core 7

852-859 cm samples are both normally consolidated, that is, the observed

maximum preconsolidation stress, σ_o , is approximately equal to the calculated

overburden, σ_c. This is typical of deep sea sediments deposited in tranquil

environments and suggests that secondary consolidation occurring during the

direct permeability tests does not obscure the determination of the maximum

preconsolidation stress. The shallowest sample, 345-350 cm is slightly

overconsolidated, which is also a well observed phenomenon in deep-sea

sediments (Miller and Richards, 1969; Silva, 1979). The sample at 696-699 cm

indicates appreciable underconsolidation which is unexpected. According to

Terzaghi's concept of effective stress, this only occurs in the presence of

excess pore pressures. The reason for this anomalous zone of

underconsolidation can not be determined from the available information. The

degree of disturbance determined from the consolidation curves in Figure 3

suggests that our samples are of low disturbance.

Permeability as a function of void ratio and sediement type is summarized

in Figure 4. Also included in this figure are results pertaining to the

second phase of our experimentation discussed later. The illite and smectite

data sets in Figure 4 each consist of the combined permeability versus void

ratio curves of over twenty samples of similar mineralogical composition,

differing only slightly in grain-size distribution and in-situ void ratios.

Collectively they form a self-consistent data set representing the range of

permeability for North Pacific clays. For the three biogenic samples studied,

data obtained from each individual measurement are plotted (large circles) to

demonstrate the self-consistency of these tests. It is clear from Figure 4

that at similar void ratios there is approximately one order of magnitude

Figure 4. Permeability as a function of void ratio for the biogenic and clay

sediments from the North and Equatorial Pacific Ocean. The data for the

biogenic sediment consists of the results of three analyses. The individual

values from the biogenic sediment study are plotted as large solid circles.

The clay data is from Silva et al., (1980) and the cumulative results of a

series of analyses of samples of similar mineralogy. The results of the four

tests run to evaluate the effects of back-pressure and vertical stress are

also plotted and are grouped together by dashed lines.
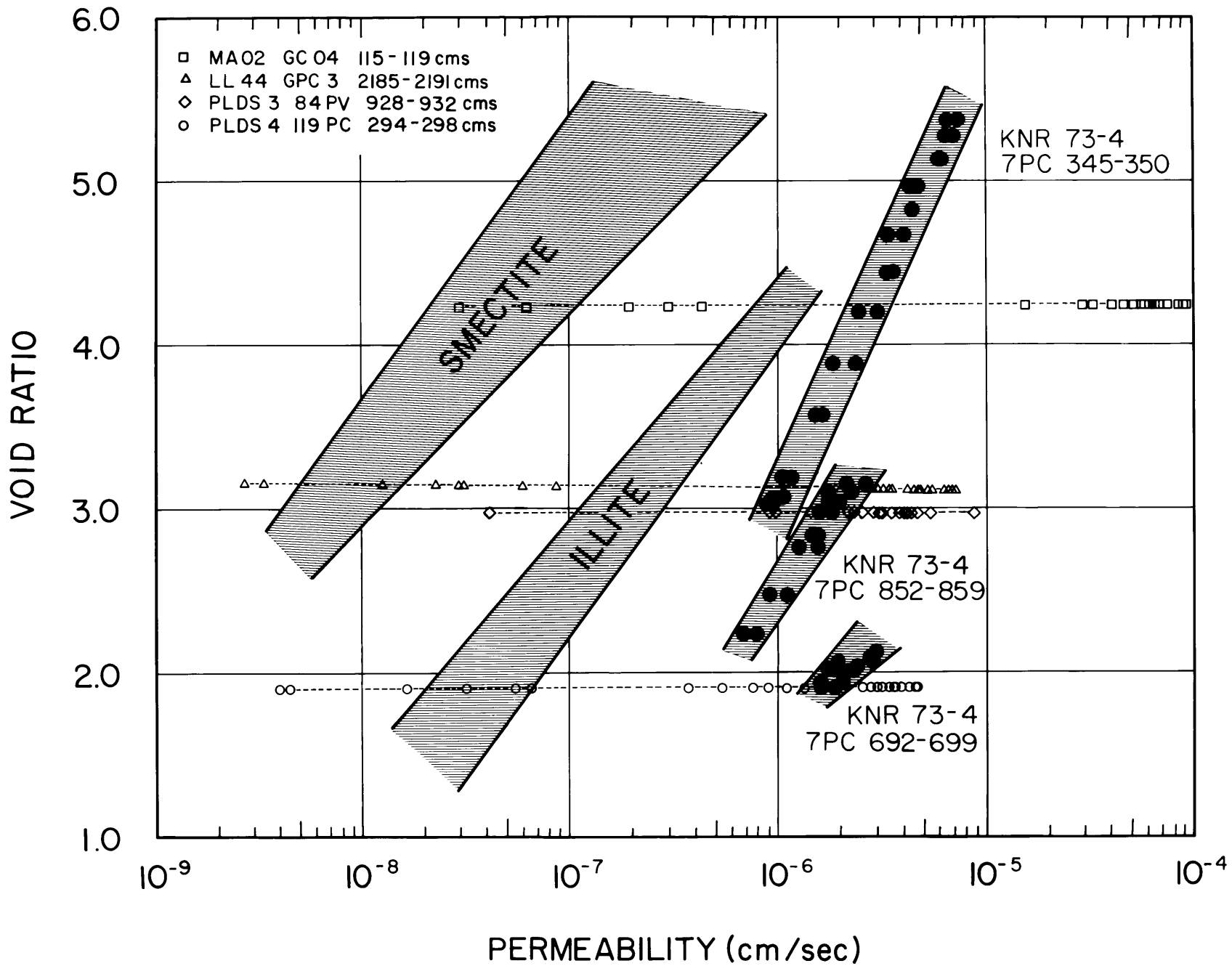
difference between the permeabilities of smectite and illite. At high void ratios the permeabilities of illite and the biogenic sediments are within an order of magnitude but differ by an order of magnitude at smaller void ratios. From the results of the three biogenic samples studied, it appears that a broad range of permeabilities and void ratios may characterize biogenic sediments reflecting the complex effect on pore size resulting from the large variations in grain-size and carbonate content that are possible.

In our measurements we cannot account for the effects of time (i.e. slow chemical reactions, diagenesis) or effects due to the difference in temperature and hydrostatic pressure between the laboratory and in-situ environments. If it is valid for us to assume these effects are of second order, the measurements allow some insight into the variation of sediment permeability as the process of consolidation progresses. The values of void ratio and permeability shown in Figure 4 correspond to results obtained at applied vertical stresses ranging from in-situ sample conditions to that corresponding to approximately 200 meters of overburden (8 kg/cm^2), based on our consolidation measurements and the core descriptions of the Deep Sea Drilling Project. We can speculate that within the thick accumulations of carbonate-rich sediments of the equatorial Pacific (Ewing et al., 1968), permeability will vary by only a factor of two (roughly between 0.6 - 1.2x10^{-6} cm/sec) over a depth of 200 meters. To visualize the effect of consolidation on the microstructure of the biogenic samples, we examined cross sections of the pore structure of these specimens under a scanning electron microscope (SEM), using the technique of Goreau and Honjo (1980). The pores of all three specimens can be characterized by thin elongated vents, less than

1.5 microns wide, within a flocculated structure of clay-silt sized

particles. As consolidation progresses, these elongated vents tend to close

bringing the flocculated particles closer together. Figures 5, a and b, are

SEM photographs of the microstructure of the 345-350 cm sample before and

after consolidation (0 and 8 kg/cm^2). These photographs were chosen as

examples because of the large changes in void ratio occurring during this

consolidation test, clearly demonstrating the nature of the changes occurring

in pore structure. Unlike the sample at 345-350 cm, the other two biogenic

specimens studied contained a large component of forams. SEM photographs

suggest that although large voids are included within these forams, their

contribution to permeability is minor, as they are completely isolated within

the matrix of finer sized particles.

(B) Analysis of the Effects of Back-Pressure and Vertical Stress

The use of back-pressure and in-situ vertical stresses requires a

substantial increase in the complexity of the experimental apparatus as well

as the amount of time needed to conduct individual measurements. A series of

tests were conducted to evaluate the necessity of insuring essentially

complete pore fluid saturation and a stable sediment structure. These tests

consisted of conducting direct permeability measurements under conditions of

negligible vertical stress (4 gm/cm^2) and back-pressure varying from 0 to

150 psi. Low hydraulic gradients (2-5) were used as a precaution against

altering flow paths by disturbing the sediment fabric (channeling) and thereby

increasing the observed permeability.

Four samples were used in this study summarized in Table 2. Table 3 is

Figure 5. Scanning electron microscope photographs of KNR 73-4, 7PC, 345-350

cm sample (a) prior to emplacement in the consolidation unit and (b) after

completion of consolidation test run to vertical stress of 8 kg/cm^2.

Magnification is 3000x.

10 Microns   10 Microns
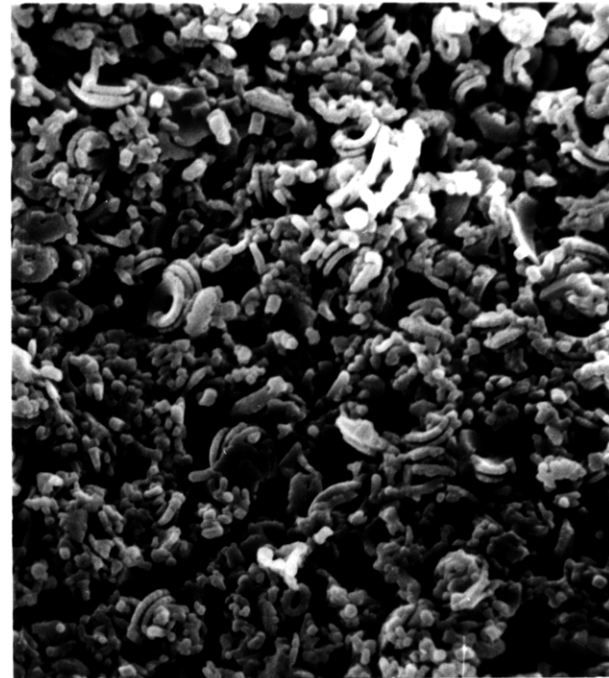
(A)   e=5.69   (B)   e=3.28

KNR 7PC
345-350 cm
55% $CaCO_3$ - 30% SiO_2

Table 2. Summary of Properties: Biogenic and Clay Samples
Measured At Various Back-Pressures and 4 gm/cm^2 Vertical Stress

Station		Latitude	Longitude	Sample Depth (cm)	Initial Void Ratio	Grain Size[1]			Specific Gravity	Mineralogy
						%Sand	%Silt	%Clay		
PLDS 3	84PV	0 57.7'N	126 37.3'W	882-886	2.99	11	•55	34	2.60	Calcium Carbonate Ooze
PLDS 4	119PC	(11 00.0'N)	(141 00.0'W)	290-294	1.94	2	84	14	2.67	Carbonate-Siliceous Ooze
MARA 02 GC 04		30 07.0'N	157 52.5'W	115-119	3.24	0.1	18	82	2.91	Illite
LL-44	GPC 3	30 19.9'N	157 49.4'W	2185-2191	4.26	1	43	56	2.78	Smectite

1 Sand greater than 0.065mm diameter, clay less than 0.002mm diameter.

Table 3. Summary of Measurements Run With Variable
Back-Pressure and Negligible Vertical Stress

Sample	Back-Pressure (psi)	N	Permeability (cm/sec)	S.D. (cm/sec)
LL-44	0	13	3.9E-5	3.6E-5
GPC 3	50	8	7.2E-5	2.6E-5
2185-2191cm	150	8	7.1E-5	2.3E-5
MA 02	0	8	3.0E-8	2.8E-8
GC 04	50	11	1.1E-5	1.1E-5
115-119cm	150	10	4.1E-6	1.7E-6
PLDS 4	0	12	4.5E-7	5.9E-7
119 PC	25	8	3.4E-6	9.3E-7
290-294cm	50	8	3.3E-6	9.6E-7
	150	10	3.8E-6	7.4E-7
PLDS 3	0	8	2.9E-6	2.8E-6
84 PV	25	6	3.8E-6	1.3E-6
882-886cm	50	8	3.3E-6	5.4E-7
	100	9	1.4E-6	1.1E-6

a summary of the results of these tests as a function of back-pressure (0-150 psi). The table lists the average and standard deviation of the observed permeabilities for the back-pressures as well as the number of measurements conducted at that back-pressure.

The results of the first few direct permeability tests for all four specimens, conducted without back-pressure, showed unusually low permeabilities. This is reflected in Table 3 by the large standard deviations at zero back-pressure. After a length of time amounting to several hundred minutes of testing time and several days of specimen residence in the consolidation unit, the measured values of permeability increased, in some cases by orders of magnitude. In Figure 4 these results are plotted as a function of void ratio (the samples are identified in the upper left hand corner). This figure demonstrates both the magnitude of the scatter in the measurements and the relationship of these results to that obtained with in-situ vertical and suitable values of back-pressure. All of the low permeability values were measured without back-pressure. Two samples, LL-44 and PLSDS-3, underwent drastic changes in permeability during the testing at zero back-pressure which we interpret as due to channelling, resulting in the enormous standard deviations listed in Table 3. The larger values measured for the MA-02 and PLDS-4 samples did not occur until back-pressure was applied, however, the values measured were not reproduceable. These values are also interpreted as resulting from channelling. In contrast to these measurements, the results obtained using vertical stress and back-pressure are self-consistent and highly reproduceable, exhibiting little scatter.

It is our opinion that the initial low permeability measurements are not

representative of the true permeability at the calculated void ratio for the four samples studied in this second experiment. We attribute these low values to the effects of incomplete saturation. In tests where back-pressure is applied across samples before testing begins, this phenomenon is not observed. It can be argued that for the samples chosen for this study it unlikely that a supersaturated gas phase such as methane or carbon dioxide exists in the pore fluids in-situ which would release gas bubbles under the conditions existing in the laboratory. However, the process of sampling and emplacement into the consolidation unit certainly introduces gas into the system. Most important is the exposure of the faces of the specimens, of which the surface area is very large, to the atmosphere trapping within it a layer of air which may account for the observed initial low values of permeability.

Direct measurements of deep-sea sediment permeability such as those reported by Pearson and Lister (1973) and Abbott et al. (1979, in press) are measurements in which the effects of back-pressure and vertical stress are assumed negligible. Without the complete saturation of the pore fluid and the stability of the soil structure, direct permeability measurements may not reflect in-situ values.

CONCLUSIONS:

Direct measurement of the permeability of carbonate-rich biogenic sediments resulted in permeabilities within the range of $2-6 \times 10^{-6}$ cm/sec for calcium-carbonate contents ranging from 55 to 90%. Complete saturation of the pore fluids and a stable microstructure was ensured by the use of

back-pressure (hydrostatic) and vertical stress respectively. The study of the relationship between permeability and consolidation suggested that within the thick sequences of carbonate sediment in the equatorial Pacific, changes in permeabltiy of only a factor of two occur over 200 meter of depth. SEM photographs of sediment microstructure suggest that the observed changes in permeability can be accounted for by the gradual closing of individual elongated pores occurring within a structure consisting of flocculated clay and silt sized particles.

The results of direct measurements made without back-pressure and vertical stress showed great scatter. This variability is attributed to both the presence of gas at the boundaries of the sample and the response of a weak sediment structure to applied hydraulic gradients. Unless complete saturation of the pore fluid and stability of the soil structure is assured, direct permeability measurements may not reflect in-situ values.

BIBLIOGRAPHY:

Abbott, D. H., M. A. Hobart, W. Menke and R. N. Anderson, Permeability and heat flow results from the Southwest Indian Ocean, AGU abstract, EOS, 60, 382, 1979.

Abbott, D. H., W. Menke, M. A. Hobart and R. N. Anderson, Evidence for excess pore pressures in Southwest Indian Ocean sediments, submitted to J. Geophys. Res.

Anderson, D. R., Nuclear waste disposal in subseabed geologic formations: the seabed disposal program, 40p., SAND78-2211, Sandia Laboratories, May, 1979.

Anderson, R. N., M. G. Langseth and J. G. Sclater, The mechanisms of heat transfer through the floor of the Indian Ocean, J. Geophys. Res., 82, 3391-3409, 1977.

Anderson, R. N., M. A. Hobart and M. G. Langseth, Geothermal convection through oceanic crust and sediments in the Indian Ocean, Science, 204, 828-832, 1979.

Averjanov, S. F., About permeability of subsurface soils in case of incomplete saturation, Engineering Collection, 7, 1950, discussed by P. Ya Polubarinova, Theory of Ground Water Movement, English translation by J. M. R. DeWiest, Princeton University Press, 1962.

Black, D. A. and K. L. Lee, Saturating laboratory samples by back pressure, JSMFD, ASCE, 99, 75-93, 1973.

Brooks, R. H. and A. T. Corey, Properties of porous media affecting fluid flow, JIDD, ASCE, 92, 61-88, 1966.

Brownscombe, E. R., R. L. Slobod and B. H. Caudle, Laboratory determination of relative permeability, Parts 1 and 2, Oil & Gas J., 48, 68-69, 81-82, 98-102, 123, 1950.

Carman, P. C., Flow of Gas Through Porous Media, Academic, New York, 1956.

Casagrande, A., The determination of the pre-consolidation load and its practical significance, Proc. 1st Int. Conf. on Soil Mech., Harvard, 3, 60-64, 1936.

Crowe, J., R. P. Von Herzen and K. E. Green, The eastern equatorial Pacific Ocean heat flow low: evidence of hydrothermal circulation within 15 to 40 Ma crust, submitted to J. Geophys. Res.

Darcy, H. P. G., Les fontaines publiques de Dijon, Victor Delmont, Paris, France, 1856.

Ewing, J., M. Ewing, T. Aitken and W. J. Ludwig, North Pacific sediment layers measured by seismic profiling, Geophysical Monograph No. 12, ed. L. Knopoff, C. L. Drake and P. J. Hart, American Geophysical Union, Washington, D.C., 147-173, 1968.

Goreau, M. and S. Honjo, A freeze fracture method: observation of fresh marine sediment under SEM, submitted to Marine Geology.

Irmay, S., On the hydraulic conductivity of unsaturated soils, AGU Trans., 35, 463-467, 1954.

Jambu, N., Consolidation of clay layers based on non-linear stress strain, Proc. 6th Int. Conf. on Soil Mech. & Foundation Engr., Montreal, 2, 83-87, 1965.

Langseth, M. G. and B. M. Herman, Heat transfer in the oceanic crust of the Brazil Basin, submitted to J. Geophys. Res.

Lee, K. L. and D. K. Black, Time to dissolve air bubble in drain line, JSMFD, ASCE, 98, 181-194, 1972.

Lowe, J. and T. C. Johnson, Use of back pressure to increase degree of saturation of triaxial test specimens, ASCE, Res. Conf. on Shear Strength of Cohesive Soils, Boulder, CO, 819-836, 1960.

Miller, D. G. and A. F. Richards, Consolidation and sedimentation-compression studies of a calcareous core, Exuma Sound, ASCE, Res. Conf. on Shear Strength of Cohesive Soils, Boulder, CO, 819-836, 1960.

Mitchell, J. K., Fundamentals of Soil Behavior, Wiley, New York, 1976.

Mualem, Y., Hydraulic conductivity of unsaturated porous media: generalized macroscopic approach, Water Resources Res., 14, 325-334, 1978.

Muskat, M. and M. W. Meres, The flow of heterogeneous fluids through porous media, Physics, 7, 346-363, 1936.

Pearson, W. C. and C. R. B. Lister, Permeability measurements on a deep-sea core, J. Geophys. Res., 78, 7786-7787, 1973.

Schmertmann, J. H., Estimating the true consolidation behavior of clay from laboratory test results, Proc. ASCE, 79, Seperate No. 311, 1-25, 1953.

Silva, A. J., Marine geomechanics: overview and projections, In A. L. Inderbitzen, ed., Deep-Sea Sediments, N. Y., Plenum Press, 45-62, 1974.

Silva, A. J., J. R. Hetherman and D. I. Calnan, Low gradient permeability testing of fine-grained marine sediments, submitted to the American Soc. for Testing and Materials.

Silva, A. J., Geotechnical properties of deep sea clays - a brief discussion, 1st Canadian Conf. on Marine Geotechnical Engineering, Calgary, Canada, 1979.

Skempton, A. W., The consolidation of clays by gravitational compaction, Q. Jl. geol. Soc. Lond., 125, 373-411, 1970.

Terzaghi, K., The shearing resistance of saturated soils, Proc. 1st Int. Conf. on Soil Mech., Harvard, 1, 54-56, 1936.

Wyckoff, R. O. and H. C. Botset, The flow of gas-liquid mixtures through unconsolidated sands, Physics, 7, 325-345, 1936.

Yuster, S. T., Theoretical considerations of multiphase flow in idealized capillary systems, Third World Petroleum Congress, The Hague, Sec. II, 437-445, 1951.

CHAPTER IV

Comparison of Geochemical and Geophysical Estimates

of Convective Flow Through Marine Sediments

by

John Crowe

Dept. of Earth and Planetary Sciences
Massachusetts Institute of Technology, Cambridge, MA   02139

Dept. of Geology and Geophysics
Woods Hole Oceanographic Institution, Woods Hole, MA   02543

and

Russell E. McDuff

Dept. of Earth and Planetary Sciences
Massachusetts Institute of Technology, Cambridge, MA   02139

ABSTRACT:

Recent reports of geothermal observations in deep sea rises and basins that suggest the transport of heat by the mass movement of fluid through sediments have yet to be verified by independent experimentation. Profiles of. temperature and pore water chemistry over a depth of eleven meters were compared at three sites in the equatorial Pacific Ocean where thermal evidence of hydrothermal circulation was present. Volume flux rates based on the geothermal data were between 6.3×10^{-7} and 2.4×10^{-6} cm/sec, approximately three orders of magnitude greater than those accomodated by the sulfate profiles, $1.2 - 2.4 \times 10^{-9}$ cm/sec. This difference is difficult to explain by experimental uncertainty, and attempts to account for the observed geothermal data using purely conductive thermal models are unsuccessful. Mo eling of sulfate depletion by the oxidation of organically bound sulfur suggests sulfate reduction rates of 1.1 to 2.5×10^{-12} mM/sec, compatible with other published results.

INTRODUCTION:

Hydrothermal convection within the oceanic crust has been suggested as an important heat transport mechanism at both spreading centers (Lister, 1970 and 1972; Talwani et al., 1971) and in areas of older crust (Sclater et al., 1974; Anderson et al., 1977). The hydrothermal circulation of seawater within the oceanic crust at active ridge crests has been widely accepted as both the major heat transport mechanism in newly formed crust and a site of chemical transformations important in controlling the composition of seawater. Sclater

et al. (1980) estimated 90% of the total heat loss of the oceans to be due to plate creation with 30% of this loss by advection near active spreading centers. In older regions, much of the observed variability in heat flow measurements has been associated with convection cells within the crust, initiated at the spreading axis and migrating with the plate.

The existence of hydrothermal circulation has been verified at the Galapagos Spreading Center (Williams et al., 1979; Corliss et al., 1979) and at the crest of the East Pacific Rise at 21°N (Spiess et al., 1980). Non-linear temperature gradient measurements made using the deep-submersible ALVIN south of the Galagagos Spreading Center were interpreted by Williams et al. (1979) using a one-dimensional model that assumed the transport of heat by both conduction and convection through the sediment. Flows of up to 10^{-4} cm/sec were calculated.

In their study of the geothermal regime of the Indian Ocean, Anderson et al. (1977) distinguished two thermal regimes within oceanic crust on the basis of geothermal observations: (1) a convective region which includes both spreading centers and ridge flanks where convection is dominant, (2) a conductive region which includes the basins where conduction is the dominant heat transfer mechanism. The nature of the transition between these two regions is thought to be related to the hydraulic resistance of the overlying sediment layer offered to the convection system, eventually masking the effects of and confining the circulation to the crust. This model was first proposed by Sclater et al. (1974) and its application to the data of the Pacific by Sclater et al. (1976) was successful. A second model of the transition zone, proposed by Anderson et al. (1977), consisted of the sealing

of the oceanic crust by hydrothermal precipitation. They concluded from compiled heat flow data that in the Indian Ocean the effects of convective heat exchange persists to crust of approximately 40 to 60 m.y.

Geothermal evidence of heat transport by the movement of seawater through the sediment cover in older crustal regions was reported by Anderson et al. (1979); non-linear temperature gradients similar to those observed at the Galapagos Spreading Center were observed in the Indian Ocean suggesting flows on the order of magnitude of 10^{-6} cm/sec. Oscillatory patterns of heat flow observed in closely spaced measurements were interpreted as resulting from cellular convection within the crust and sediment cover. They speculated that the transport of heat by geothermal convection may occur over more than one third of the entire surface of the ocean floor. Similar observations have been made on old crust in the Brazil Basin (Langseth and Herman, in press), the equatorial Pacific Ocean (Crowe et al., in preparation) and the Guatemala Basin (Anderson, personal communication).

The existence of fluid convection through sediments at the velocities predicted by the geothermal data would certainly alter our present concepts in such fields as pore water geochemistry, physical properties of sediments and the diagenesis of sediments. Of prime importance are its implications on the proposed disposal of nuclear waste within the sedimentary environment.

There have yet to be observations other than geothermal data that suggest the movement of interstitial fluid through sediments at velocities of 10^{-6} – 10^{-5} cm/sec. To constrain this problem, we compared the fluid fluxes predicted by both geothermal and geochemical data from three piston cores collected in the equatorial Pacific Ocean (Figure 1). These cores are

Figure 1. Locations of the three piston core sites in the equatorial Pacific Ocean used in this study.

6 PC • • 5 PC
• 7 PC
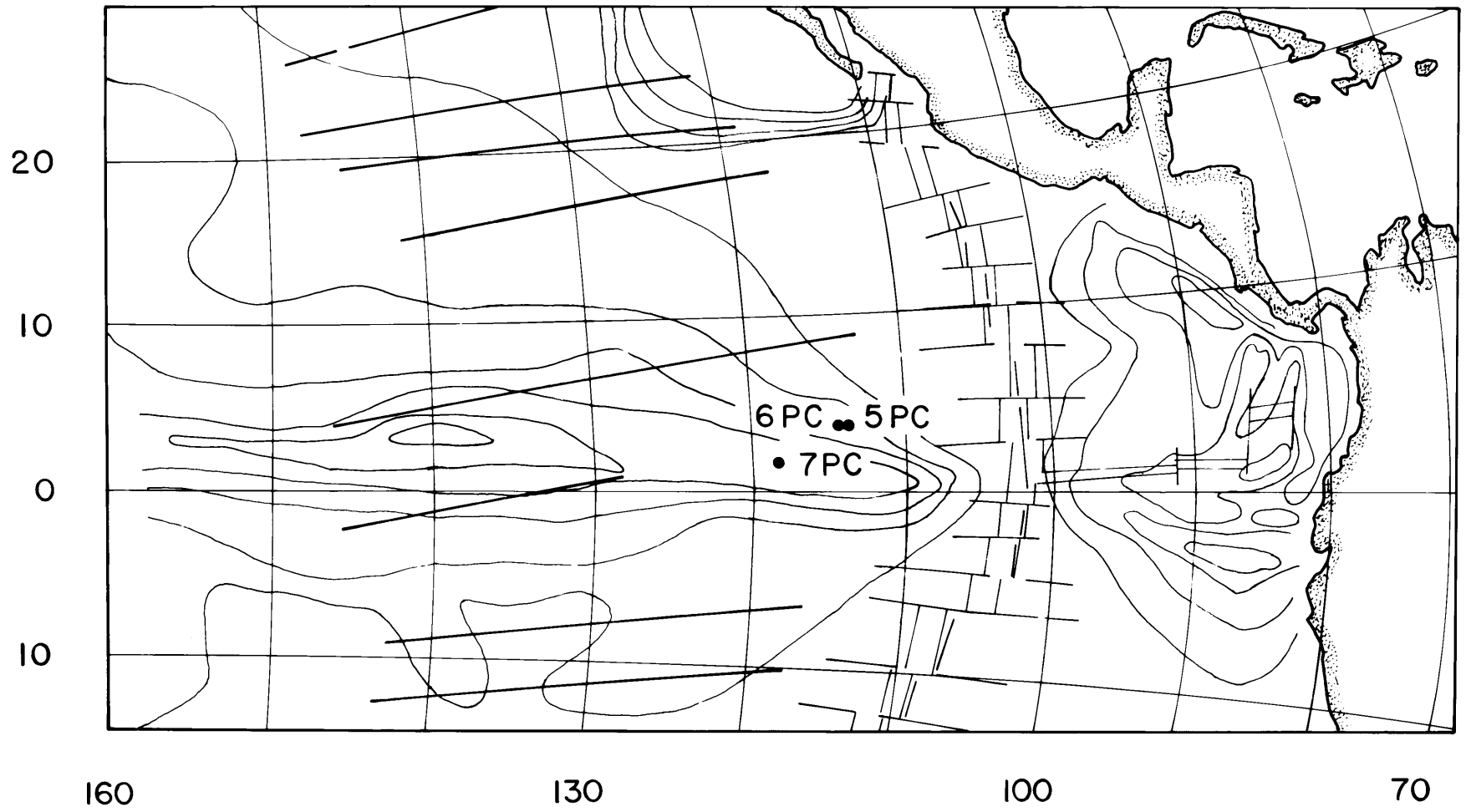
situated within the equatorial Pacific sediment bulge which is a thick

accumulation of biogenic ooze reaching at some points over 600 meters of

sediment. The sediment isopachs of Ewing et al. (1968) as well as the trends

of the major tectonic features are included in Figure 1. Cores 5 and 6 PC are

situated in over 200 meters of sediment that completely covers the oceanic

basement. Core 7PC is located in over 400 meters of sediment. Although the

permeability of these sediments is quite low, 6×10^{-7} to 3×10^{-6} cm/sec

(Crowe and Silva, in preparation), they are one to two orders of magnitude

more permeable than the red clays typical of the North Pacific. At velocities

of 10^{-6} - 10^{-5} cm/sec the distribution of major cations and anions within

the sedimentary layer would be controlled by advection. An exponentially

varying chemical gradient similar to the temperature profile would be

produced. Since the coefficient of chemical diffusivity is orders of

magnitude less than that of thermal diffusivity, the geochemical profile will

have a greatly reduced e-folding depth, allowing the velocities predicted by

geothermal data to be independently checked. Sulfate was used as the chemical

tracer. Velocities suggested by these two independent data sets did not agree

and their variance is difficult to explain.

METHODS:

The interstitial water samples were obtained by squeezing sediment at

selected depths in the piston cores shortly after the core was brought aboard

the ship. The major cations and anions of seawater other than sulfate were

determined using the techniques summarized by Gieskes (1974), however, there

were no resolvable gradients of these species. Sulfate was determined by

precipitation of the sulfate as lead sulfate and determination of the excess lead by pulse polarography (Luther and Meyerson, 1975).

The geothermal profiles were obtained by attaching temperature sensitive probes to the piston core pipe at seven locations (Von Herzen and Anderson, 1972) and digitally recording the data to accuracies of a few thousanths of a degree. Thermal conductivity was measured on core samples shipboard using the needle probe technique of Von Herzen and Maxwell (1959). The reduction of this data is discussed in detail by Crowe et al. (in preparation).

DISCUSSION OF DATA AND INTERPRETATION OF RESULTS:

The geothermal data is presented in Figures 2a, b and c. Temperatures with error bars are plotted as a function of depth. To the right of these profiles are the results of the thermal conductivity measurements. Figures 3a, b and c are the corresponding sulfate concentrations versus depth. The value at the sediment/seawater interface is taken as that of seawater of the appropriate chlorinity, 28.75 mM.

For both data sets the governing equations are nearly identical, differing only in boundary conditions and source/sink terms.

Sulfate is a suitable geochemical tracer for two reasons. First, there are no "sqeezing effects", chemical reactions that alter the sulfate concentration upon removal from in-situ conditions of temperature and pressure (Sayles and Manheim, 1975). Second, the only reaction important involving sulfate is its reduction coupled to the oxidation of organic carbon:

Figure 2. Temperature data (with error bars) and thermal conductivity as a function of depth for (a) 5PC, (b) 6PC and (c) 7PC. The solid lines are the temperature profile defined by the best fit of the parameters to the observed data. The dashed lines are the temperature profiles that would result from the flow velocity suggested by the geochemical data.
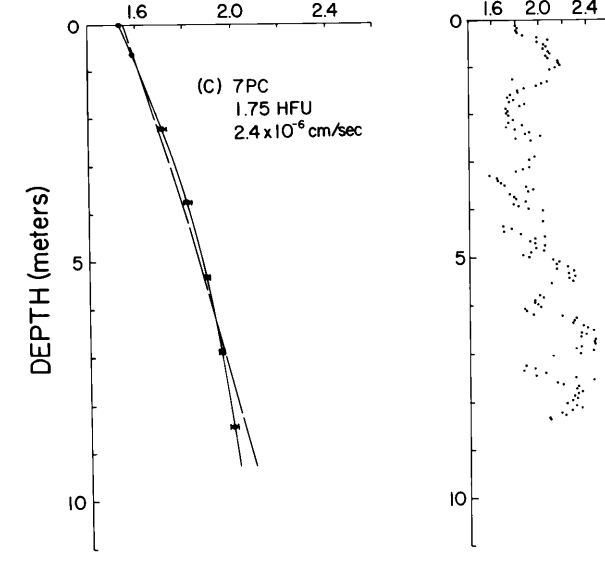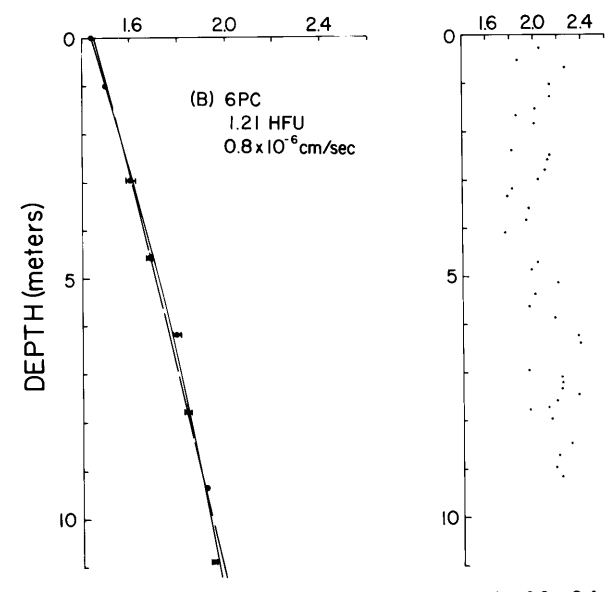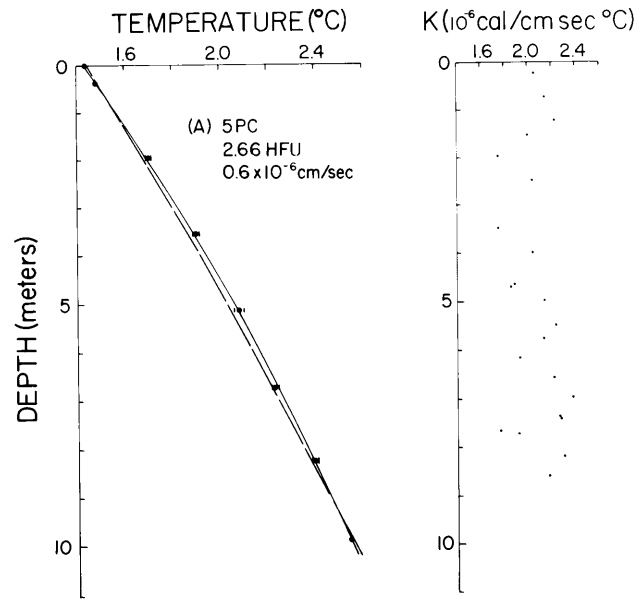
TEMPERATURE (°C)

K (10⁶ cal/cm sec °C)

DEPTH (meters)

(A) 5PC
2.66 HFU
0.6 x 10⁻⁶ cm/sec

(B) 6PC
1.21 HFU
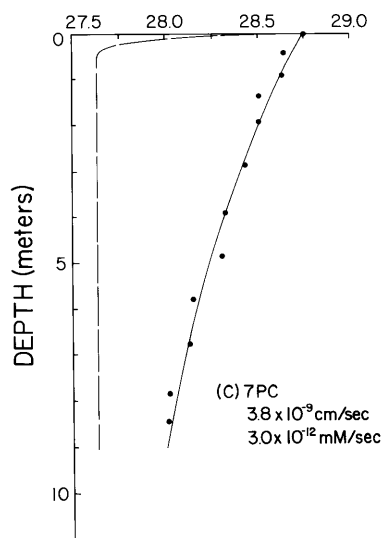0.8 x 10⁻⁶ cm/sec

(C) 7PC
1.75 HFU
2.4 x 10⁻⁶ cm/sec

Figure 3. Concentration of sulfate versus depth at (a) 5PC, (b) 6PC and 7PC. The solid lines are the sulfate profiles defined by the best fit of the parameters to the data. The dashed lines are representative of the sulfate profiles that would result from the flow velocities suggested by the geothermal data.

SULFATE (mM)

(A) 5PC
3.8 x 10⁻⁹ cm/sec
4.1 x 10⁻¹² mM/sec

(B) 6PC
1.9 x 10⁻⁹ cm/sec
1.8 x 10⁻¹² mM/sec

(C) 7PC
3.8 x 10⁻⁹ cm/sec
3.0 x 10⁻¹² mM/sec

$$2CH_2O + SO_4^{-2} \rightarrow 2HCO_3^- + HS^- + H^+ \tag{1}$$
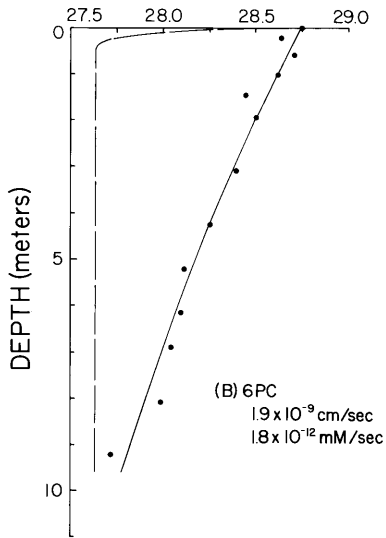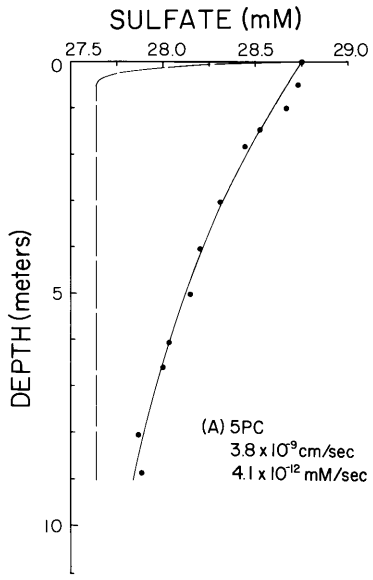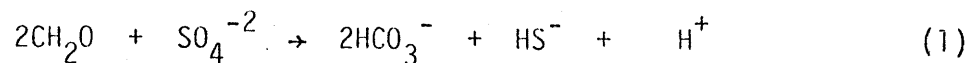
leading to depletion with increasing depth. The depth distribution can be modeled with the diffusion-advection-reaction equation. At steady state:

$$0 = D \frac{d^2c}{dz^2} + W \frac{dc}{dz} + J \tag{2}$$

where J is a chemical source/sink function (positive for a source), z is the spatial coordinate (positive downward), D is the chemical diffusion coefficient, c is the concentration of sulfate and W is the advective velocity (positive upwards). The solution to equation 2 is

$$\frac{c - c_o}{c_b - c_o} = f(z) + \frac{J\, z_b}{(c_b - c_o)W} \left(f(z) - \frac{z}{z_b} \right) \tag{3}$$

where $f(z) = (\exp(z/z^*) - 1)/(\exp(z_b/z^*) - 1)$, $z^* = D/W$, c_o is the concentration of sulfate at sediment/seawater interface and c_b is the concentration of sulfate at depth z_b.

Similarly, the general steady-state equation of heat conservation for transport in the vertical direction only is

$$0 = \underline{\nabla} \cdot \underline{q} = -k \frac{d^2T}{dz^2} + W \frac{dT}{dz} \tag{4}$$

where q is the vertical heat flux, z is vertical distance (positive downwards), W is the vertical volume flux (positive upwards), k is thermal diffusivity ($= K/\rho c_p$), ρ is fluid density, c_p is fluid heat capacity and

K is the thermal conductivity of the saturated bulk sediment. Subject to the conditions $T = 0$ at $z = 0$ (the sediment/seawater boundary) and q constant (q_0) everywhere, the solution to equation 4 is

$$T(z) = \frac{q_0}{\rho c_p W} (1 - e^{-Wz/k})$$

(5)

(Sleep and Wolery, 1978; Williams et al., 1979). The formulation of equation 5 incorporating the variation of thermal conductivity with depth and the variation of the location of the temperature sensors relative to the sediment/seawater interface is presented by Crowe et al. (in preparation).

To determine the best estimate and the range of model parameters from our observed data, weighted least squares fits of equations 3 and 5 to the data were obtained by means of stepwise Gauss-Newton iterations on the undetermined parameters of the equations. Crowe et al. (in preparation) discuss the formulation of this non-linear regression technique. From this method we obtain the best fit parameters, the standard deviations and correlation coefficients. The best fit of the parameters to each data set is shown in Figures 2 and 3 by solid lines drawn through the data. Table 1 summarizes the results of both the geothermal and geochemical results obtained in this manner.

The individual sulfate analyses were considered to be of equal weight, however, the temperature data were assigned weights according to assigned errors. The diffusivity of sulfate was estimated from the relationship $D = D_p/F$ (= pD_b in McDuff and Gieskes, 1976) where D_p is the solution diffusion coefficient, p is porosity and F is the formation factor. D_p was

Table 1. Flow Rates Derived From Geothermal And Geochemical Data

| Core | Latitude | Longitude | Depth[1] | Geothermal | | Geochemical | |
				Heat Flux[2]	Volume Flux[3] (10^{-6} cm/sec)	Volume Flux[3] (10^{-9} cm/sec)	Sink (10^{-12} mM/sec)
5PC	4 00.0'	-114 00.8'	3869	2.66 +/-0.11	0.6 +/-0.2	3.8 +/-0.9	4.1 +/-0.9
6PC	4 00.7'	-114 10.1'	3934	1.21 +/-0.15	0.8 +/-0.5	1.9 +/-1.2	1.8 +/-1.2
7PC	1 45.0'	-118 22.5'	4166	1.75 +/-0.06	2.4 +/-0.2	3.8 +/-1.2	3.0 +/-1.0

1 Depth in corrected meters.
2 Heat flux in cal/cm^2-sec x 10^{-6}.
3 Volume flux (porosity x fluid velocity).

taken as the tracer diffusion coefficient at 2^0C (5.1×10^{-6} cm^2/sec)

and F estimated from the porosity data and the F-p relation for similar

carbonates, $F = 1.07p^{-1.41}$ (McDuff and Ellis, 1979; McDuff, 1978). For the

appropriate porosity range of 70 to 80%, D is 2.9 - 3.5×10^{-6} cm^2/sec.

Because the reaction leading to depletion is a sink, $J < 0$, fits were made for

both $W = 0$ and $J = 0$, with the $J = 0$ fit yielding the maximum upward velocity.

The detailed thermal conductivity measurements, accurate to about 10%

(Von Herzen and Maxwell, 1959), reflect the variation of both porosity and

mineral composition with depth. These sediments range in porosity from 65 to

90% and in composition from 1% SiO_2, 90% $CaCO_3$ to 30% SiO_2, 50% $CaCO_3$

reflecting respectively the glacial/interglacial sedimentation regimes

(Arrhenius, 1952). Since the glacial sedimentation rate greatly exceeds the

interglacial, the core is predominantly carbonate.

For the geothermal data there is some uncertainty as to the actual depth

of penetration. A linear fit to the temperature gradient results in a greater

depth of penetration for the piston core than that suggested by the results of

the convection model. Corehead photographs taken during stations 5PC and 7PC

support the best fit depth of penetration suggested by the convection model

supporting the observed non-linearity of the geothermal data.

DISCUSSION:

In order to reconcile the difference between the geothermal and

geochemical data we have examined the ranges of possible best fit parameters

that successfully describe the observed data. The ranges of these parameters

do not show any compatibility between the two data sets.

The geochemical model seems relatively reliable. The lack of a squeezing effect is indicated by the agreement of the extrapolated interface values and the water column concentration calculated from the water column chlorinity and the seawater SO_4/Cl ratio (Figures 3a, b and c). Though Sayles (1979) has inferred some oxidation of organically bound S in sediments accumulating at lower rates, it is clear from the magnitude of the depletion seen here that reduction is occurring in these sediments, i.e. the $J < 0$ assumption seems sound. Further, the gradients observed are similar to those calculated from the gradient-sedimentation rate relation reported by Berner (1978).

Similarly, we can examine whether conductive heat transport theory is adequate to explain the observed geothermal data. Two simple conductive models are considered as alternatives to the proposed convective model. The first is a study of the effects of hydrothermal circulation confined to within the crust on the temperature structure at the seawater/sediment interface of an impermeable sediment cover. The model is formulated as a impermeable layer of sediment with upper and lower boundaries at $z = 0$ and $z = L$ respectively. The transport of heat within this layer is governed by the equation of heat diffusion:

$$0 = \frac{dT}{dt} - k \nabla^2 T \qquad (6)$$

where k is the thermal diffusivity of this layer. Modeling the effect of a convection cell to be that of an oscillatory temperature preturbation at the lower boundary of the sediment layer, it can be show that the observed non-linear temperature gradients cannot be explained by such a model. The effect of a relative motion between the plate and the convection cell over a

wide range of velocities was studied. If the wavelength of the cell is large, 5 km, (Ribando, et al., 1976; Green, 1980) compared to the thickness of the sediment layer, 100-500 meters, the problem reduces to only the vertical spatial component and the temporal variable t. The problem is now the one dimensional heat diffusion problem with an oscillating temperature at its lower boundary. For the initial conditions $T = 0$ and $T = T_L$ at $z = 0$ and $z = L$ respectively, and a boundary condition $T = T_L + T_0 \sin(\omega t + \epsilon)$ at $z = L$ where T_0, ω and ϵ are the amplitude, frequency and phase of the disturbance, the temperature field within the sediment layer is given by (Carslaw and Jaegar, 1959, p. 105)

$$T(z,t) = \frac{T_L z}{L} + T_0 A \sin(\omega t + \epsilon + \phi) + $$

$$2\pi k T_0 \sum_{n=1}^{\infty} \frac{n(-1)^n (kn^2\pi^2 \sin \epsilon - \omega L^2 \cos \epsilon)}{k^2 n^4 \pi^4 + \omega^2 L^4} \sin(\frac{n\pi z}{L}) \exp(-kn^2\pi^2 t/L^2)$$

(7)

where A and ϕ are the magnitude and phase of the steady-state temperature oscillation at the point z

$$A = \left| \frac{\sinh \xi z(1+i)}{\sinh \xi L(1+i)} \right|$$

$$\phi = \arg \left\{ \frac{\sinh \xi z(1+i)}{\sinh \xi L(1+i)} \right\}$$

$$\xi = (\frac{\omega}{2k})^{1/2}$$

$$\omega = \frac{2\pi v}{\lambda}$$

where v is equal to the relative velocity between the sediment layer and the convection cell within the crustal layer and λ is the wavelength of the convection cell.

The third term of equation 7 is the transient solution. This term dies out quickly depending upon the thermal time constant of the layer, $\tau = k/L^2$ ($\tau(200$ meters$)$ = 5000 years; $\tau(400$ meters$)$ = 25,000 years). The expression $\sum_{n=1}^{\infty} \exp(-n^2\pi^2 t/\tau)$ as a function of t/τ is plotted in Figure 4 demonstrating the short time necessary for steady state to be reached, about one time constant.

The second term of equation 7 is the periodic steady-state solution. Of interest is the range of ω and L for which this term is significant. The variation of A across the cross section of the slab for different values of ξL is shown in Figure 5. A is a maximum for $\xi L < 1.0$. From Figure 5, $A \propto z/L$ for $\xi L < 1.0$. If the curvature of equation 7 is compared to that observed in our non-linear gradients, by comparing the respective second derivatives we find that, for equation 7

$$|T''| = \left| \frac{T_0 \omega A}{k} \cos(\omega t + \epsilon + \phi) \right| < \frac{T_0 \omega A}{k} \tag{8}$$

if $\xi L < 1$, then $A = A_{max} = z/L$. Therefore $\omega < 2k/L^2$. Equation 8 is now

$$|T''| < \frac{T_0 \omega A}{k} = \frac{2T_0 z}{L^3} \tag{9}$$

The smallest detectable value of d^2T/dz^2 in the observed data (Crowe et

Figure 4. Non-dimensionalized plot of $\sum\limits_{n=1}^{\infty} \exp(-kn^2\pi^2 t/L^2)$ versus time (from equation 7).
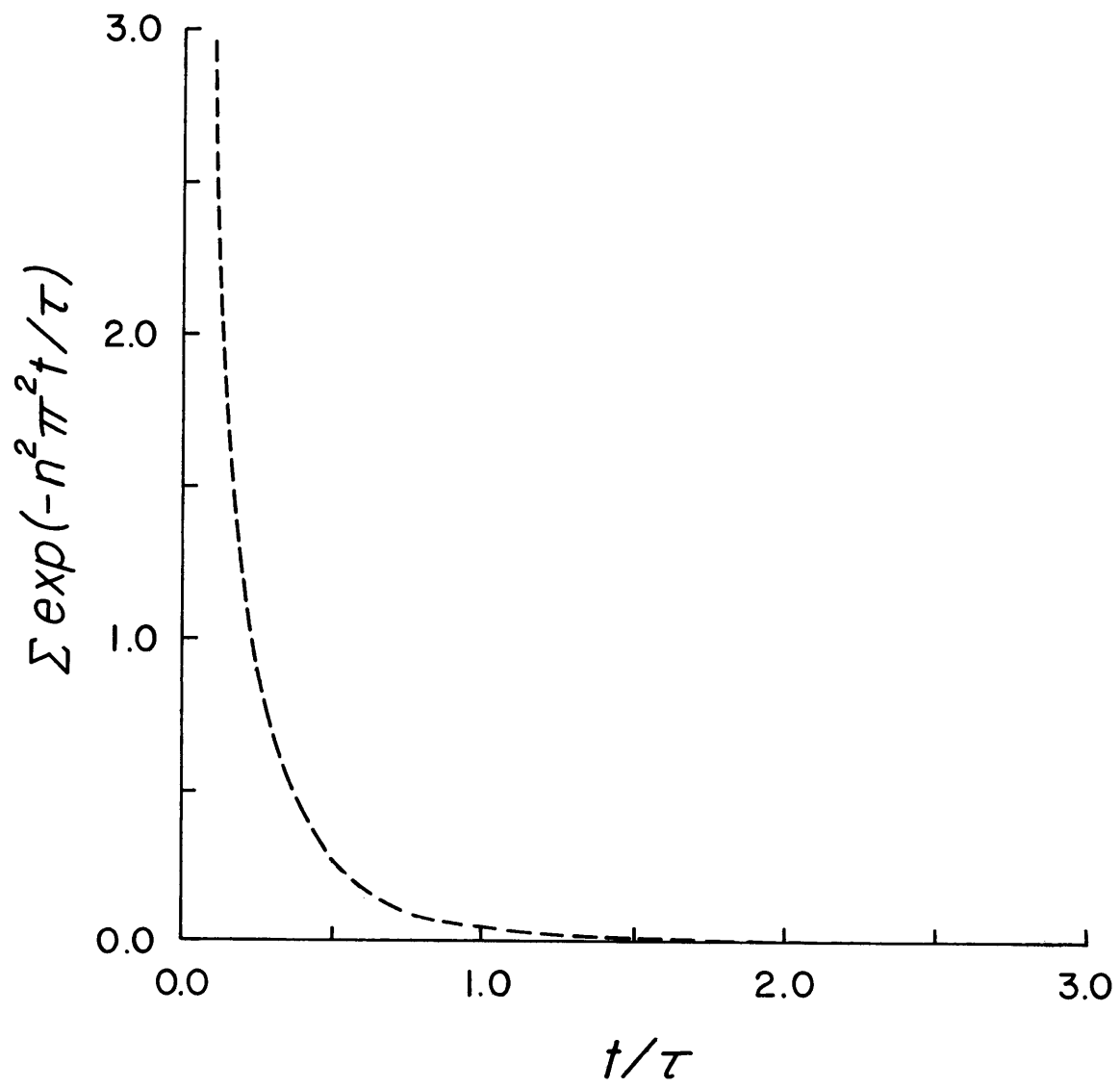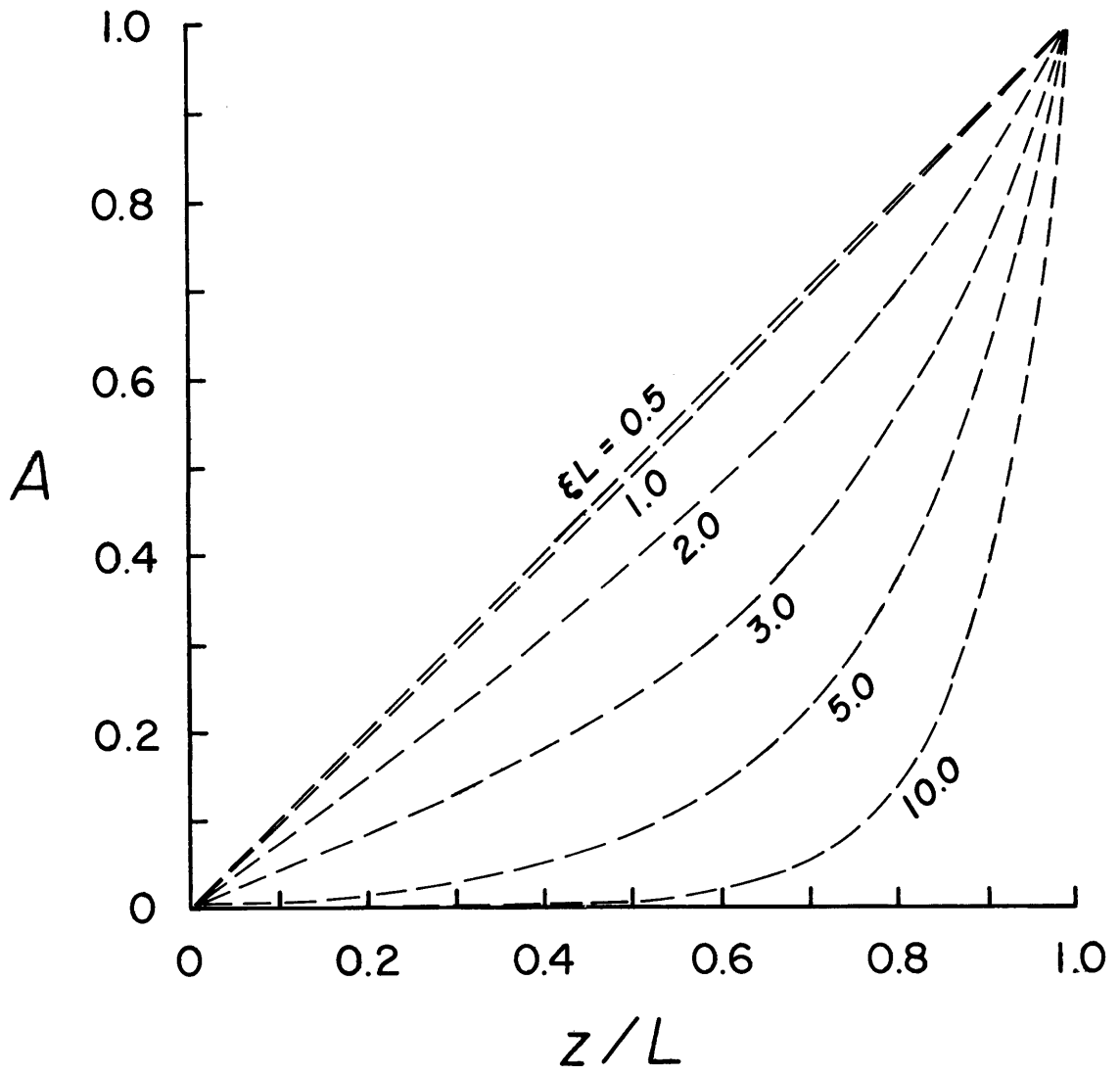
Figure 5. Variation of A, defined in equation 7, across the cross-section of a slab, for a range of values for ξL.

al., in preparation) roughly corresponds to the parameters, Q = 0.5 HFU, W = 10^{-7} cm/sec, and at a depth of 5 meters (the average depth of our data) is of order of magnitude 10^{-8} ^{o}C/cm^{2}. For a sediment thickness of over a hundred meters, at a depth of 5 meters equation 9 is of order of magnitude T_{o} 10^{-11} ^{o}C/cm^{2}.

A second possible model is the thermal effect of the venting of hydro-tnermal fluids through outcropping porous basement. Sleep and Wolery (1978) considered two variations of this model, a crack or fault model and a cylindrical outcrop model. In both models a horizontal isotherm, T_{L}, is imposed at depth L, which for our models will be considered the lower boundary of the sediment layer. At the vertical contact between the outcrop and the sediment, arbitrary temperature distribution can be imposed. This temperature distribution is related to the rate at which fluid exits the outcrop and introduces non-linearities in the steady state temperature field which decay with distance from the contact. Of interest is the rate at which this anomalous temperature field dissipates.

In the crack or fault model, tne temperature distribution is governed by Laplaces's equation

$$\nabla^{2}T = 0 \qquad (8)$$

For tne boundary conditions T = 0 at z = 0 and T = T_{L} at z = L, equation 8 is satisfied by a solution of the form

$$T = \frac{T_{L}z}{L} + \sum_{n=1}^{\infty} B_{n} \sin(\frac{n\pi z}{L}) \exp(-\frac{n\pi x}{L}) \qquad (9)$$

Imposing a general boundary condition at x = 0 equal to F(z) we have

$$B_n = \frac{2}{L} \int_0^L F(z) \sin(\frac{n\pi z}{L}) \, dz \tag{10}$$

The second term in equation 9 is the effect of the anomalous temperature field on the otherwise linear temperature versus depth relationship. The decay of this term with distance from the fault is shown in Figure 6 which is a non-dimensional plot of $\sum_{n=1}^{\infty} \exp(-n\pi x/L)$. This figure demonstrates the limited range of effect of this model.

For the cylindrical outcrop model, Laplace's equation in cylindrical coordinates is

$$\frac{d^2 T}{dz^2} + \frac{1}{r} \frac{dT}{dr} + \frac{d^2 T}{dr^2} = 0 \tag{11}$$

The solution to this problem for a seamount of radius R is

$$T(z,r) = \frac{T_L z}{L} + \sum_{n=1}^{\infty} B_n \sin(\frac{n\pi z}{L}) \frac{K_0(n\pi(\frac{R+r}{L}))}{K_0(\frac{n\pi R}{L})} \tag{12}$$

where K_0 is a modified Bessel function (Abromowitz and Stegun, 1964), r is radial distance from the seamount/sediment layer contact and B_n is determined in the same manner as previously discussed for the crack model. The distribution of the temperature field with increasing r decreases as the ratio of two Bessel functions. Figure 7 shows the relationship of the sum of this ratio as a function of r/L for several values of R/L. It is clear that the anomalous temperature field in the cylindrical model falls off quickly as r increases.

Figure 6. Non-dimensionalized plot of $\sum\limits_{n=1}^{\infty} \exp(-n\pi x/L)$ versus distance x (from equation 9).
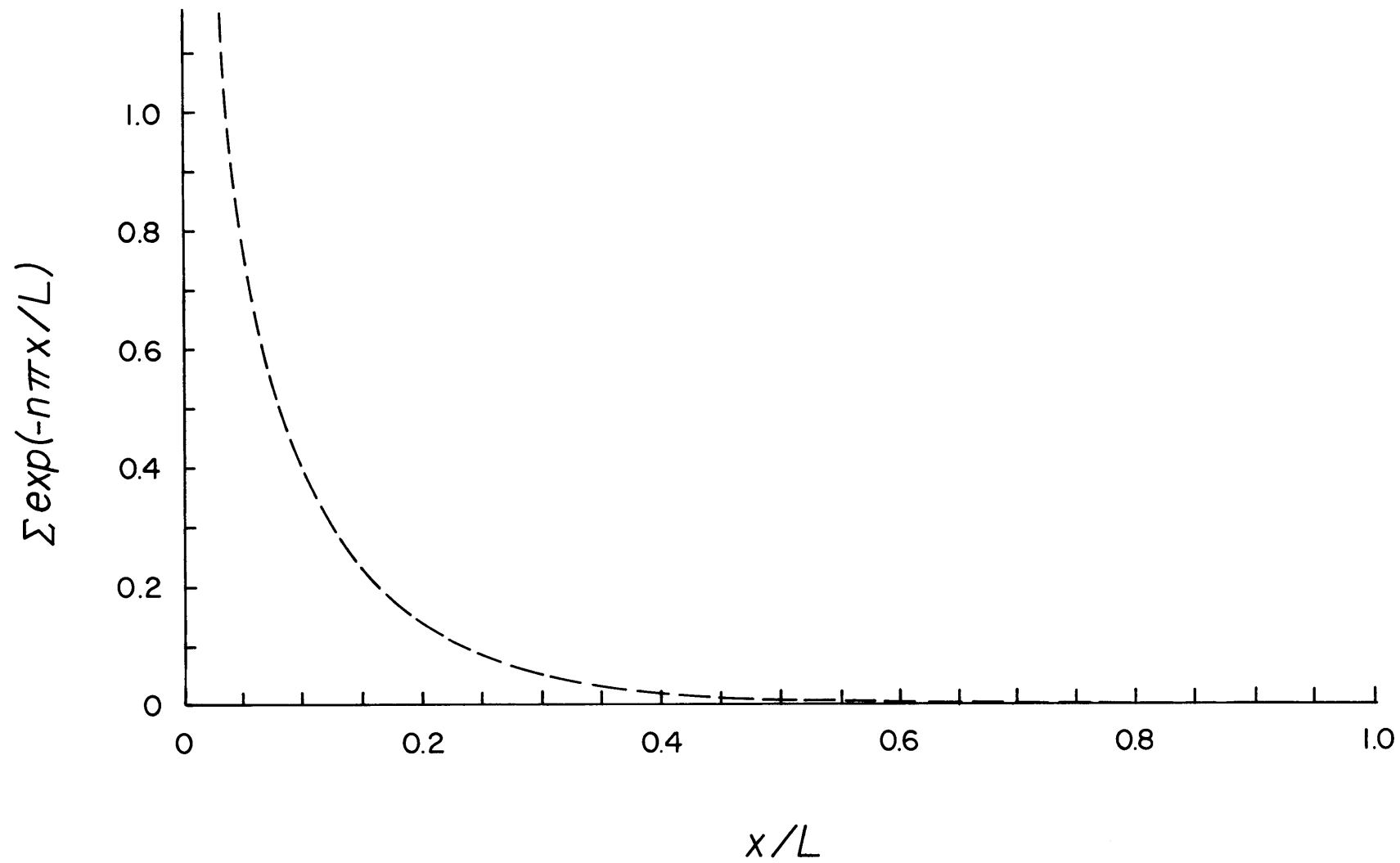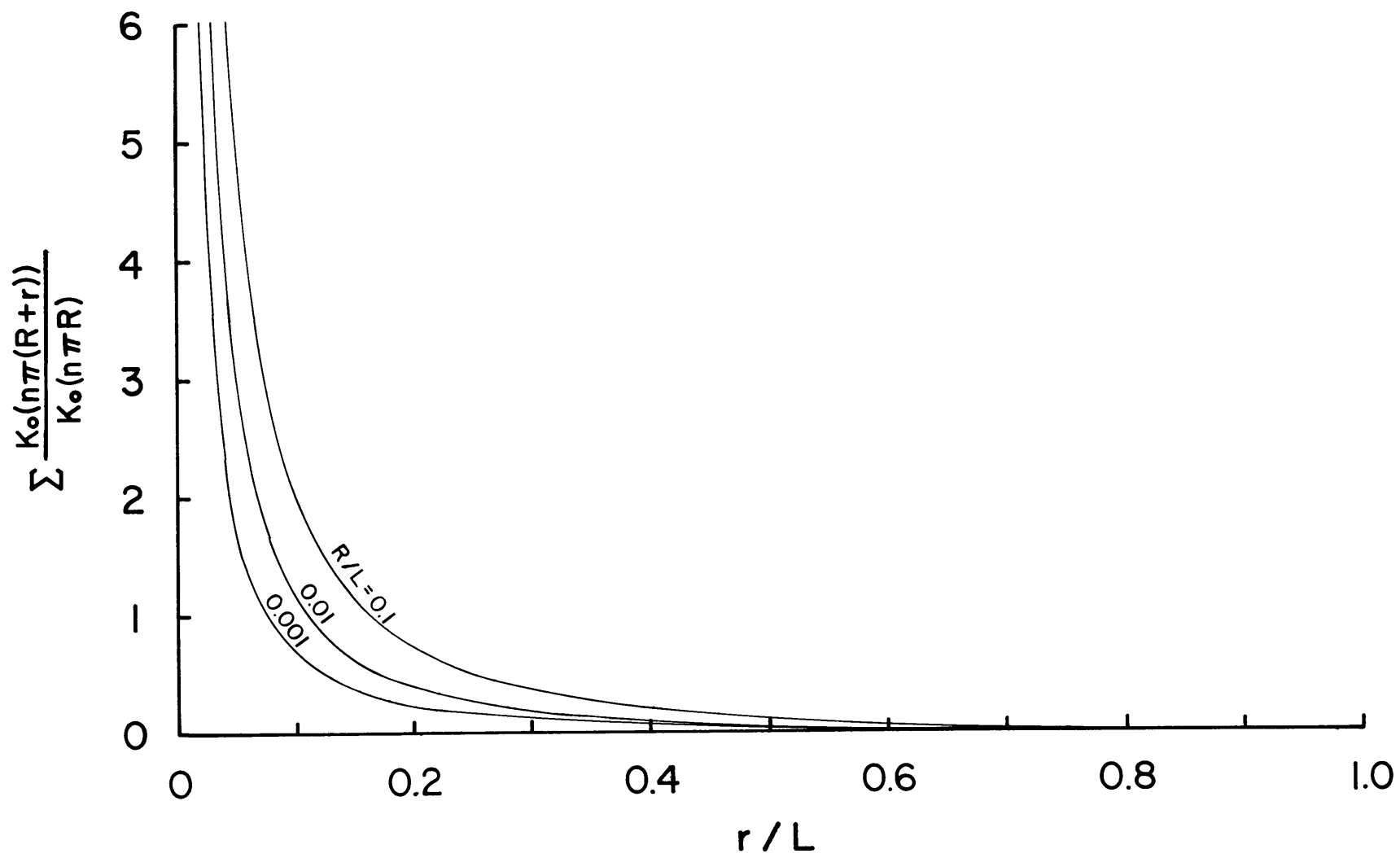
Figure 7. Plot of

$$\sum_{n=1}^{\infty} K_0 \left(n\pi \left(\frac{R + r}{L} \right) \right) \, / \, K_0 \left(\frac{n\pi R}{L} \right)$$

versus r/L for several values of R/L.

Non-steady state solutions to equations 2 and 4 are not able to resolve the problem. If the onset of advection is recent, the approach to steady-state would be dominated by the advection component of the response. Both the thermal and chemical characteristics would show similar behavior. If advection had recently ceased, the approach to steady-state would be dominated by the diffusive component of the response. Since the thermal diffusivity is greater, the temperature profile would not show advective behavior while the chemical profile would.

CONCLUSIONS:

A three order of magnitude discrepancy in the estimated rate of fluid flux resulted from the application of a convective/conductive transport model to geothermal and geochemical profiles observed at three sites in the equatorial Pacific Ocean. Rates predicted by geochemical profiles, order of magnitude 10^{-9} cm/sec, are not compatible with those predicted by the thermal profiles, order of magnitude 10^{-6} cm/sec. Analysis of the effects of simple conductive thermal models show that temperature distributions similar to those observed dissipate over short distances from the source of the temperature perturbation. Non-steady state solution of the convection/conduction governing equations were also not able to resolve this incompatibility. At present we cannot resolve the difference in these data sets.

ACKNOWLEDGEMENTS:

BIBLIOGRAPHY:

Abromowitz, M. and I. A. Stegun, Handbook of mathematical functions, National Bureau of Standards, U.S. Government Printing Office, Washington, D.C. (1964) 1046p.

Anderson, R. N., M. G. Langseth and J. G. Sclater, The mechanisms of heat transfer through the floor of the Indian Ocean, J. Geophys. Res., 82 (1977) 3391-3409.

Anderson, R. N., M. A. Hobart and M. G. Langseth, Geothermal convection through oceanic crust and sediments in the Indian Ocean, Science, 204 (1979) 828-832.

Arrhenius, G., Sediment cores from the East Pacific. Properties of the sediment. Rep. Swed. Deep-Sea Exped. 1947-1948, 1 (1952) 1-228.

Berner, R. A., Sulfate reduction and the rate of deposition of marine sediments, Earth Planet. Sci. Lett., 37 (1978) 492-498.

Carslaw, H.S. and J.C. Jaeger, Conduction of heat in solids, 2nd ed. (1959) Clarendon Press, Oxford, England.

Corliss, J. B., J. R. Dymond, L. I. Gordon, J. M. Edmond, R. P. Von Herzen, R. D. Ballard, K. Green, D. L. Williams, A. Bainbridge, K. Crane, and Tj. H. van Andel, Submarine thermal springs on the Galapagos Rift, Science, 203 (1979) 1073-1083.

Crowe, J. and A. J. Silva, Permeability measurements of Equatorial Pacific carbonate oozes using a direct measurement back-pressured technique, to be submitted to J. Geophys. Res.

Crowe, J., R. P. Von Herzen and K. E. Green, The eastern equatorial Pacific Ocean heat flow low: evidence of hydrothermal circulation within 15-40 Ma crust, to be submitted to J. Geophys. Res.

Ewing, J., M. Ewing, T. Aitken and W. J. Ludwig, North Pacific sediment layers measured by seismic profiling, American Geophysical Union, Geophysical Monograph 12 (1968) 147-173.

Gieskes, J. M., Interstitial water studies, Leg 25, In: Simpson, E. S. W., R. Schlich., et al., Initial Reports of the Deep Sea Drilling Project, 25 (1974) 361-394.

Green, K. E., Ph.D. thesis, Massachusetts Institute of Technology/Woods Hole Oceanographic Institution (1980) 232 p.

Langseth, M. G. and B. M. Herman, Heat transfer in the oceanic crust of the Brazil Basin, submitted to J. Geophys. Res.

Lister, C. R. B., Heat flow west of the Juan de Fuca Ridge, J. Geophys. Res., 75 (1970) 2648.

Lister, C. R. B., On the thermal balance of a mid-ocean ridge, Geophys. J. R. astr. Soc., 26 (1972) 515-535.

Luther, G. W. and A. L. Meyerson, Polarographic analysis of sulfate ion in seawater, Anal. Chem., 47 (1975) 2058-2059.

McDuff, R. E. and J. M. Gieskes, Calcium and magnesium profiles in DSDP interstitial waters: diffusion or reaction?, Earth Plant. Sci. Lett., 33 (1976) 1-10.

McDuff, R. E., Conservative behavior of calcium and magnesium in the interstitial waters of marine sediments: identification and interpretation, Ph.D. thesis, Univer. California, San Diego (1978) 182p.

McDuff, R. E. and R. A. Ellis, Determining diffusion coefficients in marine sediments: a laboratory study of the validity of resistivity techniques, Am. Jour. Sci., 279 (1979) 666-675.

Ribando, R. J., K. E. Torrence and D. L. Turcotte, Numerical models for hydrothermal circulation in the ocean crust, J. Geophys. Res., 81 (1976) 3007-3012.

Sayles, F. L. and F. T. Manheim, Interstitial solutions and diagenesis in deeply buried marine sediments: results from the Deep Sea Drilling Project, Geochim. Cosmochim. Acta., 39 (1975) 103-127.

Sayles, F. L., The composition and diagenesis of interstitial solutions - I. Fluxes across the seawater-sediment interface in the Atlantic Ocean, Geochim. Cosmochim. Acta., 43 (1979) 527-546.

Sclater, J. G., R. P. Von Herzen, D. L. Williams, R. N. Anderson and K. Klitgord, The Galapagos Spreading Centre: heat flow low on the north flank, Geophys. J. Roy. Astr. Soc., 38 (1974) 609-626.

Sclater, J. G., J. Crowe and R. N. Anderson, On the reliability of oceanic heat flow averages, J. Geophys. Res., 81 (1976) 2997-3006.

Sclater, J. G., C. Jaupart and D. A. Galson, The heat flow through oceanic and continental crust and the heat loss of the Earth, Rev. Geophys. and Space Phys., 18 (1980) 269-311 .

Sleep, N. H. and T. J. Wolery, Egress of hot water from midocean ridge hydrothermal systems: some thermal constraints, J. Geophys. Res., 83 (1978) 5913-5922.

Spiess, F. N., K. C. Macdonald, T. Atwater, R. Ballard, A. Carranza, D. Cordoba, C. Cox, V. M. Diaz Garcia, J. Francheteau, J. Guerrero, J. Hawkins, R. Haymon, R. Hessler, T. Juteau, M. Kastner, R. Lawson, B. Luyendyk, J. D. Macdougall, S. Miller, W. Normark, J. Orcutt and C. Ranjin, East Pacific Rise: hot springs and geophysical experiments, Science, 207 (1980) 1421.

Talwani, M., C. C. Windisch and M. G. Langseth, Reykjanes Ridge Crest: a detailed geophysical study, J. Geophys. Res., 76 (1971) 473-517.

Von Herzen, R. P. and R. N. Anderson, Implications of heat flow and bottom water temperature in the eastern equatorial Pacific, Geophys. J. R. Astr. Soc., 26 (1972) 427-458.

Von Herzen, R. P. and A. E. Maxwell, The measurement of thermal conductivity of deep-sea sediments by a needle-probe method, J. Geophys. Res., 64 (1959) 1557-1563.

Williams, D. L., K. E. Green, Tj. H. van Andel, R. P. Von Herzen, J. R. Dymond and K. Crane, The hydrothermal mounds of the Galapagos Rift: observations with DSRV Alvin and detailed heat flow studies, J. Geophys. Res., 84 (1979) 7467-7484.